FACULTY OF ENGINEERING AND ARCHITECTURE

Non-Contact Photoacoustic Imaging Using Silicon Photonics-Based Laser Doppler Vibrometry

Emiel Dieussaert

Doctoral dissertation submitted to obtain the academic degree of
Doctor of Photonics Engineering

Supervisors
Prof. Yanlu Li, PhD - Prof. Em. Roel Baets, PhD
Department of Information Technology
Faculty of Engineering and Architecture, Ghent University

December 2024

GHENT UNIVERSITY

ISBN 978-94-6355-932-4
NUR 954
Wettelijk depot: D/2024/10.500/137

Members of the Examination Board

Chair

Prof. Em. Daniël De Zutter, PhD, Ghent University

Other members entitled to vote

Prof. Mathias Kersemans, PhD, Ghent University
Prof. Christian Rembe, PhD, Technische Universität Clausthal, Germany
Prof. Günther Roelkens, PhD, Ghent University
Prof. Xavier Rottenberg, PhD, imec & KU Leuven
Prof. Patrick Segers, PhD, Ghent University

Supervisors

Prof. Yanlu Li, PhD, Ghent University
Prof. Em. Roel Baets, PhD, Ghent University

Dankwoord

Lang, lang geleden, in het jaar 2015, startten 3 Truiense knaapjes (Maxim, Alexander en ik) aan de opleiding burgerlijk ingenieur in Gent. Dit was het begin van mijn academisch avontuur, dat nu toch al meer dan 10 jaar geleden is gestart. De opleiding Engineering Physics bleek niet alleen het beste bij mij te passen op het vlak van interesse, ik kreeg er ook veel toffe klasgenoten bij, met wie ik nog steeds maar al te graag ga kamperen of volleyballen. Voor mijn masterthesis zocht ik naar een multidisciplinair, toepassingsgericht onderwerp en zo kwam ik terecht bij professor Roel Baets en zijn team. Zij ontwikkelden toen fotonische chips om antibioticawaarden te meten in het bloed. Tijdens deze masterthesis kreeg ik fantastische begeleiding door Ali Raza en volgde ik het vak microfotonica, gegeven door Dries en Roel. Dit wakkerde mijn interesse voor dit vakgebied helemaal aan en hierdoor besliste ik om een PhD aan te vatten in de Photonics Research Group. Opnieuw koos ik voor een toepassingsgericht onderwerp, ditmaal begeleid door Yanlu Li en Roel Baets. Voor deze kans en hun begeleiding ben ik hen beiden zeer dankbaar. Roel wil ik bedanken voor de mogelijkheden die hij mij doorheen de jaren heeft gegeven en de gerichte feedback op de gepaste momenten. Ik kijk op naar zijn passie voor het vak en de menselijke en respectvolle manier waarop hij onze vakgroep leidde.

I am deeply grateful to Yanlu for being such a friendly, patient and approachable advisor. I truly enjoyed our long technical discussions and I have learned so much from his expertise. At Imec, I would also like to thank Hilde Jans and Xavier Rottenberg for supporting this research and our interesting meetings and visits to Leuven. I would also like to thank all of my jury members, for taking the time to review my manuscript and providing me with feedback to improve the quality of this book.

Throughout this PhD journey, I have had the privilege of meeting and getting to know so many wonderful and friendly people, whom I would like to thank. First and foremost, my colleagues at the Photonics Research Group (PRG)—the people who surrounded me most of the time and with whom I shared many conversations by the coffee machine, during lunch or at the ‘Friday drinks’. I would like to express my gratitude to all professors, post-docs, PhDs and our support staff for making the

PRG a fun workplace and a successful research group.

More specifically, I would like to thank my office mates that made my time in the office so much more enjoyable; Ewoud and Tom S., for bringing us Dutch culture; Emmanuel for his role as great office leader; Robbe, for being a great neighbour; Ruben, for his sarcastic humour; Tom V., for his quirkiness, Valeria, for bringing some Italian energy and a new espresso machine and Dennis and Abdul, for their wise opinions on a broad range of topics.

Another important group of people from the PRG are those who directly contributed to this work. I want to acknowledge them all because, without their help, this work would not have been possible: Clemens, for getting this rookie started in the lab; Steven, for wirebonding many samples; Liesbet and Sheila, for their assistance with the PDMS samples; Amin, Raphael, Hendrik, Jasper, and Hasan, for their support throughout the years in developing electronics; Zhang and Yichen, for their help with glueing of fibers. Also, all thesis students I had the opportunity to work with and who each left their imprint to this work: Julia, Maxim, Selènè, Guo, Ruifeng, Milan: thank you! En natuurlijk Kristien, Ilse (x2) en Bert, merci voor jullie hulpvaardigheid bij allerlei IT- en HR-zaken.

I truly enjoyed organizing events together with a great group of people for the Photonics Society Ghent. Thank you Max, Korneel, Jorik, Stijn, Viktor, Sarah, Rohan, Frederico and Thanos!

Na een dag werken was er voor mij geen betere uitlaatklep dan atletiek. Bedankt aan de hele atletiekgroep, met wie ik de afgelopen jaren met veel plezier fysiek heb afgezien.

Tot slot wil ik natuurlijk de belangrijkste mensen in mijn leven bedanken: Mama, papa, bedankt voor jullie onvoorwaardelijke steun en heldere blik op het leven die jullie hebben doorgegeven. Tibo, voor al die jaren met plezier mijn liefdevol geplaag te ondergaan. Laura, omdat je de perfecte tegenpool bent waar het nodig is, en we op andere vlakken zo goed op elkaar aansluiten.

Gent, November 2024
Emiel Dieussaert

Contents

List of Acronyms

ADC	Analog-to-Digital Converter
AOM	Acousto-Optic Modulator
AR-PAM	Acoustic-Resolution Photoacoustic Microscopy
CMOS	Complementary Metal-Oxide-Semiconductor
EDFA	Erbium-Doped Fiber Amplifier
FFT	Fast Fourier Transform
FOV	Field of View
FPR	Free Propagation Region
I	In-phase
LDV	Laser Doppler Vibrometry
LiDAR	Light Detection and Ranging
MEMS	Micro-Electro-Mechanical Systems
MMI	Multimode Interferometer
MRI	Magnetic Resonance Imaging
MZI	Mach-Zehnder Interferometer
NA	Numerical Aperture
NED	Noise Equivalent Displacement

NEP	Noise Equivalent Pressure
NIR	Near Infrared
OCT	Optical Coherence Tomography
OM	Optical Microscopy
OMUS	Optomechanical Ultrasound Sensor
OR-PAM	Optical-Resolution Photoacoustic Microscopy
PAI	Photoacoustic Imaging
PAT	Photoacoustic Tomography
PC	Personal Computer
PCB	Printed Circuit Board
PD	Photodetector
PDK	Process Design Kit
PDMS	Polydimethylsiloxane
PIC	Photonic Integrated Circuit
Q	Quadrature
RF	Radio Frequency
RMSE	Root Mean Square Error
RX	Receiver
SOA	Semiconductor Optical Amplifier
SOI	Silicon-On-Insulator
SNR	Signal-to-Noise Ratio
TX	Transmitter
US	Ultrasound Imaging

Samenvatting

Inleiding

Foto-akoestische beeldvorming is een relatief nieuwe biomedische beeldvormingstechniek die toelaat om biomedische structuren in kaart te brengen die diep wonder de huid liggen [1, 2]. Dit maakt het bijzonder interessant voor medische toepassingen zoals het monitoren van het zuurstofgehalte in een weefsel [3] en het in kaart brengen van bloedvaten [4]. In tegenstelling tot traditionele beeldvormingsmethoden, zoals optische microscopie of MRI, combineert deze techniek optische excitatie en ultrasone detectie. Fig. 1 toont een schematisch overzicht van het werkingsprincipe van deze techniek. Een gepulseerde lichtbron wordt gericht op een weefsel. Daar veroorzaakt de plotselinge, lokale absorptie van het gepulseerde licht een lokale verhitting. Deze lokale verhitting leidt tot een snelle thermische expansie, die drukgolven, of ultrasone golven, genereert binnen het weefsel. Deze ultrasone golven verplaatsen zich vervolgens door het weefsel en worden gedetecteerd door ultrasone transducers die zich bevinden aan de rand van het sample. De gedetecteerde signalen worden verwerkt om een beeld te reconstrueren dat de optische absorptie-eigenschappen van het weefsel in kaart brengt, waardoor informatie over de structuur en samenstelling van het sample of weefsel wordt verkregen.

Conventionele foto-akoestische beeldvormingssystemen gebruiken krachtige gepulseerde lasers voor de optische excitatie en ultrasone sondes voor de akoestische detectie [1, 5]. Deze sondes vereisen contact met het sample en gebruiken vaak een soort koppelingsgel. Deze contact-technieken brengen aanzienlijke nadelen

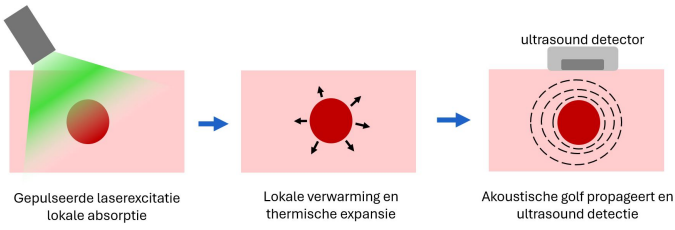

Figuur 1: Schematisch overzicht van de werking van foto-akoestische beeldvorming.

met zich mee, zoals het risico op infectie of monstercontaminatie [6].Contactloze alternatieven zouden deze risicos kunnen elimineren. In de afgelopen decennia zijn optische technieken gebruikt om ultrasone trillingen op afstand te detecteren [7–12]. Laser Doppler Vibrometry (LDV) is een optische techniek waarmee bewegingen van een target gemonitord kunnen worden door met een laserstraal. Ultrasone golven in een sample veroorzaken miniscule bewegingen op het oppervlak. Deze trillingen kunnen deze dus ook gedetecteerd worden met LDV. Hoewel LDV's gebruikt zijn in laboratoriumdemonstraties [8, 11–13], zijn er praktische beperkingen. Foto-akoestische beeldvorming vereist namelijk de detectie van de ultrasone trillingen op meerdere punten op het oppervlak van het sample. De huidige LDV systemen scannen de straal over het oppervlak van het sample, wat leidt tot een complex en duur systeem dat de beeldvormingssnelheid compromitteert. Een oplossing hiervoor is het ontwikkelen van LDV's met meerdere detectie stralen, die gelijktijdige ultrasone golven detecteert op verschillende locaties. Conventionele LDV's hebben gewoonlijk maar een paar detectiestralen omdat ze afhankelijk zijn van discrete optische componenten. Opschaling naar meer detectiestralen is moelijk omdat de complexiteit en kost schaalt met het aantal detectiestralen.

Recente demonstraties hebben aangetoond dat op silicon photonics gebaseerde LDV's veelbelovend zijn om deze beperkingen van conventionele systemen te overwinnen [14, 15]. Silicon photonics of Silicium-fotonica is een technologie die gebruikt maakt van technieken die oorspronkelijk ontwikkeld zijn voor de fabricatie van elektronische chips, om micro- en nanoschaal structuren in silicium te creëren die licht manipuleren [16, 17]. Door meerdere optische componenten te integreren op een enkele siliciumchip, kunnen silicon photonics LDV's de grootte, complexiteit en kosten van multi-beam detectiesystemen aanzienlijk verminderen. Fig. 2 toont een op silicon photonics implementatie van een homodyne LDV. Een coherente laserbron wordt gekoppeld in het fotonische geïntegreerde circuit (Photonic Integrated Circuit, PIC), waar het laserlicht wordt gesplitst in een referentiepad en een meetpad. Het meetlicht wordt uit het PIC geleid naar een target via een ontvangst- en transmissiegrating (RX/TX grating). Na reflectie van het meetlicht door het target wordt het licht teruggekoppeld in het PIC en gecombineerd met het referentielicht in de 90°-optische hybride, waarbij vier combinaties worden geproduceerd, elk met een verschillende relatieve faseshift. Deze combinaties worden vervolgens omgezet in elektrische signalen door on-chip fotodetectoren. Terwijl het target beweegt, verandert de padlengte van het meetlicht. Deze verandering in padlengte moduleert de elektrische signalen van de fotodetectoren door de interferentie van het meetlicht met het referentielicht. Deze elektrische signalen kunnen worden uitgelezen via de elektrische contactpads op het PIC en kunnen dus gebruikt worden om bewegingen te detecteren.

Eerder werk toonde aan dat on-chip LDV's goed grote trillingen kunnen meten bij relatief lage frequenties [14, 15]. Detectie van ultrasone golven vereist echter het meten van trillingen bij hogere frequenties (in het ultrasone gebied) wat typisch gepaard gaat met kleinere trillingen. In dit werk passen we daarom de technologie

aan om ultrasone detectie mogelijk te maken om het potentieel ervan voor foto-akoestische beeldvorming te demonstreren.

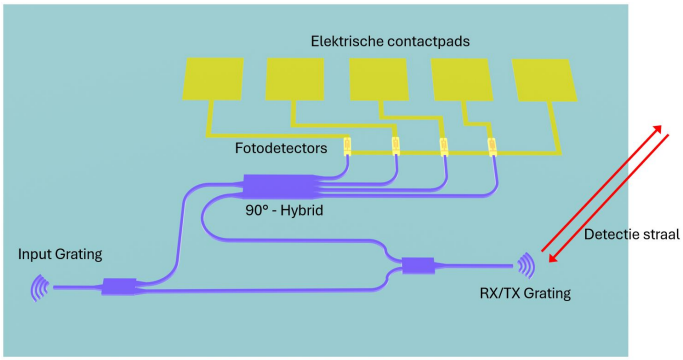

Figuur 2: Weergave van een silicon photonics implementatie van een homodyne LDV. Licht wordt in de chip gekoppeld via de ingangsgrating, vervolgens wordt het gesplitst in een meet- en referentiearm. Het meetlicht wordt in en uit de chip gekoppeld via de TX/RX-antenna. De hybride component combineert het licht op vier verschillende manieren. Fotodetectoren zetten deze optische combinaties om in elektrische signalen, waaruit de verplaatsing kan worden gedemoduleerd.

Resultaten

Siliciumfotonica-gebaseerde LDV voor ultrasone detectie

Om ultrasone detectie voor foto-akoestische beeldvorming mogelijk te maken met een op silicon photonics gebaseerde LDV, werd een systeem ontwikkeld met een detectie-bandbreedte tot in het ultrasoon frequentie-gebied. Een grote detectie-bandbreedte is cruciaal voor het bereiken van foto-akoestische beeldvorming met een hoge resolutie. Doordat hogere frequenties gepaard gaan met lagere verplaatsingsamplitudes, is de bandbreedte een belangrijke afweging. Hierdoor werd het systeem geoptimaliseerd om zich te richten op het lagere ultrasone frequentiegebied met een bruikbare bandbreedte tot ongeveer 3,5 MHz.

Het silicon photonics LDV-systeem toonde een ruis-limiet die vergelijkbaar is met die van commerciële LDV-systemen, waarbij schattingen aangeven dat de ruisniveaus dicht bij de fundamentele shot-noise limiet liggen. In een poging om de detectielimiet verder te verlagen, onderzochten we theoretisch of optische versterkers het systeem kan verbeteren. Deze theoretische berekeningen toonden echter aan dat, in de meeste praktische situaties, deze versterkers de detectielimiet niet significant verbeteren, voornamelijk vanwege de extra faseruis die wordt geïntroduceerd.

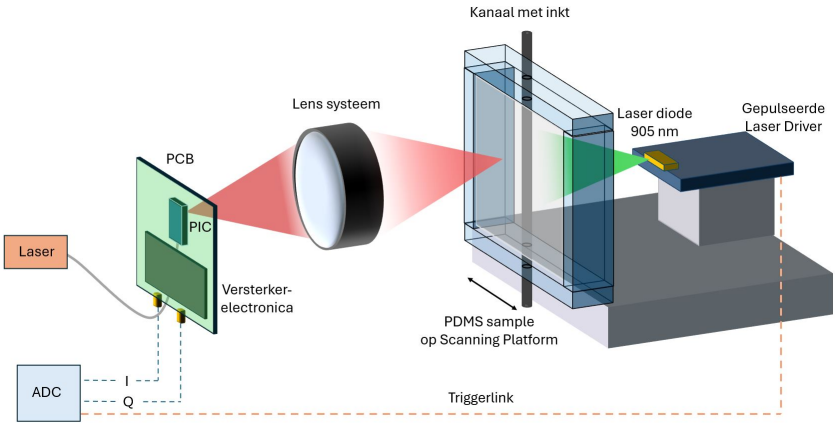

Figuur 3: Schematisch overzicht van de lab-demonstratie van foto-akoestische beeldvorming

Foto-akoestische beeldvorming met op siliciumfotonica gebaseerde LDV

Om contactloze foto-akoestische beeldvorming aan te tonen, werd een lab demonstratie ontwikkeld, zoals weergegeven in Fig. 3. Deze demonstratie werkt met een op silicon photonics LDV en een miniatuur-excitatiebron. Het LDV-fotonisch geïntegreerd circuit is geconnecteerd met een printplaat (PCB) waarop de benodigde versterkerelektronica is aangebracht. Nadat de fotodetectorsignalen differentieel zijn versterkt, resulterend in een In-Fase (I) en Quadratuur (Q) signaal die de relatieve beweging van het target beschrijven, worden deze signalen gedigitaliseerd met behulp van een Analoog-naar-Digitaal Converter (ADC). Een lenssysteem focust het LDV-meetlicht op een zelfgemaakt sample. Dit sample is een plat, polydimethylsiloxaan (PDMS)-sample met een ingebed kanaal, dat ruwweg een bloedvat kan voorstellen.

Het ingebedde kanaal, gevuld met een inkt-wateroplossing, fungeert als de absorber, die foto-akoestische signalen genereert bij gepulseerde belichting. Een miniatuur-excitatiebron werd ontwikkeld met behulp van een 905 nm laserdiode of laserbar die is aangesloten op een gepulseerde laserdriver. Wanneer de gepulseerde laserbron het sample verlicht, genereert de plotselinge, gelokaliseerde absorptie foto-akoestische golven die zich naar het oppervlak van het PDMS-sample voortplanten. Deze golven veroorzaken kleine bewegingen op het oppervlak, die vervolgens worden gedetecteerd door het on-chip LDV-systeem. Een triggerlink tussen de excitatiebron en het detectiesysteem zorgt voor een nauwkeurige timing van de foto-akoestische signalen. Om scannen te mogelijk te maken, werd het sample en de excitatiebron gemonteerd op een scanning platform, waardoor de LDV foto-akoestische signalen kon detecteren op verschillende locaties langs een lijn over het oppervlak van het sample.

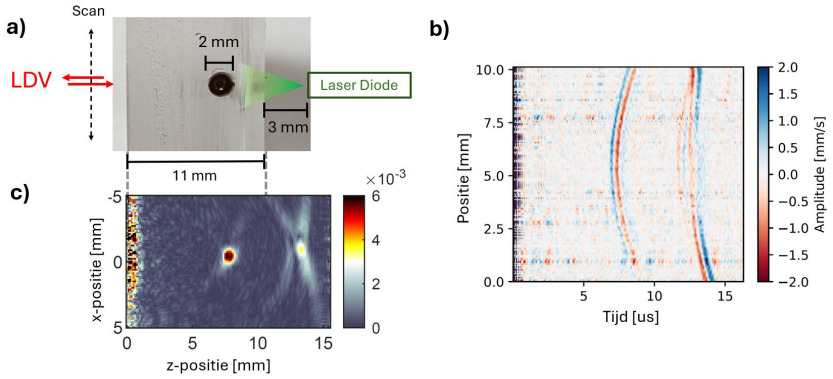

Figuur 4: a) Dwarsdoorsnede van het PDMS sample met een ingebed inkt kanaal, met indicatie van de LDV-zijde, de scan-as en de laserdiode-excitatiezijde. b) Oppervlakte-snelheid gemeten door de LDV op verschillende locaties langs de scan-as gedurende 16 μs na het afvuren van een excitatiepuls. De aankomsttijden van de foto-akoestische signalen variëren voor de verschillende posities. c) Een foto-akoestisch reconstructiebeeld gemaakt met behulp van de gegevens van b) met een reconstructie-algoritme (time reversal reconstruction).

Fig.4a toont een dwarsdoorsnede van een sample met een ingebed inkt-kanaal en toont de as waarover de LDV over het oppervlak scande. Met een stapgrootte van 125 μm werd de LDV-straal over het oppervlak van het sample gescand. Op elke scanlocatie registreerde de LDV het tijdsverloop van de oppervlakte-snelheid, zoals weergegeven in Fig.4b. Deze figuur laat zien dat een primair foto-akoestische signaal wordt gedetecteerd tussen 6 en 10 μs na het afvuren van de puls. Een secundair signaal is zichtbaar na 12 μs door reflectie van de akoestische golf. Met behulp van deze gegevens werd een reconstructie-algoritme (time reversal reconstruction) toegepast om het 2D foto-akoestische reconstructiebeeld te creëren. De reconstructie, weergeven in Fig. 4c, toont de oorsprong van het primaire foto-akoestische signaal van het inkt kanaal, maar ook een schaduw-afbeelding door de reflectie.

Vergelijkbare reconstructies werden gemaakt met samples met kanalen op verschillende diepten en met verschillende inktconcentraties, evenals met twee kanalen. Bovendien werd aangetoond dat het gebruik van een laserbar effectiever kan zijn dan een laserdiode, vanwege het specifieke verlichtingspatroon.

Schaalbare architectuur voor multibeam LDVs

Hoewel on-chip LDV's de opschaling naar enkele tientallen stralen mogelijk maken, vereist de opschaling naar honderden stralen geavanceerde verpakkingsmethoden of architecturale innovaties van de chip om het aantal elektrische verbindingen

met het fotonische geïntegreerde circuit te beperken. In deze thesis stellen we een alternatieve architectuur voor met een nieuwe component, de multi-beam frequentieverschuiver. Deze component verschuift verschillende detectiestralen naar verschillende optische draaggolffrequenties, waardoor de fotodetectorsignalen—die een lokale referentie combineren met de meetsignalen—kunnen worden gemultiplexed over een elektrische verbinding. Dit zou het aantal vereiste elektrische verbindingen drastisch kunnen verminderen.

De multi-beam frequentieverschuiver neemt een optisch monofrequent signaal en genereert meerdere signalen in verschillende optiische golfgeleiders (waveguides), elk met een andere frequentie-verschuiving. Dit wordt gerealiseerd door het monofrequente licht over een array van modulatoren te verdelen. Door akoestisch-optische modulatie na te bootsen met de array van on-chip modulatoren, kunnen verschillende harmonieken van de modulatie worden gesplitst worden naar verschillende uitgangen van een star coupler. Het werkingsprincipe van deze component is zowel theoretisch als door simulaties onderzocht.

Hoewel simulaties aangeven dat deze architectuur en bijbehorende component veelbelovend zijn in het verminderen van het aantal elektrische verbindingen, zou de implementatie hiervan een aanzienlijke wijziging betekenen ten opzichte van het huidige detectiesysteem. Enerzijds is de impact van deze verandering op de detectielimiet onzeker, en anderzijds vergt deze ingrijpende aanpassing aanzienlijke engineering-resources. Om deze redenen is een systeem gebaseerd op deze nieuwe architectuur niet binnen de scope van deze thesis geïmplementeerd.

Conclusie

Dit werk heeft met behulp van een labdemonstratie aangetoond dat on-chip LDV's gebruikt kunnen worden voor contactloze foto-akoestische beeldvorming. De thesis legt uit hoe we met een on-chip LDV en compacte excitatiebron, contactloos, 2D fotoakoestische beelden hebben gemaakt van zelfgemaakte samples. De overgang naar beeldvorming van in-vivo samples brengt verschillende uitdagingen met zich mee. Een van die uitdagingen is de signaalkwaliteit van de LDV bewaren voor ruwe oppervlaktes met diffuse reflectie, zoals de huid.

Een potentiële oplossing is het gebruik van lenzen met een hoge numerieke apertuur (NA) en automatische focustechnieken om de verzamelingsefficiëntie voor diffuus reflecterende en bewegende oppervlakken te optimaliseren. Een andere belangrijke uitdaging is het opschalen van het systeem om honderden stralen te verwerken, wat de noodzaak voor scannen zou elimineren. Dit werk stelt een nieuwe architectuur voor die het aantal vereiste elektrische verbindingen vermindert, terwijl alternatieve benaderingen geavanceerde verpakkingsmethoden zouden kunnen omvatten om een groot aantal elektrische verbindingen te accommoderen.

Summary

Introduction

Photoacoustic imaging is a biomedical imaging technique that offers a unique combination of optical contrast and deep tissue penetration [1, 2]. This makes it particularly useful for medical applications like monitoring blood oxygenation [3] and mapping vasculature [4]. Unlike traditional imaging methods, such as optical microscopy or MRI, it combines optical excitation and ultrasound detection. Fig. 5 shows a schematic of the working principle of this technique. A pulsed light source is directed towards a sample. There, sudden, local absorption of the pulsed light source causes a local heating. This localized heating leads to a rapid thermal expansion, which generates pressure waves, or ultrasound waves, within the tissue. These ultrasound waves then propagate through the tissue and are detected by ultrasonic transducers positioned around the sample. The detected signals are processed to reconstruct an image that represents the optical absorption properties of the tissue, providing information about the structure and composition of the sample.

Conventional photoacoustic imaging systems use high-power pulsed lasers for optical excitation and contact-based ultrasound probes for acoustic detection [1, 5]. This requires contact with the sample, often facilitated by a coupling gel. The need for direct contact presents significant drawbacks, due to the risk of infection or sample contamination [6]. This has driven the development and search for

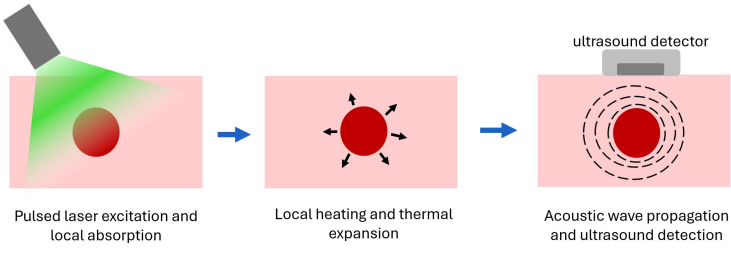

Figure 5: Schematic of the working principles of photoacoustic imaging

non-contact alternatives, which aim to eliminate these risks. Over the past decades, optical techniques have been used to detect ultrasound vibrations remotely [7–12]. One approach, called Laser Doppler Vibrometry (LDV), remotely probes the surface of the sample and, based on interferometric principles, can detect any movement of the surface of the sample including movement due to ultrasound waves. While they have been used in lab demonstrations [8, 11–13], practical limitations remain. Photoacoustic imaging requires the detection of ultrasound signals at multiple locations and therefore LDV-based systems scan the beam over the surface of the sample, which creates a complex and expensive system that compromises the imaging speed. One solution is developing multi-beam LDVs, that enable simultaneous ultrasound detection at different locations. However, conventional fiber- or free-space-based LDVs are limited to accommodate only a couple of detection beams, because they rely on discrete optical components which makes scaling the number of detection beams bulky and expensive.

Recently, the development of silicon photonics-based- LDVs have shown promise to overcome the limitations of conventional systems [14, 15]. Silicon photonics is a technology that leverages CMOS-like techniques, to create micro- and nanoscale structures in silicon to manipulate light [16, 17]. By integrating multiple optical components onto a single silicon chip, silicon photonics-based LDVs can significantly reduce the size, complexity, and cost of multi-beam detection systems. Fig. 6 shows a layout of a single-beam silicon photonics-based implementation of a homodyne LDV. A coherent laser source is coupled into the photonic integrated circuit (PIC), where the laser light is split into a reference path and measurement path. The measurement light is directed out of the PIC towards a target via a receive and transmission grating (RX/TX grating). After reflection off the target, the light is coupled back into the PIC and combined with the reference light in the 90°-optical hybrid, producing four combinations, each with a different relative phase shift. These combinations are then transferred into electrical signals by on-chip photodetectors. As the target moves, it changes the path length of the measurement light. This path length change can be demodulated from the electrical signals from the photodetectors due to the interference of the measurement light with the reference light. These electrical signals can be accessed through the electrical contact pads on the PIC.

While previous work has demonstrated silicon photonics-based LDVs for measuring relatively large vibrations at low frequencies [14, 15], this work adapts the technology to accommodate ultrasound detection and to demonstrate its potential for photoacoustic imaging.

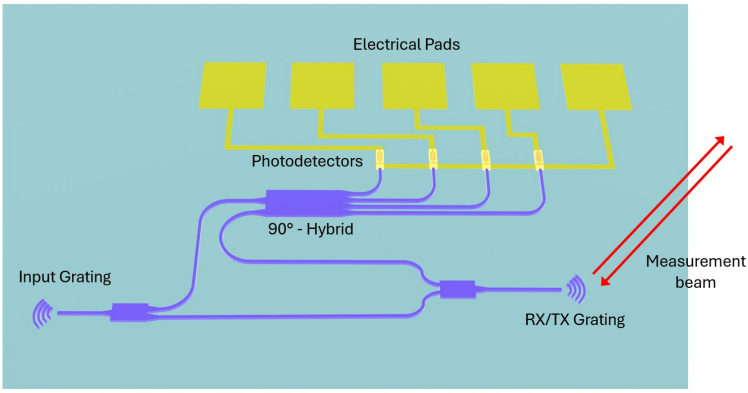

Figure 6: Layout of a silicon photonics-based implementation of a homodyne LDV. Light is coupled into the chip using the input grating coupler, then split into a measurement and reference arm. The measurement light is coupled in and out of the chip using the TX/RX Grating. The hybrid component combines the light in four different ways, and photodetectors convert these combinations into different currents, from which the displacement can be demodulated.

Results

Silicon photonics-based LDV for ultrasound detection

In order to enable ultrasound detection for photoacoustic imaging with a silicon photonics-based LDV, the system was developed with an extended bandwidth. A large bandwidth is crucial for achieving high-resolution photoacoustic imaging; however, the noise equivalent pressure of an LDV-based detection system increases rapidly at higher frequencies due to the lower displacement amplitudes associated with high-frequency vibrations. Therefore, the system was optimized to focus on the low ultrasound range with a useful bandwidth of up to around 3.5 MHz.

The silicon photonics-based LDV system demonstrated a noise floor comparable to that of commercial LDV systems, with estimations indicating noise levels close to the fundamental shot noise limit. In an attempt to further lower the detection limit, we theoretically explored the integration of Semiconductor Optical Amplifiers (SOAs) into the silicon photonics-based LDV. However, these theoretical estimates revealed that in most practical situations, incorporating an SOA generally did not significantly enhance the detection limit, primarily due to the phase noise introduced by the SOA.

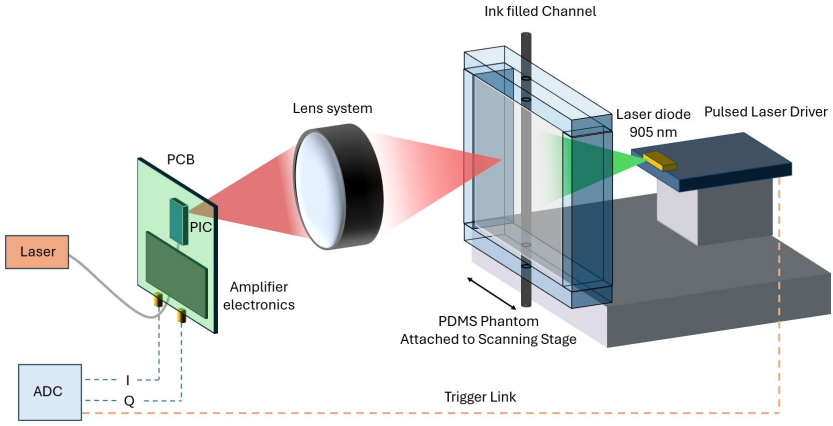

Figure 7: Schematic of the lab-based photoacoustic imaging demonstration.

Photoacoustic imaging with silicon photonics-based LDV

A lab-based system, as shown in Fig. 7, was developed to demonstrate contactless photoacoustic imaging using a silicon photonics-based LDV and a miniature excitation source. The LDV photonic integrated circuit (PIC) is wirebonded onto a printed circuit board (PCB) that houses the necessary amplifier electronics. After the photodetector signals are differentially amplified, resulting in an In-Phase (I) and Quadrature (Q) that describe the relative movement of the target. These signals are then digitized using an Analog-to-Digital Converter (ADC). A lens system focuses the LDV measurement light onto a phantom—a flat, polydimethylsiloxane (PDMS)-based model with an embedded channel.

The embedded channel, filled with an ink-water solution, acts as an absorber, generating photoacoustic signals upon pulsed illumination. A miniature excitation source was developed using a 905 nm laser diode or laserbar attached to a pulsed laser driver. When the pulsed laser source illuminates the phantom, the sudden, localized absorption generates photoacoustic waves that propagate towards the surface of the phantom. These waves induce small movements on the surface, which are then detected by the silicon photonics-based LDV system. A trigger link between the excitation source and the detection system ensures accurate timing of the photoacoustic signals. To facilitate scanning, the phantom and excitation source are mounted on a scanning stage, allowing the LDV to detect photoacoustic signals along a line across the surface of the phantom.

Fig.8a shows a cross-section of a single-channel phantom along with the scanning axis of the LDV over its surface. Using a step size of 125 μm, the LDV beam was scanned across the surface of the phantom. At each scanning location, the LDV recorded time traces of the surface velocity, as depicted in Fig.8b. This figure

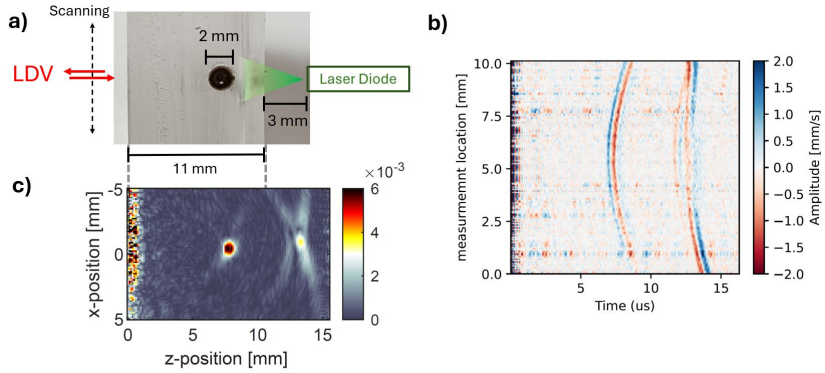

Figure 8: a) Cross-sectional view of a single-channel PDMS-based phantom, showing the LDV side, scanning axis, and laser diode excitation side. b) Surface velocity measured by the LDV at different locations along the scanning axis for 16 μs after an excitation pulse is fired, illustrating the varying arrival times of the photoacoustic signals at different positions. c) A photoacoustic reconstruction image created using the data from b) with a time-reversal reconstruction algorithm.

shows that the primary photoacoustic signal is detected between 6 and 10 μs after the pulse is fired. A secondary signal, representing a reflection of the acoustic wave within the sample, arrives after 12 μs. Utilizing this data, a time-reversal reconstruction algorithm was applied to create the 2D photoacoustic reconstruction image shown in Fig. 8c, which shows the origin of the photoacoustic signal and a shadow image due to the reflection. Similar reconstructions were performed with phantoms featuring channels at various depths and with different ink concentrations, as well as with phantoms having two channels. Additionally, it was demonstrated that using a laserbar could be more effective than a laser diode, owing to its specific illumination pattern.

Proposal of a scalable multibeam architecture

While a silicon photonics-based LDV layout can accommodate scaling to a few tens of beams, scaling up to hundreds of beams necessitates advanced packaging techniques or architectural innovations to manage or limit the number of electrical connections to the photonic integrated circuit (PIC). In this work, we propose an alternative architecture featuring a newly introduced component, the multibeam frequency shifter. This component shifts different sensing beams to distinct optical carrier frequencies, allowing the photodetector signals—which combine a local reference with the frequency-shifted measurement signals—to be multiplexed over an electrical connection. This approach could potentially reduce the number of required electrical connections by up to an order of magnitude.

The multibeam frequency shifter takes a single frequency input and generates multiple output waveguides, each carrying a differently frequency-shifted beam. It achieves this by dividing the single-frequency light across an array of modulators. By emulating the modulation typically performed by an acousto-optic modulator using this array of on-chip modulators, different harmonics of the modulation can be coupled to various outputs of a star coupler. The working principle of this component has been explored both theoretically and through simulations.

While simulations suggest that this architecture and component hold promise, implementing it represents a significant shift in the detection system.

Conclusion

This work has demonstrated the adoption of silicon photonic-based LDVs for contactless photoacoustic imaging in a lab-based system, showcasing 2D photoacoustic imaging capabilities for simple homemade phantoms. However, transitioning to real-life applications presents several challenges. One such challenge is the reduced collection efficiency of the LDV due to non-specular reflection from the sample's surface.

A potential solution is to employ high numerical aperture (NA) optics and automatic focusing techniques to optimize collection efficiency for non-specular and moving surfaces. Another significant challenge is scaling the system to handle hundreds of beams, which would eliminate the need for scanning. This work proposes a novel architecture that reduces the number of required electrical connections, while alternative approaches could involve advanced packaging techniques to accommodate a large number of electrical connections.

Overall, this research establishes a foundation for future advancements in developing a contactless photoacoustic imaging system using silicon photonics-based LDVs.

1

Introduction

In the modern information age, the integration of discrete electrical components into chip-based systems has revolutionized electronics. This shift, driven by advancements in Complementary Metal-Oxide-Semiconductor (CMOS) processing, has enabled the miniaturization of electronic devices and increased their performance. Complex electronic circuits that once required multiple separate components can now be fabricated on a single chip. This has led to the proliferation of powerful, compact, and energy-efficient electronic devices enabling the current digital age.

Similarly, the field of photonics has experienced a transformative shift with the advent of Photonic Integrated Circuit (PIC). Discrete optical components such as filters and waveguides can be integrated into a photonic chip using the same techniques and machinery developed for CMOS processing. This integration has paved the way for compact, efficient, and scalable solutions for manipulating light on a chip. Initially, innovation in this field was mostly driven to advance

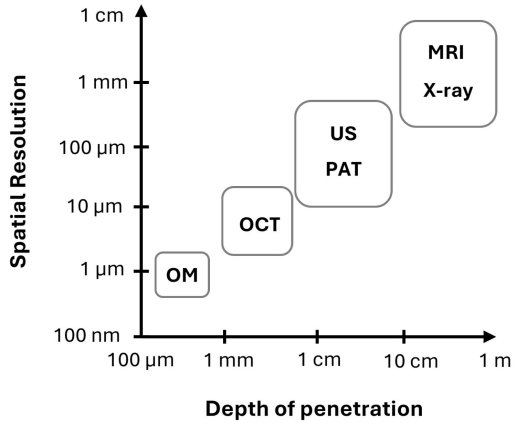

Figure 1.1: Overview of different biomedical imaging modalities; optical microscopy (OM), optical coherence tomography (OCT), ultrasound imaging (US), photoacoustic tomography (PAT), magnetic resonance imaging (MRI), X-ray imaging. These techniques are organized in terms of their typical resolution and penetration depth. Adapted from [23]

optical communication. Now, innovation is happening across a broad range of new applications beyond established tele- and datacom applications, such as LiDAR [18, 19], optical computing [20], sensing [21], and beyond [22]. One medical application is medical imaging, which is one of the most crucial tools in the biomedical field. It offers vital insights for diagnosis, treatment planning, and monitoring of various medical conditions. Over the past decade, photoacoustic imaging has become a fast-developing emerging technique that enables imaging capabilities beyond conventional ones.

The combination of these two innovative fields, silicon photonics, and photoacoustics, opens up potential for further advancements and novel applications.

1.1 Medical Imaging

A wide range of imaging modalities exist, each with unique characteristics and applications [23]. Fig. 1.1 illustrates several common imaging techniques, arranged according to their depth of penetration and resolution. Generally, techniques with lower penetration depth provide higher resolution, and vice versa.

Optical Microscopy (OM) techniques, which detect reflected or transmitted light by a sample, offer cellular-level resolution, but the penetration depth is limited by scattering and absorption. This limitation confines their use to thin, transparent

samples.

Optical Coherence Tomography (OCT), utilizes low-coherence interferometry, where light is partially reflected by tissue structures, and the interference of the reflected light is used to create cross-sectional images. OCT extends beyond the shallow penetration depth of optical microscopy, reaching up to a few millimeters with micrometer-scale resolution. This capability makes OCT ideal for mesoscopic-scale studies, such as routine retinal imaging in ophthalmology [24] and superficial skin layer examination in dermatology [25].

At the macroscopic scale, imaging techniques like Magnetic Resonance Imaging (MRI) and X-ray are employed to visualize larger structures such as organs. X-rays, with their high energy, can pass through most body tissues, creating contrast from the shadows of denser structures that absorb more X-rays. However, the ionizing nature of X-rays can be harmful with prolonged or large exposures. MRI, on the other hand, provides superior contrast in soft tissues without ionizing radiation. It leverages the property of hydrogen atoms absorbing and re-emitting Radio Frequency (RF) signals in a magnetic field. Despite its benefits, MRI is both expensive and time-consuming.

Bridging the gap between OCT and macroscopic techniques are Ultrasound Imaging (US) and Photoacoustic Tomography (PAT), as shown in Fig. 1.1. These methods offer a balance of resolution and penetration depth, making them versatile for a wide range of applications. Ultrasound imaging employs high-frequency sound waves that are transmitted into the body; the reflected waves from different tissues are then detected and converted into images based on the speed of sound and acoustic impedance differences. It is widely used to image tendons, muscles, joints, and other internal structures.

Over the past decades, photoacoustic imaging has rapidly emerged as a popular technique [26]. Combining optical excitation with acoustic detection, photoacoustic imaging can penetrate deeper than traditional microscopy and OCT, while still utilizing optical properties for contrast. Unlike ultrasound, which relies on acoustic impedance differences for structural information, photoacoustic imaging derives contrast from varying absorption characteristics within the sample. By using multiple excitation wavelengths, absorption profiles at different wavelengths give spectroscopic absorption data which can be used to extract and quantify absorbers concentration.

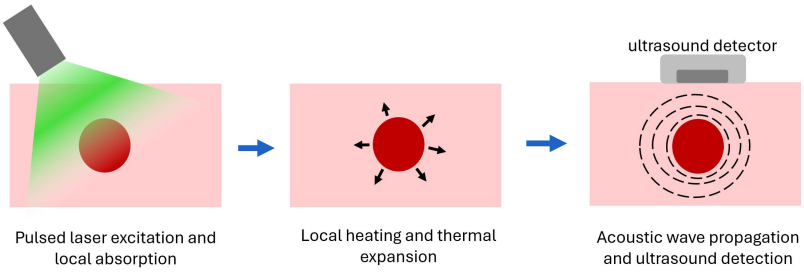

Figure 1.2: Photoacoustic effect under pulsed illumination

1.2 Photoacoustic Imaging

The photoacoustic effect was discovered around 1880 by Alexander Bell [27]. After his invention of the telephone, he began experimenting with the idea of using light for the transmission of speech. In 1880, he demonstrated a setup where sunlight was directed onto a flexible mirror, which focused the light onto a black solid inside a conical resonator attached to an earpiece. Speaking into a mouthpiece attached to the mirror caused vibrations, modulating the light intensity focused on the solid. This modulated illumination generated acoustic waves, which were then detected with a hearing tube near the solid [27]. Subsequent demonstrations showed photoacoustic generation in gas cells, and a theoretical model was developed [28–30].

In these demonstrations, the absorption of modulated light caused heating and expansion of the gas or air around the sample, generating acoustic vibrations. A second mechanism, dominant under pulsed illumination, directly couples the heat energy into a pressure wave [31–33]. This thermoelastic process forms the basis for most modern photoacoustic imaging techniques and is depicted in fig. 1.2. While a detailed mathematical explanation will be presented in Chapter 2, a brief overview of this effect is as follows:

Sudden, localized heating from the absorption of pulsed energy generates a pressure buildup governed by the thermal expansion coefficient. This pressure results in the emission of an acoustic wave. When the optical pulse duration is shorter than the heat diffusion time, and the stress relaxation time, the effect is most efficient. The acoustic wave can then be detected at the sample's surface.

By detecting the acoustic waves at multiple locations on the surface, the origin of the waves can be determined by monitoring the time delay between their arrivals. With a large array of detectors, reconstruction algorithms can create a photoacoustic image, revealing where the pulsed laser light was absorbed.

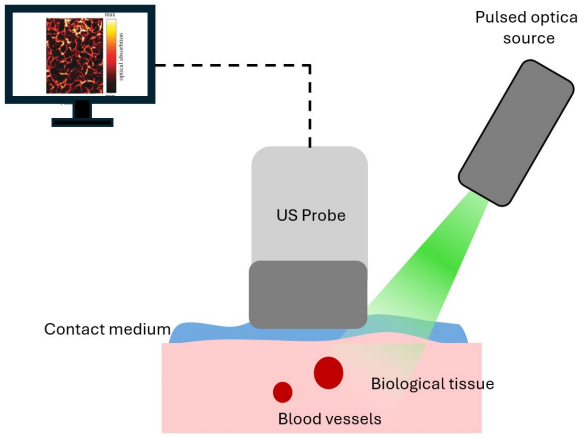

Figure 1.3: A schematic of a conventional imaging system using a pulsed laser as the excitation source, and an ultrasound probe in contact with the sample facilitated by a coupling gel.

A conventional medical photoacoustic tomographic imaging system can be depicted as Fig. 1.3. A high-power pulsed laser source is directed toward the sample, where absorbers convert this energy into acoustic waves, typically detected by an array of ultrasound transducers in contact with the sample. A contact medium is generally applied to ensure effective ultrasound transmission. In the second chapter, we will delve deeper into the theory of photoacoustics and common photoacoustic imaging modalities.

Photoacoustic excitation with multiple wavelengths sequentially excites different absorbers, providing spectroscopic information from within the sample. Various wavelengths can be used depending on the targeted chromophores. In-vivo chromophores can include myoglobin, water, lipids, melanin, and hemoglobin, which absorbs light in the visible and near-infrared spectra [34]. This capability allows for generating angiographic images and mapping blood vessel structures in tissue. Multi-wavelength excitation can differentiate between oxygenated and deoxygenated hemoglobin, mapping tissue oxygenation levels.

These imaging techniques have been applied to study a broad range of tissues and diagnose many medical conditions. Applications include cancer detection, blood oxygenation monitoring, vascular structure visualization, and tissue viability assessment in ophthalmology and brain imaging. Fig. 1.4 shows some specific examples including: a) the imaging of a nevus on the forearm to assess its size and depth [35], b) imaging of the vasculature in the cornea for disease diagnosis and progression [36], and c) evaluating burn wounds to monitor healing [37].

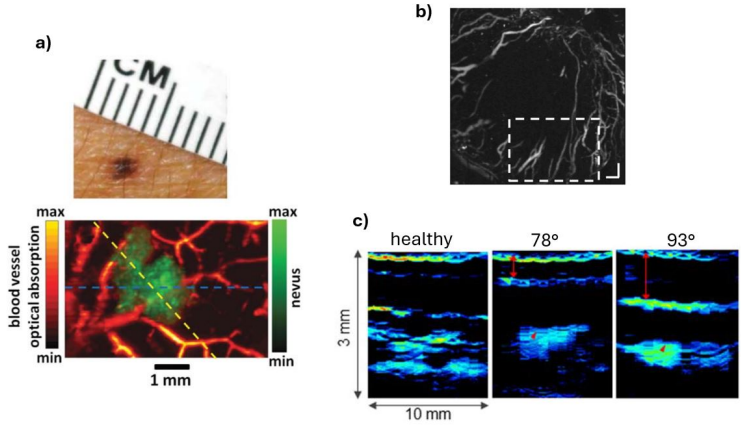

Figure 1.4: Examples of photoacoustic imaging applications. a) Imaging of a nevus on the forearm to asses the size and depth. Reproduced from [35]. b) Imaging of vascularization in the cornea. Reproduced from [36]. c) Demonstration in which the severity and depth of a burn wound were assessed using photoacoustic imaging. Reproduced from [37].

1.2.1 Contactless Photoacoustic imaging with a Laser Doppler Vibrometer

Photoacoustic detection usually requires contact with the sample, often facilitated by coupling gels. However, this contact can be uncomfortable for patients and poses risks of contamination and infection [6], especially in wound imaging or intraoperative settings. A promising non-contact alternative is Laser Doppler Vibrometry (LDV).

LDV is an optical interferometric technique for measuring surface vibrations. A probe beam is directed at the target, after reflection from the target, it is combined with a local oscillator on photodetectors. By combining the two beams on a photodetector, interference effects cause a variation in the photocurrent when there are changes in the relative path lengths of the beams, allowing for the precise detection of target movements. Since ultrasound waves induce surface movements, these can be detected using LDV. Figure. 1.5 depicts a homodyne LDV schematic.

This non-contact approach mitigates risks of contamination and mechanical coupling artifacts, which can degrade photoacoustic image quality. Traditional LDV systems are limited to a few beams and require scanning over the sample surface, increasing cost and complexity while reducing imaging speed. A potential solution is integrating LDV architectures into a photonic integrated chip, enabling the use of multiple sensing beams without the bulk and expense of discrete optical components.

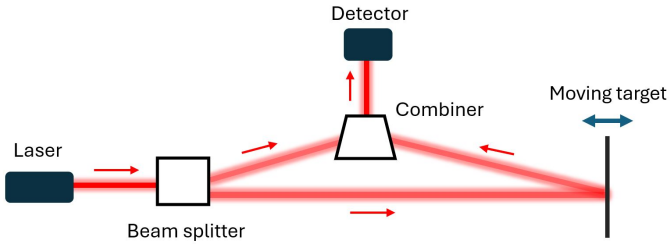

Figure 1.5: Schematic of a homodyne LDV. Laser light is split into a reference beam and a beam directed towards a moving target. After reflection from the target, the light is combined with the local oscillator on a detector.

1.3 Silicon Photonics

Integrated photonics is the field of guiding and manipulating light on an integrated circuit. By leveraging established lithographic techniques from the microelectronics industry, miniature circuits can be patterned for a variety of material platforms [16, 17].

Just like optical fibers, photonic integrated circuits (PICs) operate based on the principle of refractive index contrast. By carefully designing the geometry and materials of the photonic structures, light can be confined and guided through the chip, enabling complex optical functionalities. Silicon, in particular, has emerged as a favored material for PICs due to its high refractive index contrast with silicon dioxide. This allows for tight confinement of light and the creation of high-density photonic circuits. Silicon is also advantageous because it supports transmission at telecom wavelengths (1310 nm and 1550 nm), which are suitable for a wider variety of applications. For applications that require wavelengths outside of the silicon transmission band, alternative platforms exist that offer a solution (e.g. silicon nitride platforms enable transmission in the visible spectrum). Beyond passive optical circuits, integrated optical circuits are generally designed to include a multitude of active components such as photodetectors, lasers, and modulators. Various techniques and materials have been developed to enhance the silicon platform. One notable advancement is the epitaxial growth of germanium on silicon, which enables the fabrication of on-chip detectors. By integrating these advanced components, we can develop more sophisticated and versatile photonic systems, analogous to the advancements seen in electronic integration. These advancements have opened the door to a broad range of applications, including LiDAR [18, 19], optical computing [20], sensing technologies [21], including LDV. The infrared transmission band of silicon is particularly well-suited for applications that require coupling light into free space while adhering to eye-safety limits. This is because

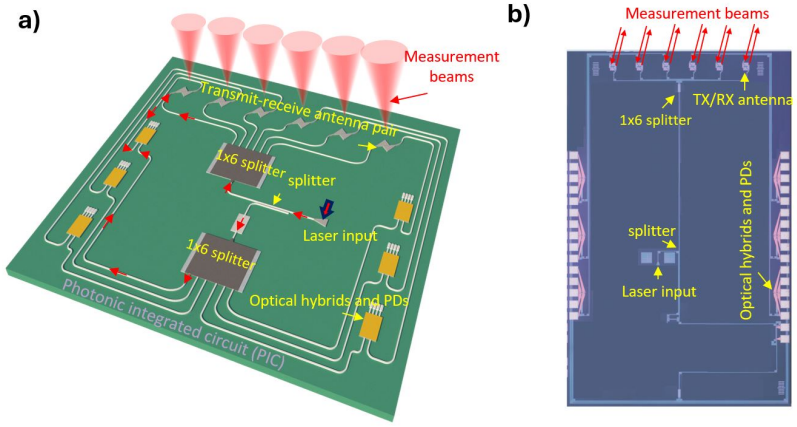

Figure 1.6: a) Schematic and b) Picture of a 6-beam silicon photonics-based LDV which was developed and used in [15] to measure the pulse wave velocity from the artery. Reproduced from [15]

operating at infrared wavelengths allows for 10-20 times higher permissible power compared to visible wavelengths, enabling higher power for such applications.

Over the past decade, our group has demonstrated homodyne LDV layouts on the silicon photonics platform [15] (one example depicted in Fig. 3.19). While these have been used to measure vibrations up to around 100 kHz, in this work, this technology has been adapted to detect ultrasounds for photoacoustic imaging and has been implemented in a photoacoustic system.

1.4 Research Objective and Outline

The goal of this work is to enable compact and contactless photoacoustic imaging using silicon photonics-based LDV. Photoacoustic imaging is an emerging technology, transitioning into commercialization and an active field of research. Despite numerous developments on the system side, progress in contactless photoacoustics has been limited. Proposed solutions often fail to be scalable for detection at multiple locations while maintaining compact size. This work builds on recent advancements and demonstrations of silicon photonics-based LDV to enable non-contact photoacoustic imaging. Although silicon photonics-based LDVs have been demonstrated, these implementations have been limited to measuring relatively large vibrations at low frequencies. This project aims to implement a silicon photonics-based LDV for ultrasound detection and demonstrate its capability to measure photoacoustic vibrations, culminating in a lab demonstration of photoacoustic imaging with a

silicon photonics-based LDV. Finally, we discuss the path forward and challenges for silicon photonics-based LDVs and propose a scalable architecture for multibeam LDVs with hundreds or thousands of sensing beams.

Chapter 1 situated photoacoustic imaging within the broader landscape of current medical imaging techniques and introduces photonic integration as a solution for building compact, contactless detectors.

Chapter 2 explores the physics underlying the photoacoustic effect, building on the foundation of prior research and established principles. It briefly presents an overview of various photoacoustic imaging modalities and explains image reconstruction techniques. It also provides an overview of contactless demonstrations, highlighting the need for a scalable contactless solution.

Chapter 3 begins by outlining the prior art, specifically the working principles and design requirements for a silicon photonics-based LDV system. The chapter then transitions into novel contributions, examining the performance of silicon photonics-based LDVs within the contexts of photoacoustic imaging and ultrasound. After explaining the origins of non-linearities and the adopted demodulation method, the discussion focused on the characterization of a silicon photonics-based LDV for ultrasound detection. Additionally, the chapter provides a theoretical analysis of optical amplifiers specifically tailored for silicon photonics-based LDV systems.

The following chapter, Chapter 4. presents and discusses the implementation of a first-of-its-kind lab demonstration of contactless photoacoustic imaging using a silicon photonics-based LDV and a small excitation source. It concludes with a discussion of the challenges involved in moving towards in-vivo measurements.

Chapter 5 tackles the challenge of scaling the number of sensing beams. It begins by explaining the scaling problem and proposes an alternative architecture using a new component: the multibeam frequency shifter. The chapter discusses the theory and working principle behind this component, design methods, and simulation results indicating its performance.

The final chapter summarizes the key conclusions from this work and provides an outlook for future developments in the field of silicon photonics-based LDVs and photoacoustic imaging.

1.5 List of Publications

Patent applications

1. **E. Dieussaert**, R. Baets, Y. Li, "Photonic integrated circuit for multiple frequency shifting of light," publication number: US20240168223A1, U.S. Patent and Trademark Office, published on 23 May, 2024.

Publications in international journals

1. **E. Dieussaert**, R. Baets, H. Jans, X. Rottenberg, Y. Li "Non-contact photoacoustic imaging with a silicon photonics-based Laser Doppler Vibrometer," *Scientific Reports*, vol. 14, no. 1, Article 22953, 2024.

2. **E. Dieussaert**, R. Baets, Y. Li, "On-chip multi-beam frequency shifter through sideband separation," *Optics Express*, vol. 31, no. 18, pp. 29213–29227, Aug. 2023.

3. Y. Li, **E. Dieussaert**, "A Compensation Method for Nonlinearity Errors in Optical Interferometry," *Sensors*, vol. 23, no. 18, Article 7942, 2023.

4. Y. Li, **E. Dieussaert**, R. Baets, "Miniaturization of Laser Doppler Vibrometers—A Review," *Sensors*, vol. 22, no. 13, Article 4735, 2022.

Publications in international conferences

1. **E. Dieussaert**, R. Baets, Y. Li, "Scaling Silicon Photonics-based Laser Doppler Vibrometry with Multi-Beam Frequency Shifters," in *2024 IEEE Silicon Photonics Conference (SiPhotonics)*, 2024, pp. 1-2.

2. **E. Dieussaert**, X. Rottenberg, R. Baets, Y. Li, "Miniature and non-contact photoacoustic system using silicon photonics-based Laser Doppler Vibrometer and compact excitation source," presented at the *European Conference on Integrated Optics (ECIO)*, 2023.

3. **E. Dieussaert**, R. Baets, Y. Li, "Silicon photonics based laser doppler vibrometer for non-contact photoacoustic sensing," in *Smart Photonic and Optoelectronic Integrated Circuits 2023*, S. He and L. Vivien, Eds., vol. 12425, International Society for Optics and Photonics, SPIE, 2023, pp. 124250C.

4. Z. Yang, **E. Dieussaert**, R. Baets, Y. Li, "Comparison between laser doppler and sagnac," presented at the *IEEE Benelux Photonics Chapter-Annual Symposium 2022*, pp. 78-81, 2022.

5. **E. Dieussaert**, R. Baets, Y. Li, "Proposal for non-contact photoacoustics using silicon photonics-based Laser Doppler Vibrometers," presented at the *IEEE Benelux Photonics Chapter: Annual Symposium 2022*, 2022.

6. I. Ansari, G. F. Feutmba, **E. Dieussaert**, J. P. George, J. Beeckman, D. Van Thourhout, "PZT based actuator for an efficient electro-optomechanical interaction in Si-photonic integrated circuits," in *Integrated Optics: Devices, Materials, and Technologies XXVI*, S. M. García-Blanco and P. Cheben, Eds., vol. 12004, International Society for Optics and Photonics, SPIE, 2022, pp. 1200411.

7. **E. Dieussaert**, Y. Li, G. Morthier, R. Baets, "Influence of optical amplifiers for on-chip homodyne laser Doppler vibrometers," *Journal of Physics: Conference Series*, vol. 2041, no. 1, pp. 012005, Oct. 2021.

2

Biomedical photoacoustics and contactless detection

2.1 Introduction

The photoacoustic process is a complex due to the interplay of pressure, temperature, optical absorption, density,... Understanding the physics is required to fully grasp the working principle behind photoacoustic imaging techniques and can clarify

several system design decisions for photoacoustic systems, including those in the remainder of this work.

In this chapter, the photoacoustic process is mathematically described, largely following the theory as explained in the book '*Photoacoustic Imaging and Spectroscopy*' of Wang et al. [38]. Starting from conservation equations, two coupled equations are derived that can describe general photoacoustic effects. In order to derive analytical solutions that would allow photoacoustic imaging, we assume working in the instantaneous heating regime. In these assumptions, equivalent to short pulse excitation, the generated pressure profile right after the pulse, reflects the absorption of the excitation light. This not only allows for analytical prediction of the generated pressure but also allows the reconstruction of the absorption profile when detecting the pressure wave at different locations, forming the basis of photoacoustic imaging. After this mathematical description, we shortly look at different photoacoustic imaging modalities and we describe how multi-wavelength photoacoustic enables quantification of absorbers concentration, demonstrated by providing a linear model for the quantification of the oxygenation of blood. In the last part of this chapter, we take a look at the state of the art of contactless photoacoustic imaging techniques and describe how LDV can be used for non-contact photoacoustic imaging.

2.2 Photoacoustic principles

The photoacoustic process is initiated because light is absorbed and converted into heat. This variation in heat deposition over time is the source term for the photoacoustic effect. The heat energy deposited per unit volume and time $H(\mathbf{x}, t)$ $[\mathrm{J/cm^3}]$ can be written in terms of the optical absorption coefficient profile $\mu_a(\mathbf{x})[1/\mathrm{cm}]$ and the light fluence or irradiance $\Phi(\mathbf{x}, t)$ $[\mathrm{J/cm^2}]$.

$$H(\mathbf{x}, t) = \mu_a(\mathbf{x})\Phi(\mathbf{x}, t) \tag{2.1}$$

2.2.1 Photoacoustic Wave Equation

The pressure and temperature variations due to the photoacoustic process are generally much smaller compared to their ambient values. As such, the linearized mass, momentum, and energy conservation equations for inviscid flows can be used as a starting point to describe the process. In the following expressions, a subscript 0 for a variable indicates an ambient quantity, such as T_0 being the background temperature, while without a subscript it describes the variation. The ambient flow velocity is assumed to be zero, $v_0 = 0$.

The mass conservation equation describes how the change in density variation ρ of a fluid over time t, relate to the divergence of the velocity field $\mathbf{v}$

$$\partial\rho/\partial t = -\rho_0 \nabla \cdot \mathbf{v}. \tag{2.2}$$

The momentum conservation equation relates the change in momentum (represented by $\rho_0(\partial\mathbf{v}/\partial t)$)to the gradient of pressure p

$$\rho_0(\partial\mathbf{v}/\partial t) = -\nabla p. \tag{2.3}$$

The energy conservation equation describes how the change in entropy s (related to temperature T evolves over time, considering heat conduction (term with κ) and any internal heat generation H

$$\rho_0 T_0(\partial s/\partial t) = \nabla \cdot (\kappa \nabla T) + H. \tag{2.4}$$

The heat source H changes the temperature, density, and pressure following the thermodynamic relation $\rho = \rho_0 K_T p - \rho_0 \beta T$, where K_T is the isothermal compressibility and β is the volume thermal expansivity.

Now, by taking the time derivative of equation 2.2 and substitution of 2.3, this gives

$$(\partial^2/\partial t^2)(\rho_0 K_T p - \rho_0 \beta T) = \nabla \cdot (\nabla p). \tag{2.5}$$

Another thermodynamic relation, $\rho_0 T_0 s = \rho_0 C_p T - T_0 \beta p$, can be used to rewrite Equation 2.4 as

$$(\partial/\partial t)(\rho_0 C_p T - T_0 \beta p) = \nabla \cdot (\kappa \nabla T) + H. \tag{2.6}$$

Equations 2.5 and 2.6 form a set of two coupled equations, describing the pressure and temperature perturbations. When the thermal conduction cannot be neglected, they must be solved together.

Generally, these need to be solved together to accurately describe the photoacoustic process, however, when the thermal conduction can be neglected $\nabla \cdot (\kappa \nabla T)$, these equations can be uncoupled. This is accurate when in the so called thermal confinement regime. This regime holds when the characteristic time of the heat τ_h is much longer compared to the acoustic propagation time $\tau_h \gg d/v_s$. The acoustic propagation time is estimated by a characteristic length d of the heat source and the speed of sound v_s. In this regime, these two equations can be combined and written as the photoacoustic wave equation.

$$\frac{1}{v_s^2}\frac{\partial^2 p}{\partial t^2} - \rho_0 \nabla \cdot \left(\frac{1}{\rho_0}\nabla\right) p = \frac{\beta}{C_p}\frac{\partial H}{\partial t}, \tag{2.7}$$

Assuming a uniform ambient density $\rho_0(\mathbf{x})$ =constant, this yields:

$$\left(\frac{\partial^2}{\partial t^2} - v_s^2 \nabla^2\right) p = \Gamma \frac{\partial H}{\partial t}, \tag{2.8}$$

where Γ is the Grüneisen parameter, a dimensionless quantity representing the efficiency of conversion from absorbed energy to pressure, described as:

$$\Gamma = \frac{v_s^2 \beta}{C_p}.$$

2.2.2 Instantaneous Heating

Now, assume a stationary source, described as $H(x,t) = h_x(x)h_t(t)$. Consider $h_t(t)$ to be a pulse in time with $\int h_t dt = 1$. Now, when this pulse (with length τ_p is much faster than the acoustic travel time $\tau_p \ll d/v_s$, the temporal part of the heat source can be approximated by a delta function $h_t(t) = \delta(t)$. In this regime, also known as the stress confinement regime, the heat energy is deposited before any notable change in mass density can occur. Now, thermodynamic relation $\rho = \rho_0 K_T p - \rho_0 \beta T$ with $\rho = 0$ describes the initial pressure:

$$p|_{t=0} = (\beta/K_T)T = \Gamma h_x \tag{2.9}$$

With these assumptions, Equation 2.8 has a source term $\Gamma h_x \partial\delta(t)/\partial t$. This is equivalent to an initial value problem described by:

$$\left(\frac{\partial^2}{\partial t^2} - v_s^2 \nabla^2\right) p = 0, \tag{2.10}$$

and with initial conditions

$$p|_{t=0} = \Gamma h_x, \text{ and } \partial p/\partial t|_{t=0} = 0. \tag{2.11}$$

Now, with the assumption of instantaneous heating, this initial value problem describes the photoacoustic effect and allows for a relatively simple model for calculating the resulting pressure wave. Moreover, by recording the pressure in various locations, the initial pressure distribution and absorption profile can be estimated, thus reconstructing a photoacoustic image.

2.2.3 Image reconstruction

A broad range of imaging algorithms have been developed that try to reconstruct the initial pressure of the inverse value problem by using data collected from a limited number of detectors. Various categories of reconstruction algorithms exist, each with distinct approaches to solving imaging problems. The main categories include Back Projection, which directly projects collected data back into the image space; Time Reversal (TR), which uses the principles of wave physics to refocus waves back to their origin; Fourier Transform methods, which operate in the frequency domain; and Model-Based methods, which employ mathematical models to iteratively reconstruct images, handling complex scenarios with higher accuracy. Each method is tailored to specific imaging needs, balancing simplicity and precision.

In the remainder of this work, we have opted to work with a time reversal algorithm [39]. While it may not be the most computationally efficient algorithm, its underlying concept is simple, and it provides accurate reconstruction in heterogeneous media.

Time reversal relies on the fact that the wave equation in a lossless medium remains unchanged if time t is replaced by $-t$. This implies that if we record a wave field as it propagates through a medium and then play back the recorded signals in reverse order, the wave field will retrace its path and focus back on the original source location. For instantaneous photoacoustic, this means that when the pressure field is recorded over a surface enclosing the absorber locations, playing back the recorded signals until t=0 results in the identical $p|_{t=0}$ representation inside the enclosed volume. In reality, the pressure is recorded in a discrete number of locations, often not enclosing the absorber locations. This causes limitations on image resolution image quality similar to other imaging algorithms.

In practice, this means that we need to use the recorded pressure measurements in time-reversed order as a time-varying Dirichilet boundary condition imposed at the detector locations in an acoustic simulation. First of all, accurate timing is crucial to ensure the simulation halts precisely at $t = 0$, thereby allowing for an accurate approximation of the initial pressure. Second of all, one needs to know or assume the speed of sound within the simulation region. In general, for tissue this can be assumed at around $1500\ m/s$.

Image Resolution

One of the key parameters for photoacoustic imaging is the spatial resolution. In the case of unfocused optical excitation and instantaneous heating (as explained in Section 2.2.2), different characteristics of the detector and detector array determine

the spatial resolution such as the finite frequency detection bandwidth and the number and position of the detectors.

Bandwidth limitations affect the timing accuracy of the detected signals, leading to uncertainty in determining the exact arrival time of the acoustic waves. This timing uncertainty, in turn, causes an imprecision in calculating the distance the wave has traveled from its origin to the detector.

Consider a point absorber in a medium that is photoacoustically excited, meaning it absorbs light and generates an acoustic wave—a pressure pulse—at a specific location. Ideally, this pressure pulse would be an infinitely small, sharp delta function that travels through the medium. However, when this sharp signal reaches a detector with a finite bandwidth, the detector cannot perfectly capture the abrupt changes in the signal due to its limited frequency response. Instead of detecting the sharp delta pulse as it is, the impulse response of the detector system is recorded, which causes a finite point spread function (PSF) for the reconstruction. Analytical calculations show that the PSF of a lowpass bandwidth-limited system (but perfect aperture) with cutoff frequency f_c, has a full-width half-maximum (FWHM) of $0.8\lambda_c$ [38, 40], which represents the bandwidth limited resolution.

The second factor that determines the spatial resolution is the number and position of the detectors of the detection system. While in a perfect situation, the point source of photoacoustic signals is fully enclosed by an infinite amount of detectors, in reality, only a limited aperture is represented by the detector array. For a detector array, both the physical size of the array and the spacing between individual detectors, known as the detector pitch will eventually determine the resolution. This limitation is similar to array factors in electromagnetic systems, where the arrangement of the array elements affect the system's directional sensitivity and resolution. For a linear array, the pitch size is generally chosen to be below λ_c, and the relation between the numerical aperture of the detector array and lateral resolution can be expressed as $0.61\lambda_c/NA$ [38]. The axial resolution generally is limited by the bandwidth-limited resolution.

Note that when the excitation light is focused (in some imaging modalities as explained in the next section), the resolution is not only determined by the ultrasound detector array characteristics.

2.3 Photoacoustic imaging modalities

Several PAI modalities have been developed to exploit these techniques for various applications. The most prominent ones are indicated in Fig. 2.1, including

Optical-Resolution Photoacoustic Microscopy (OR-PAM), Acoustic-Resolution Photoacoustic Microscopy (AR-PAM) and Photoacoustic Tomography (PAT). These imaging modalities generally use pulsed excitation to ensure the assumption of instantaneous heating is valid. This makes the conversion from optical energy to acoustic energy relatively efficient and, as discussed in the previous section, allows for retracing the origin of the photoacoustic wave.

Optical-Resolution Photoacoustic Microscopy (OR-PAM)

Optical-Resolution Photoacoustic Microscopy (OR-PAM) achieves high spatial resolution by focusing the excitation light tightly to a small spot as indicated in Fig. 2.1a, typically on the order of micrometers.

In OR-PAM, the lateral resolution is primarily determined by the optical focus, while the axial resolution is governed by the detection bandwidth limitation of the detectors (as explained in the previous section). Because the spatial coherence of incoming wavefronts is lost rapidly for propagation in highly scattering samples, this method generally has a limited imaging depth. This modality is particularly effective for imaging superficial structures within the optical diffusion limit, such as microvasculature, single cells, and subcellular structures. OR-PAM is well-suited for high-resolution studies in small animal models and in vitro samples due to its ability to provide detailed optical absorption contrast at the cellular level [41].

Acoustic-Resolution Photoacoustic Microscopy (AR-PAM)

Acoustic-Resolution Photoacoustic Microscopy (AR-PAM), unlike OR-PAM, achieves its lateral resolution through the focusing of ultrasonic waves rather than the optical focus. As seen in fig. 2.1b, an ultrasound transducer (UT) is focused within the sample, while the light is diffusely directed towards the focus region of the ultrasound detector.

This allows AR-PAM to image deeper into tissues, beyond the optical diffusion limit, while still maintaining relatively high resolution when using high bandwidth detectors. The lateral resolution in AR-PAM is determined by the focal spot size of the ultrasonic transducer, and the axial resolution remains governed by the bandwidth limitation. AR-PAM is advantageous for imaging larger and deeper structures, such as tissues and organs, providing valuable information in preclinical and clinical studies where penetration depth is critical [41].

Photoacoustic Tomography (PAT)

The term Photoacoustic Tomography (PAT) and AR-PAM are often mixed throughout the literature. Here, we use the term PAT when referring to a system in which the acoustic resolution is obtained by an array of acoustic detectors, while for AR-PAM we considered a single focused detector. PAT extends the capabilities

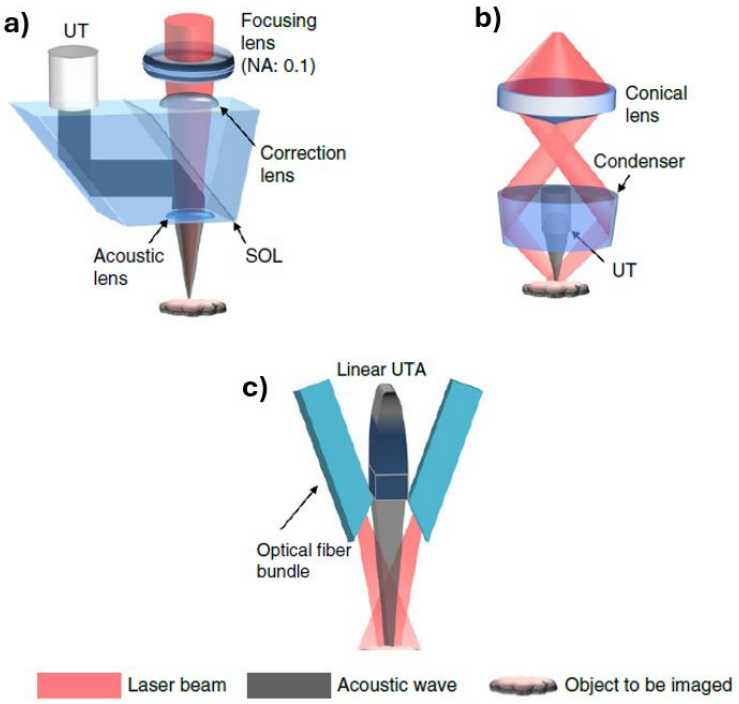

Figure 2.1: Shematic of prominent biomedical photoacoustic imaging modalities; a) OR-PAM setup, b) AR-PAM and c) PAT. Figure reproduced from [2]

of PAI to volumetric imaging, providing 2D or 3D visualization of tissues. PAT systems use an array of ultrasonic transducers to capture photoacoustic signals from locations around the object and light diffusely directed toward the sample. Fig. 2.1c shows a PAT system using a linear ultrasound array, typically used to create 2D PAT images. As mentioned in the previous section, reconstruction algorithms, such as the time-reversal algorithm can use the recorded data to reconstruct a photoacoustic image. This modality allows for imaging at greater depths to PAM, albeit with typically lower spatial resolution. PAT is highly effective for imaging whole organs, vascular networks, and tumor environments in vivo [2].

While the field of view of PAM systems is limited and generally requires scanning to create a useful image, PAT can acquire images with minimal or no scanning because of the use of an array of detectors. This makes PAT the preferred imaging modality for many in-vivo applications.

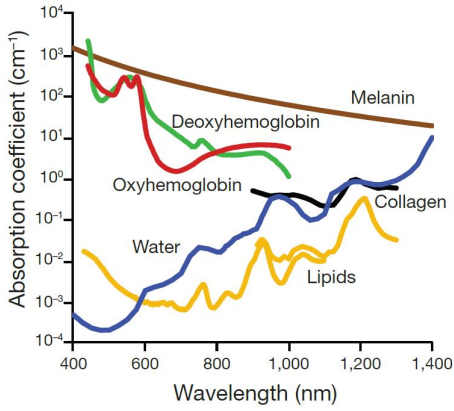

Figure 2.2: Absorption spectra of the common endogenous chromophores. Reproduced from [34]

2.4 Multi-wavelength Photoacoustics

In Multi-Wavelength Photoacoustics, the sample is sequentially illuminated with laser pulses at different wavelengths. Each wavelength is selected based on the absorption characteristics of specific chromophores or absorbers of interest, such as hemoglobin, melanin, lipids, and water. The generated photoacoustic signals at each wavelength are detected and used to construct images that reflect the spatial distribution of the absorbers.

As shown in Fig. 2.2, different absorbers in in-vivo samples have distinct absorption spectra [34]. By analyzing the photoacoustic signals and images at multiple wavelengths and comparing the amplitude, it is possible to extract quantitative information about the concentration and distribution of these absorbers.

One of the most significant applications is the determination of oxygenation inside the tissue [3]. Oxygenated hemoglobin (HbO_2) and deoxygenated hemoglobin (HbR) have different absorption spectra, which enables the differentiation of oxygenated and deoxygenated blood by multi-wave photoacoustics.

Tissue oxygenation levels are crucial for accurate diagnosis and monitoring for various conditions, including tumor hypoxia, wound healing, and brain function.

A common approach to quantifying oxygenation is through a linear model [3]. In this model, the photoacoustic signals obtained at multiple wavelengths are used to solve for the concentrations of HbO_2 and HbR. The basic principle involves the Beer-Lambert law, which relates the optical absorption ε at wavelength λ_i to the concentrations of the absorbers C. Consider P_{λ_i} to describe the reconstructed initial

pressure for excitation with wavelength λ. As in section 2.2.2, the initial pressure can be expressed in terms of absorption, fluence and the Grüneisen parameter Γ:

$$P_{\lambda_i}(\mathbf{r}) = \Gamma\Phi(\lambda_i)(\varepsilon_{\text{HbR}}(\lambda_i)C_{\text{HbR}}(\mathbf{r}) + \varepsilon_{\text{HbO}_2}(\lambda_i)C_{\text{HbO}_2}(\mathbf{r})) \tag{2.12}$$

Now, consider the matrix P in which:

$$P = \frac{1}{\Gamma}\begin{bmatrix} P_{\lambda_1}(\mathbf{r})/\Phi(\lambda_1) \\ P_{\lambda_2}(\mathbf{r})/\Phi(\lambda_2) \end{bmatrix} \tag{2.13}$$

and

$$\varepsilon = \begin{bmatrix} \varepsilon_{\text{HbR}}(\lambda_1) & \varepsilon_{\text{HbO}_2}(\lambda_1) \\ \varepsilon_{\text{HbR}}(\lambda_2) & \varepsilon_{\text{HbO}_2}(\lambda_2) \end{bmatrix} \tag{2.14}$$

Then the concentrations can be estimated by finding the least square solution of the Beer-Lambert (Eq.2.12) for multiple wavelengths. This is easily implemented by calculating the Moore-Penrose inverse:

$$\begin{bmatrix} C_{\text{HbR}}(\mathbf{r}) \\ C_{\text{HbO}_2}(\mathbf{r}) \end{bmatrix} = (\varepsilon^T\varepsilon)^{-1}\varepsilon^T P, \tag{2.15}$$

In the most simple version of this model, the fluence between both wavelengths is assumed to be identical. More advanced versions of this linear model try to estimate the difference in fluence for both wavelengths.

2.5 Contactless photoacoustic imaging

Conventional photoacoustic imaging systems rely on contact-based ultrasound detectors to achieve highly sensitive detection of ultrasound waves. These detectors typically need to be in direct contact with the sample, often facilitated by a coupling medium. For many biomedical applications, this contact requirement is a significant drawback. Not only does it cause discomfort for patients, but it also increases the risk of contaminating the sample [6]. These drawbacks are especially problematic in situations involving sensitive or exposed samples, such as wound imaging or imaging during surgical procedures.

To address these issues, several techniques have been developed to enable contactless photoacoustic imaging. Air-coupled detection is challenging due to the impedance mismatch between tissue and air, as well as the absorption of ultrasound in air. This limits air-coupled detection to low-frequency acoustic waves, reducing its suitability for photoacoustic imaging.

Optical detection techniques offer a more promising alternative, with several different approaches being considered, each with its own benefits and drawbacks.

One approach is based on speckle pattern analysis of light reflected from the sample. The photoacoustic ultrasound wave induces movement on the sample's surface, altering the speckle pattern, which is typically recorded by a camera [7, 10]. This method provides a large field of view without the need for scanning. However, it suffers from low detection bandwidth and high sensitivity to spurious vibrations due to the limited frame rate of the cameras.

Another approach developed over the past decade, involves detecting changes in the refractive index caused by the photoacoustic effect. Known as Photoacoustic Remote Sensing (PARS), this technique uses confocally focused excitation and probe light inside the sample. When an absorber is present in the focal spot, the photacoustically generated pressure slightly changes the refractive index, allowing the detection of a small amplitude change in the reflected wave [9, 42]. Although PARS enables the creation of remote photoacoustic images with relatively high resolution, it has several drawbacks. It can only measure one location inside the sample at a time. Therefore, to achieve a 3D image, both 2D lateral and confocal axial scanning are required. This leads to extremely long measurement times, making it impractical for high-resolution imaging, especially for moving samples. Additionally, the imaging depth of PARS is limited by the optical mean free path of the probe beam, and an amplitude-based technique could be sensitive to stray light.

Interferometric techniques, such as homodyne or heterodyne Laser Doppler Vibrometry (LDV), represent another promising approach, less sensitive to stray light. These dedicated interferometers probe for changes in the optical path length, often from a measurement beam directed and reflected from the sample. Ultrasound waves in the sample generate small surface movements which can than be detected by the interferometer. These techniques seem promising due to their suitability for Photoacoustic Tomography (PAT) and higher bandwidth compared to speckle analysis techniques. However, several challenges must be addressed before this approach can become a viable solution for commercial PAI systems. Efficient probe beam collection is crucial, yet challenging, particularly for in vivo samples. Additionally, most LDV systems are constrained to one or a few detection points, necessitating lateral scanning. Scaling these systems, whether free-space or fiber-based, leads to increased bulk and cost. In the following chapter, we discuss the chip-based solution that could overcome some of these challenges.

2.5.1 Laser Doppler Vibrometry

Generally, LDV-based systems can be classified into homodyne and heterodyne configurations, each offering unique advantages. The main difference between homodyne and heterodyne approaches lies in the presence of an optical frequency

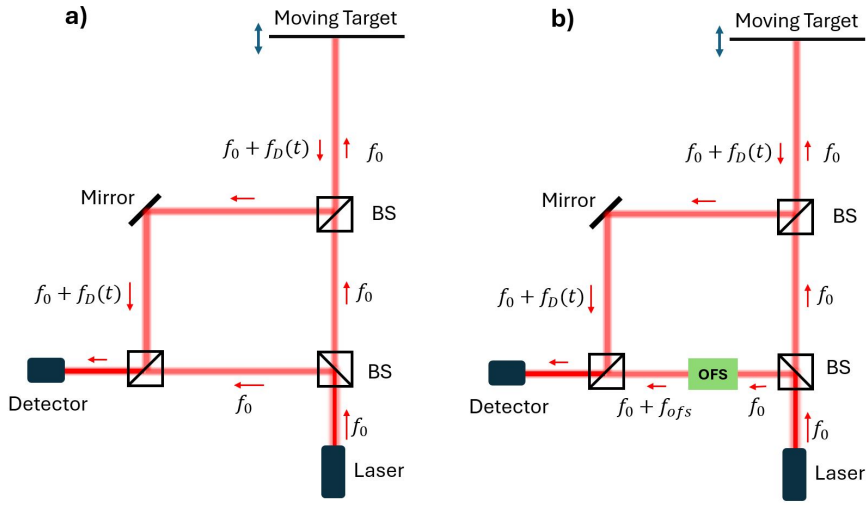

Figure 2.3: Schematic diagram of a) homodyne interferometer and b) Heterodyne interferometer. Reproduced from [43]. A beam splitter (BS) creates the reference- and measurement arm of the interferometer. The heterodyne interferometer has an optical frequency shifter (OFS) in the reference arm.

shifter in the heterodyne configuration. A schematic of a homodyne and heterodyne interferometer is indicated in Fig. 2.3. Both techniques split a coherent light source into a reference path and measurement path, which is directed towards a target. After reflection from the target, the measurement beam is combined with the local reference to interfere on the photodiode. When the sample is moving along the direction of the measurement beam with velocity $v(t)$, the reflected light is frequency-shifted with frequency $f_D(t)$ due to the Doppler effect.

$$f_D(t) = \frac{2v(t)}{\lambda} \tag{2.16}$$

Interference between the local oscillator and measurement beam causes a beating signal equal to the difference in frequency of both arms on the photodetector. In the case of homodyne LDV, this time-varying beating frequency is $f_D(t)$ while for heterodyne LDV this is frequency shifted in the electrical domain with frequency $f_D + f_{ofs}$. The absence of a frequency shifter makes the homodyne LDV an attractive design due to its simple optical setup. Nonetheless, most commercial LDVs operate on the heterodyne principle. In heterodyne systems, the electrical signal is shifted to a higher carrier frequency, reducing the impact of 1/f noise captured by the electronics. Moreover, heterodyne systems simplify detection requirements by using a single photodetector to measure the absolute movement

and direction of the sample.

Nonetheless, since the 1/f noise is only dominant for relatively low frequencies, the advantage in terms of noise is small for measuring in the ultrasound frequency band. Both homodyne and heterodyne LDVs have been used for the contactless detection of photoacoustic signals.

The frequency modulation with a varying frequency $f_D(t) \propto v(t)$ is equivalent to a phase modulation with phase change $\theta(t)$.

$$\theta(t) = 2\pi \int_0^t f_D(\tau) d\tau \tag{2.17}$$

A phase change $\Delta\theta(t)$ is related to the change in path length of the measurement beam and thus related to the displacement of the target.

$$\Delta d(t) = \frac{\Delta\theta(t)}{4\pi}\lambda \tag{2.18}$$

A displacement of half the wavelength will results in a 2π phase change. Typically, interferometry allows to discern much smaller phase changes such that detection of nm-displacments is possible. The next chapter will mathematically describe the working principle of a homodyne LDV.

2.5.2 Non-contact Photoacoustics using LDV

Laser Doppler vibrometry has long been used to detect ultrasound vibrations. In this section, we take a look at the latest advancements in using LDV systems for photoacoustic imaging.

Most of these demonstrations use a single beam and fiber-based LDV which is scanned along the surface of the sample. In 2013, Hochreiner et al. [8] demonstrated contactless imaging by scanning a fiber-based homodyne LDV over a photoacoustically excited chicken thigh to image embedded absorbers. In 2015, a paper from the same group showcased a similar demonstration but in a multimodal imaging system enabling OCT and photoacoustic imaging [13]. In these demonstrations, the LDV was directed to bare chicken skin.

In 2015, Eom et al. [11] showcased a heterodyne fiber-based noncontact PA tomography system capable of 3D imaging of blood vasculature in a chicken chorioallantoic membrane, enhancing reflection with a smoothing material. Similarly, a homodyne LDV was used to successfully image vasculature in a mouse ear, on which a water layer was applied to improve reflection [12].

While these demonstrations highlight the potential of photoacoustic detection using fiber-based LDV systems, they do not address several challenges impeding the widespread adoption of LDV for contactless photoacoustic imaging. Most in-vivo applications require high refresh rates to minimize motion artifacts. Scanning the LDV beam, as done in the discussed demonstrations, results in prolonged measurement times. Scaling a fiber-based system to hundreds of detection points would lead to prohibitively expensive and bulky optical systems due to the required discrete optical components. To address these challenges, this work focuses on developing a silicon photonics-based LDV demonstration, which could enable miniature, multipoint contactless photoacoustic imaging

3

Silicon Photonics-based Laser Doppler Vibrometer

3.1 Introduction

While previous work has demonstrated the working principle of silicon photonics-based homodyne LDVs, these systems have been limited to measuring vibrations up to 100 kHz. In this work, we use silicon photonics-based homodyne LDV specifically for ultrasound detection. Although similar photonic circuits are utilized, the main difference to previous work lies in the electronic amplification circuit, which needs to accommodate a carefully chosen bandwidth in the ultrasound range. Apart from describing the implementation, this chapter also focuses on the estimation and characterization of detection limits, which will aid in making crucial system design decisions such as determining the optimal bandwidth.

Section 3.2 reviews the working principles of silicon photonics-based LDVs as proposed in previous work. Fig. 3.1 illustrates a system with the various components which will be adressed throughout this section. We shortly discuss how the photodiode signals from the chip are amplified on a Printed Circuit Board (PCB) and how these signals are converted into an In-phase (I) and Quadrature (Q) signal, from which the displacement of the target can be demodulated.

Section 3.3 explains how noise sources limit the detection capabilities of the system and how shot noise establishes a theoretical detection limit. This analysis is specifically tailored to the development of an LDV system for photoacoustic and ultrasound measurements.

The displacement of the target can be demodulated from the I and Q signals, however, due to imperfections of the LDV system, an advanced demodulation method is often required. Section 3.4 describes the origin of imperfections and explains the Heydemann demodulation methods, used in this work to obtain accurate displacement information.

With the background of this demodulation algorithm, the characterization method and results of the silicon photonics-based LDV system developed in this work are presented in Section 3.5. Demonstrating detection limits on par with commercial LDVs and a bandwidth in the ultrasound range.

From the analysis of the theoretical detection limit and the implementation of the LDV system, it is evident that large optical losses, primarily due to coupling to and from the target, limit the signal-to-noise ratio. In search of an improved detection limit, Section 3.6 theoretically examines whether the implementation of

an Semiconductor Optical Amplifier (SOA) can enhance the performance of the on-chip LDV. Finally, we briefly discuss multi-point LDVs in the last section.

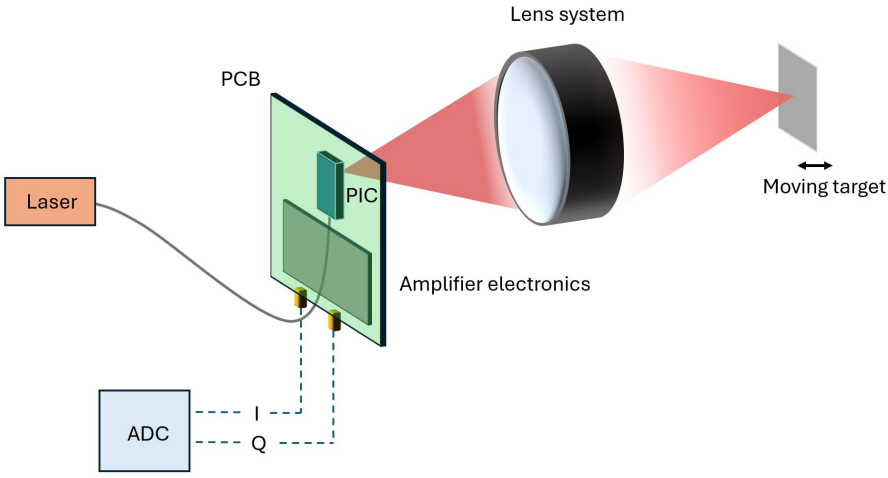

Figure 3.1: Schematic of a silicon-photonics-based homodyne LDV system. Light from a laser is coupled into a PIC. A portion of the light is directed from the PIC towards a moving target using a lens system. The reflected light from the target is then coupled back into the PIC. After undergoing optical processing, on-chip photodetectors generate different electrical signals, which are electronically amplified on a PCB. This results in two signals (I and Q) that are digitized by the ADC. These signals describe the movement of the target.

3.2 Homodyne on-chip Laser Doppler Vibrometer

3.2.1 Working principle

The layout of the silicon photonics-based implementation of a homodyne LDV is depicted in Fig. 3.2. A coherent light source is coupled into the chip via an optical fiber attached to the input grating coupler. Hereafter the light is split into a measurement arm and a reference arm on the photonic chip. In Fig. 3.2, the splitting of the light is achieved using a 1×2-Multimode Interferometer (MMI), which evenly divides the power between the two arms. To enhance the performance of the LDV, a tunable splitter can be employed to enable adjustable power distribution between the two arms. A tunable splitter can be realized using an Mach-Zehnder Interferometer (MZI) layout, with at least one arm containing a phase modulator [44].

After splitting, the measurement light is guided towards the Transmitter (TX)

grating coupler, which couples the light out of the chip. This light is typically directed towards a target using a lens system to focus it accurately. The reflected light from the target is then coupled back into the Receiver (RX)-grating coupler, which can be the same as the TX grating coupler (as is the case for Fig. 3.2).

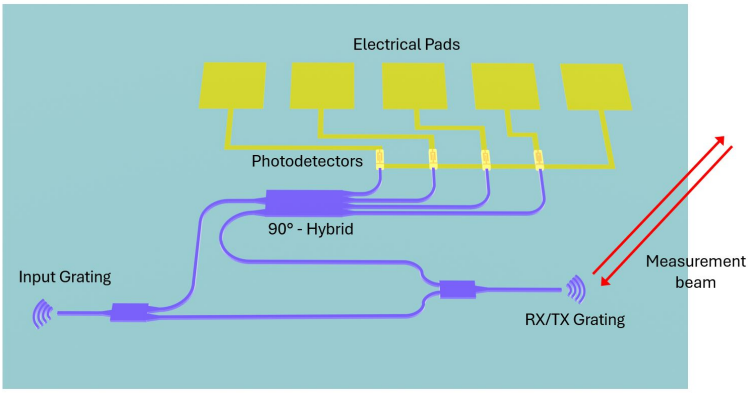

Figure 3.2: Layout of an on-chip homodyne LDV. Light is coupled into the chip using the input grating coupler, then split into a measurement and reference arm. The measurement light is coupled in and out of the chip using the TX/RX Grating couplers. The hybrid component combines the light in four different ways, and photodetectors convert these combinations into different currents, from which the displacement can be demodulated

The reflected light is then combined with the reference light in a 90-degree optical [45], which is connected to four photodiodes. The measurement and reflected light can be expressed using complex phasors as follows:

$$\mathbf{R}(t) = r\exp(i\theta_0) \tag{3.1}$$

$$\mathbf{M}(t) = m\exp[i(\theta_1 + \theta(t))]. \tag{3.2}$$

In the equations above, $\mathbf{R}$ and $\mathbf{M}$ are the phasors from the reference beam and measurement beam, respectively. The optical amplitudes of both arms arriving at the hybrid are represented as r and m, while θ_0 and θ_1 represent the static phase of the reference and measurement arms, respectively. The term $\theta(t)$ represents the dynamic phase due to changes in the path length of the measurement arm.

The optical hybrid has four output ports where the reference light and the measurement light are combined with different relative phases. These can be represented as follows:

$$\frac{1}{2}[\mathbf{M}(t) + \mathbf{R}(t)],\ \frac{1}{2}[\mathbf{M}(t) - \mathbf{R}(t)],\ \frac{1}{2}[\mathbf{M}(t) + i\mathbf{R}(t)],\ \frac{1}{2}[\mathbf{M}(t) - i\mathbf{R}(t)] \tag{3.3}$$

As illustrated in the equations above, the 90-degree optical hybrid combines the measurement and reference light in four outputs, each with a 90-degree shift in the relative phase difference between the measurement and reference light.

The 90-degree optical hybrid is realized using a 2×4-MMI. The working principle of MMIs is based on the self-imaging principle [46], where an input field excites multiple guided modes in the multimode region, each with a different propagation constant. These modes interfere along the length of the MMI. Due to the relationship between the propagation constants, replicas of the input excitation are imaged at specific positions. By appropriately placing the output waveguides at these positions, the light can be coupled into the four different outputs with the correct phase relations, as described by self-imaging theory. The desired relative phase differences are described by expression 3.3. The optical hybrids for 1550 nm and 1310 nm were based on the design by Halir et al. [45], and fine-tuned during simulations. The platform layer stack and a schematic of the design of the hybrid is depicted in Fig. 3.3a,b. The MMI was simulated using eigenmode expansion in Lumerical. The simulated amplitude of the electric field is shown in Fig. 3.3c.

Photodetectors with efficiency μ at the end of each port convert the intensity of the light into electrical currents. By substituting $\theta'(t) = \theta(t) + \theta_1 - \theta_0$, these currents can be expressed as follows:

$$i_1(t) = \mu\frac{|r|^2 + |m|^2}{4} + \mu\frac{|rm|}{2}cos(\theta'(t)) \tag{3.4}$$

$$i_2(t) = \mu\frac{|r|^2 + |m|^2}{4} - \mu\frac{|rm|}{2}cos(\theta'(t)) \tag{3.5}$$

$$i_3(t) = \mu\frac{|r|^2 + |m|^2}{4} + \mu\frac{|rm|}{2}sin(\theta'(t)) \tag{3.6}$$

$$i_4(t) = \mu\frac{|r|^2 + |m|^2}{4} - \mu\frac{|rm|}{2}sin(\theta'(t)) \tag{3.7}$$

The currents from these photodetectors can be combined into pairs (Eq. 3.8 and Eq. 3.9), resulting in two signals that represent points on an IQ-circle, as shown in Fig. 3.3d.

$$I(t) = i_1(t) - i_2(t) = \mu|rm|cos(\theta'(t)) \tag{3.8}$$

$$Q(t) = i_3(t) - i_4(t) = \mu|rm|sin(\theta'(t)) \tag{3.9}$$

By demodulation, we can retrieve the phase information of the reflected beam. In all system designs in this work, demodulation was performed after amplification and digitization of the I- and Q-signals. Ideally, we can demodulate the phase using:

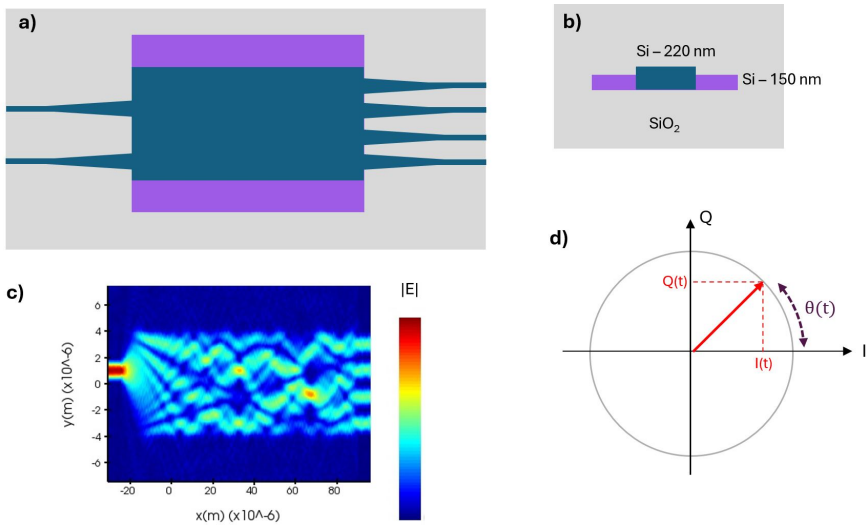

Figure 3.3: a) Design of a 2x4 MMI, acting as a 90 °- hybrid, developed on the SOI platform with the stack shown in b). c) The magnitude of the simulated E-field inside a 1550 nm optical hybrid for one excitation input. d) The output photodiodes provide the I(t) and Q(t) signals, which ideally form a circle, allowing the phase $\theta(t)$ to be demodulated.

$$\theta'(t) = \arctan(\frac{Q(t)}{I(t)}) \tag{3.10}$$

In reality, however, the I and Q circles typically form an ellipse rather than a perfect circle, often with a DC offset from the origin. This makes the simple demodulation method as expressed in Eq. 3.10 inaccurate. These imperfections are described in more detail in a subsequent section (Section 3.4), along with demodulation strategies to accurately demodulate the phase.

As mentioned in the previous chapter, the phase change can be used to demodulate the displacement of the target as follows [1]:

$$\Delta d(t) = \frac{\Delta\theta(t)}{4\pi}\lambda \tag{3.11}$$

[1]While this linear relation is generally true for a beam with a parallel phase front, a Guassian beam exhibits a deviation from the linear phase-displacement relation. This effect is called the Gouy phase shift. The deviation remains limited for low NA systems ($< 1\%$ deviation for NA < 0.14) and is thus neglected in the remainder of this thesis.

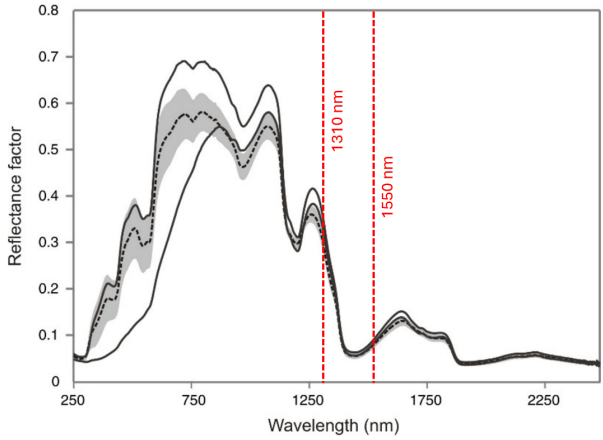

Figure 3.4: Skin reflectance spectra for different skin types, figure adapted from [48]

3.2.2 Optical light source- LDV

The light source of the on-chip LDV is a crucial component determining the overall performance of the device.

Firstly, the wavelength of this source will significantly impact the amount of light reflected from the skin. As illustrated in Fig. 3.4, visible wavelengths exhibit the highest reflectance. One might assume that these wavelengths would be optimal for an LDV measuring on skin. However, safety limits for infrared wavelengths are about ten times less stringent than for visible wavelengths. Additionally, infrared wavelengths, such as those in the C-band and O-band, are widely adopted in the telecommunications and datacom industries, making them prevalent and well-suited for silicon photonics on the SOI-platform. Note that while the SOI platform is not suitable for accommodating visible wavelengths, other platforms, such as Silicon Nitride, may be used for applications requiring visible light.

In this PhD research, we utilized a commercial SOI platform, specifically the ISIPP50G-platform from imec, due to its high-performing photodetectors [47]. Silicon's transparency window spans from approximately 1.1 µm to several micrometers, making it suitable for infrared wavelengths. For the C and O-band, optimized Process Design Kit (PDK) components and on-chip photodetectors are readily available for most SOI platforms, thus making these wavelengths advantageous. The C-band, centered around 1550 nm, is the most common band but has limited reflectance from the skin. The O-band, around 1310 nm, is preferred as it shows a threefold increase in reflectance and offers a skin safety limit relaxed by a factor of two compared to 1550 nm [48].

Due to the coherent nature of interferometric techniques, it is essential that the light source for LDV is coherent. The coherence length of the laser light should be much greater than the path length difference between the measurement and reference arms. In this PhD research, we used an external fiber-coupled distributed feedback laser to deliver light to the chip through an input grating coupler, as depicted in Fig. 3.2. Further miniaturization of the LDV system is possible by co-packaging the laser and isolator using a micro-optical bench, as demonstrated in previous studies [14]. Lasers and isolators present functionalities that go beyond passive optics, requiring materials beyond the SOI platform such as III-V semiconductors and magneto-optical materials. Heterogeneous integration techniques (e.g. micro-transfer-printing [49]) have also shown potential for integrating lasers onto the silicon photonics platform, offering an effective method for further system miniaturization. However, at the time of writing, an SOI platform offering integrated lasers and isolator is not commercially available.

3.2.3 Optical Losses and Collection efficiency

Loss in the optical path will determine the amplitude of the IQ circle, which is a critical parameter in the performance of the LDV. As we will discuss in detail in Section 3.3, maximizing the IQ -radius by minimizing these losses is crucial for optimizing the overall performance of the system.

Considering typical optical propagation lengths of around a few mm in the SOI chip for LDV circuits and accounting for typical waveguide losses of 1-2 dB/cm, it is evident that on-chip propagation losses are relatively minor. The majority of losses arise from the coupling processes, particularly the coupling of laser light out of the chip, the coupling to and from the target, and the coupling back into the chip along the measurement path. Below, we provide an overview of these loss contributions.

Each coupling via a grating coupler incurs an estimated loss ranging from 2.5 to 3 dB. Additionally, in the absence of an on-chip circulator, reciprocity introduces a cumulative loss of 6 dB. This loss arises from the three-port system: one port connected to the laser input side, one port connected to the TX/RX grating coupler, and the waveguide leading to the optical hybrid, as illustrated in Fig. 3.5.

Furthermore, the collection efficiency—encompassing losses from limited reflectance and the performance of the optical system—significantly affects overall system performance. The lens system must effectively focus light exiting from the grating coupler onto the target and back. The efficiency of this process depends on the target's reflectance and angular reflection profile, which influences how much light is redirected back into the lens system and subsequently focused into the grating coupler. For a skin target, the reflectance profile is illustrated in Fig. 3.4.

Evaluating the efficiency of the lens system itself is more complex and requires careful consideration.

First, it's important to note that the lens system can introduce aberrations, reflections and phase front distortions, which contribute to overall optical loss. If we assume these imperfections are minimal, the remaining source of loss would then be due to the limited numerical aperture (NA) of the optics. To estimate this loss, we can consider two contrasting scenarios for the angular reflectance profile of the target: (1) a specular reflector, which reflects light in a single, well-defined direction, and (2) a Lambertian reflector, which exhibits uniform radiance across all directions. Note that skin is a highly diffuse reflector and therefore more similar to the Lambertian reflection profile [50].

Fig. 3.5 illustrates a simple imaging system using a single lens to focus light onto the target. Assume we use a lens system, where the Numerical Aperture (NA) of the lens on the grating coupler side matches or is bigger than the NA of the grating coupler, such that most of the light exiting from the grating coupler is focused onto the target. For a single lens system as indicated in Fig. 3.5, this means that the aperture a is big enough to capture the light from the chip at distance o with divergence angle θ_0 and thus $a > o\sin(\theta_0)$.

In the case of specular reflection, the efficiency will be similar to the reflectance R. Due to reciprocity and symmetry, for perfect alignment, all of the reflected light is captured back into the imaging system and focused in the PIC when neglecting any reflection losses. In the case of a Lambertian reflector, we need to account that some of the light is reflected in directions that cannot be captured by the optical system and coupled back to the grating coupler. We can only consider the light reflected back into the cone characterized by angle θ_1 as indicated in Fig. 3.5, which is the same as the focusing angle originating from the light from the grating coupler. For a Lambertian reflector, the captured power fraction can be calculated as $sin^2(\theta_1)$. Since we can write $NA_1 = nsin(\theta_1)$ the captured power will scale with NA_1^2. It is important to note that increasing the NA_1 results in a decrease in the depth of focus, making alignment more challenging.

To give an idea about the magnitude of these losses, Table 3.1 shows an overview of the expected losses throughout the measurement path. Adding them shows estimated total losses between 27 -32 dB, highlighting that significant losses occur in the measurement arm of the LDV.

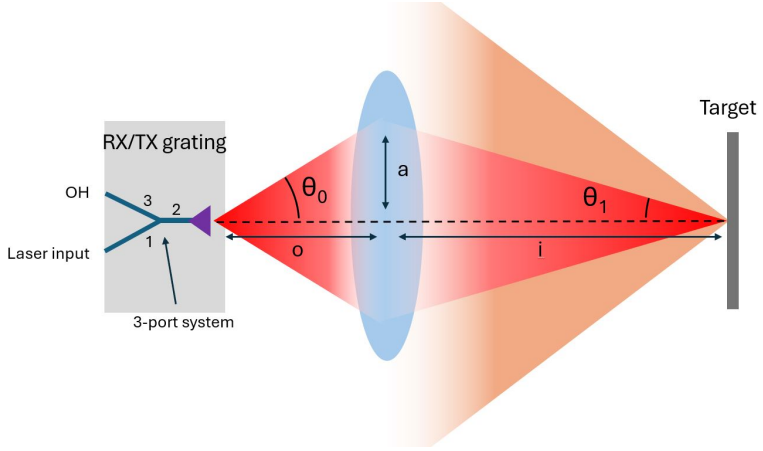

Figure 3.5: Shematic of the three-port system and the imaging system in the measurement path to couple and focus light coming from the grating coupler onto the target and collecting the back-reflected light back into the PIC.

	Loss
3-port system: $1 \rightarrow 2$	3 dB
Grating coupler	2.5 - 3 dB
Reflectance	1550 nm: $\pm$ 10 dB 1310 nm: $\pm$ 6 dB
Imaging system NA=0.3	$\pm$ 10 dB
Grating coupler	2.5 - 3 dB
3-port system: $2 \rightarrow 3$	3 dB
Total	1550 nm: **31 - 32 dB** 1310 nm: **27 - 28 dB**

Table 3.1: Overview of estimated losses in the measurement path for an imaging system with an NA=0.3 and neglecting aberration losses and phase front distortion effects.

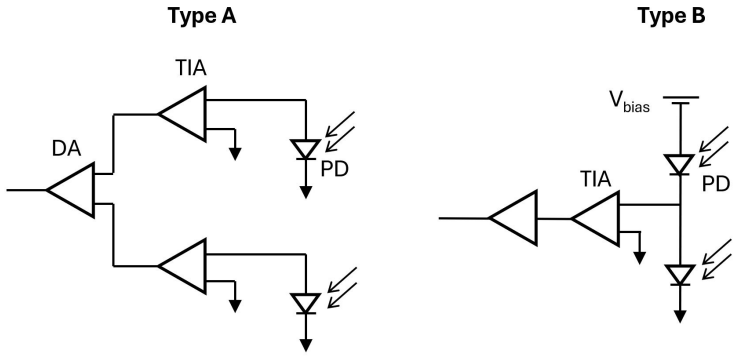

Figure 3.6: a) Balanced detection realized with a PD pair using a trans-impedance amplifier (TIA) for each PD, followed by a differential amplification stage (DA) b) balanced detection of PD pair in series, using one TIA stage and optional more opamp stages to amplify the signal more.

3.2.4 Amplifier Electronics

The photodiodes connected to the hybrid convert the optical intensity in each arm into four currents. Wirebonds connect the photodiodes to a PCB that amplifies the photocurrents and produces output voltage signals I and Q. There are two schemes for amplifying the photodiode signals, as indicated in Fig. 3.6.

With amplification as described by type A, the four photocurrents are first converted into voltage signals using trans-impedance amplifiers for each current. In the second stage, differential amplification is used to perform the subtraction operation from equations 3.8 and 3.9.

For type B, pairs of photodiodes are connected such that the difference in current between them is sent to a trans-impedance amplifier, which converts the current into a voltage signal. This signal can then be further amplified using operational amplifier (opamp) stages.

It is important to note that in type B, we cannot compensate for differences between the pairs of photodetectors, whereas in type A, we can use a tunable first stage to compensate for these differences. However, type A requires a more complex schematic. While the type B only amplifies differential signals between the two photodiodes, type A first amplifies the total photocurrent including the large but unimportant DC component from Eqs. 3.4-3.7 in the first stage and only takes the differential in the second stage. Choosing between the two methods involves weighing the more flexible but complex electronic amplification against the simpler but less flexible method of type B.

When designing for ultimate performance, the final voltage signal should match the range of the digitizer. Therefore, it is important to estimate the magnitude of the AC photocurrent signal, which depends on the power in the reference arm and the captured power of the reflected signal. The design and amplification for ultimate performance are largely dependent on the expected powers in the measurement- and reference arm and the desired detection bandwidth. The design of these amplification circuits is well described in literature [51]. Since the photocurrents can be considered as phase modulated signals with a phase modulation frequency equal to targets vibration frequency, the electronic bandwidth should be generally larger than the desired vibration detection bandwidth for large vibrations. However, since we target measuring photoacoustic vibrations which are very small, the electronic bandwidth is almost equal to the desired vibration bandwidth. For our purposes, we aim for a bandwidth of 3-5 MHz, which should be sufficient to measure small vibrations up to these frequencies.

3.3 Noise and Detection limit of LDV

In this section, we discuss several noise sources, estimate the ultimate performance of the LDV, and compare this against the performance of contact-based sensors.

3.3.1 Noise

Shot noise is a fundamental noise source in the measurement of an electric field, originating from quantum fluctuations [52]. Unlike other types of noise, shot noise is intrinsic to the quantum nature of charge carriers and photons that are discretely detected as individual events. This discrete nature gives rise to fluctuations that are not due to external influences but rather the probabilistic nature of quantum processes.

In this context, shot noise can be understood through Poisson statistics, which describe the probability of a given number of events occurring in a fixed interval of time when these events are independent and randomly distributed. The variance in the number of detected events (e.g., photons or electrons) over time is directly proportional to the mean count rate, leading to characteristic fluctuations that scale with the square root of the signal.

Shot noise is a type of white noise due to its flat spectral power density over a wide frequency range. This flatness arises because the events generating shot noise are uncorrelated, leading to a uniform contribution across frequencies.

The theoretical white noise spectral density measured by a photodetector can be described as:

$$i_n = \sqrt{2q\mu P}\,[\frac{\mathrm{A}}{\sqrt{\mathrm{Hz}}}] \tag{3.12}$$

Another fundamental noise source is thermal noise, caused by the feedback resistance in the amplifier circuit. This noise, also called Johnson-Nyquist noise, originates from the thermal movement of charge carriers causing small electrical fluctuations. Its noise spectrum is generally flat, making it another white noise source. Note that this is not expressed in the same units as shot noise, and in the next part, we will convert all of them to the same metric. The voltage across a resistor with resistance R_f has a noise spectral density given by:

$$v_{thermal} = \sqrt{4k_bTR_f}\,[\frac{\mathrm{V}}{\sqrt{\mathrm{Hz}}}] \tag{3.13}$$

In addition to these fundamental noise sources, the non-ideality of the op-amps causes several noise contributions [51]. Here, we will not discuss these in detail, but generally, you can consider contributions due to input-referred voltage noise, input-referred current noise, and input capacitance.

Intensity variations of the laser, also known as Relative intensity Noise (RIN) is mostly compensated by the balanced detection method and therefore its contribution can be neglected. On the other hand, phase variations of the laser, characterized by the linewidth and coherence length of the laser, do add noise to the demodulated phase. Still, it can be mitigated by choosing a laser with a large coherence length. Another common source in interferometric techniques is speckle noise, generally it originates from lateral movements compared to the measurement beam. While this may occur when working with in-vivo samples, here, we assume the movements are small and slow enough compared to the time length of the photoacoustic measurements.

Other sources of noise can occur due to various non-idealities in the system, such as spurious reflections in the optical path, or electromagnetic interference in the electronics of the system. However, in the remainder of this section, we consider an ideal system and calculate the fundamental shot noise limit.

To study the influence of the different noise sources, we must translate their impact in terms of the final phase/displacement noise. The current noise and voltage noise can be converted to the same units using the impedance of the amplifiers. Assuming a linear and constant impedance over the system's bandwidth region, this becomes just a scaling factor, similar to the amplification of the signal.

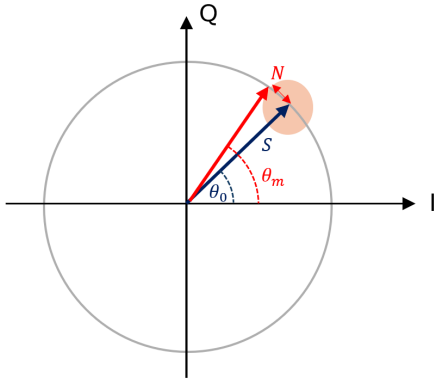

Figure 3.7: The IQ circle whereby a white noise source on the I and Q signal with magnitude N results in an uncertainty on the measured phase. The measured phase θ_m is different from the actual phase θ_0.

When converted to either current or voltage noise, the signal S must be considered in the same units. White noise sources on the I and Q circle cause an uncertainty in the demodulated phase. Fig. 3.7 shows how noise N results in a measured noise θ_m which is different than the actual phase θ_0.

From Fig. 3.7, it can be seen that the phase noise contribution can be estimated as the $\theta_n = \arctan(N/S)$, with N the noise amplitude and S the signal amplitude.

3.3.2 Theoretical detection limits

Considering a shot noise-limited situation, the optimal performance of an LDV can be estimated. Let P_m and P_r be the power in the measurement and reference beam arriving at the optical hybrid. Assume now that we can estimate these powers according to:

$$P_m = \alpha s P_{in} \tag{3.14}$$

$$P_r = (1 - s) P_{in} \tag{3.15}$$

In this equation, P_{in} represents the on-chip power before splitting into the reference and measurement beam for a single LDV. The tunable splitter in the on-chip LDV then distributes the light in fraction s going to the measurement beam and fraction $1 - s$ going to the reference path. α represents the loss in the measurement path, mostly due to coupling light towards the target and back and the loss from the TX/RX grating couplers. As can be seen from these equations, we do not consider on-chip losses, since they remain limited, especially compared to excess losses in the measurement path.

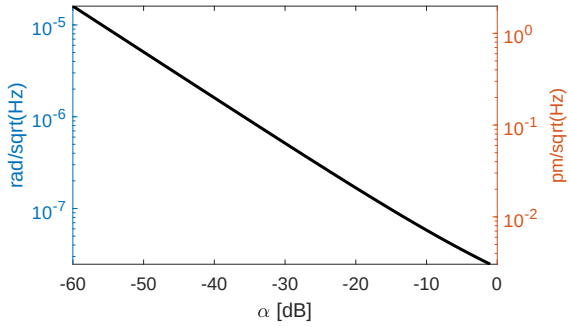

Figure 3.8: Shot noise limited performance estimate of an LDV depending on the loss in the measurement path α, and the power in the measurement beam after the splitter is 10 mW

The signal magnitude is now:

$$I_s = \mu\sqrt{P_m P_r} = \mu\sqrt{\alpha s(1-s)}P_{in} \tag{3.16}$$

While the shot noise contribution is:

$$I_n = \sqrt{4q\mu(P_m + P_r)} = \sqrt{4q\mu((\alpha-1)s+1)P_{in}} \tag{3.17}$$

For optimal phase noise in a shot noise limited situation, I_n/I_s is minimal, and thus we can find an optimal splitting ratio (s:1-s) for $s = \frac{\sqrt{\alpha}-1}{\alpha-1}$. While this splitting ratio is optimized for a situation only considering shot noise, it may not be optimal considering other noise sources.

Although increasing P_{in} could be a good approach to further minimize I_n/I_s and thus the phase noise originating from the shot noise, practical considerations limit the optical power used. First of all respecting eye-safety limit for 1550 nm limits beam power to 10 mW. Secondly, powers much higher than 10 mW would induce nonlinear losses in the silicon due to two-photon absorption. Therefore, we consider the power of the measurement beam before coupling to the target as $sP_{in} = 10\ \mathrm{mW}$. Now, we can plot the estimated phase noise (due to the shot noise contribution) as a function of α in Fig. 3.8. Since the demodulated phase is directly related to the measured displacement as stated in Eq. 3.11, the noise can also be expressed as displacement noise.

Assuming white noise sources, the total noise can be estimated by integrating over the system's bandwidth, resulting in:

$$\theta_{noise,total} = \theta_n\sqrt{BW} \tag{3.18}$$

$$d_{noise,total} = d_n\sqrt{BW} \tag{3.19}$$

However, these noise figures do not permit direct comparison with typical ultrasound sensors noise figures, which are generally characterized in terms of pressure noise. To relate the pressure noise to the displacement noise, first consider the specific acoustic impedance Z, which relates pressure to the medium's velocity. For the velocity of the boundary, where we assume a large impedance difference between the sample and air, we can write:

$$p = \frac{Z}{2}v \tag{3.20}$$

This relation can be easily deduced from the plane wave equations and boundary conditions as shown in Appendix A.

First, the measured displacement of the surface can be related to a measured velocity and similarly the noise figures can be converted. Consider an acoustical wave with wave number k causing a displacement $d(x,t)$ with angular frequency ω and amplitude d_m.

$$d(x,t) = d_m \sin(kx - \omega t) \tag{3.21}$$

Now the velocity can be estimated by taking the temporal derivative:

$$v(x,t) = -\omega d_m cos(kx - \omega t) \tag{3.22}$$

The amplitude of a vibration with frequency f is related to the velocity amplitude of the same vibration and using Eq. 3.20, the relation to the pressure amplitude of this wave can also be estimated:

$$v_m = d_m 2\pi f \tag{3.23}$$

$$p_m = \frac{Z}{2}2\pi d_m f \tag{3.24}$$

Due to the frequency dependence in the velocity noise relation, the velocity noise spectrum does not behave as a white noise source (contrary to the displacement and phase noise spectrum).

Let us consider the situation where the displacement noise is equal to $0.1\mathrm{pm}/\sqrt{(}\mathrm{Hz})$, which is the expected shot noise for a loss of around -30 dB and -40 dB in the measurement arm, close to the loss values estimated in section 3.2.3. Moreover this noise floor is similar to the characterized noise floor of the silicon photonics-based LDV in our demonstration as we show in Section 3.5.

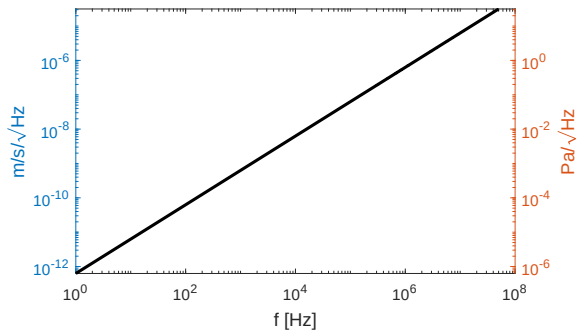

Figure 3.9: Estimated velocity and pressure noise spectrum for an homodyne LDV using a specific acoustic impedance of 1.5 MRayl when the displacement noise limit is flat and equal to $0.1\ pm/\sqrt{Hz}$

Using equations 3.23 and 3.24, the resulting velocity and pressure noise spectrum can be calculated, as shown in Fig. 3.9. Note that the system's bandwidth has not been considered yet.

The total velocity and pressure noise over a bandwidth ranging from 0 to BW can be estimated as:

$$v_{noise,total} = \sqrt{\int_0^{BW} (2\pi d_{Noise} f)^2 \, df} = 2\pi d_{Noise} \sqrt{\frac{BW^3}{3}} \tag{3.25}$$

$$p_{noise,total} = \sqrt{\int_0^{BW} (Z2\pi d_{Noise} f)^2 \, df} = Z2\pi d_{Noise} \sqrt{\frac{BW^3}{3}} \tag{3.26}$$

It can be observed that the noise floor, in terms of both pressure and velocity, increases rapidly with increasing bandwidth. Therefore, it is crucial to balance the system's bandwidth: limiting it to reduce noise while ensuring it is large enough to capture the desired photoacoustic signals.

3.3.3 Comparison to a contact-based ultrasound sensor

With the noise level for a chip-based homodyne LDV, we can now compare its performance to that of a high-performing contact-based sensor. Here, we consider a recently developed silicon photonics-based Optomechanical Ultrasound Sensor (OMUS) [53], presenting a large bandwidth and high sensitivity. Based on its characteristics, the noise level is estimated to be around $1\ \mathrm{mPa}/\sqrt{(\mathrm{Hz})}$ over a bandwidth of tens of MHz when in contact with the sample. For the LDV, we

consider a displacement noise floor of $0.1\ \mathrm{pm}/\sqrt{(\mathrm{Hz})}$, as this is close to the characterized noise floor as we will see in one of the following sections. As mentioned before and through Eqs. 3.23 and 3.24, this noise floor can be expressed in terms of velocity and pressure, and the result is plotted in Fig. 3.10. When comparing the LDV noise floor (in black) against the contact-based OMUS (red), it is clear that the noise floor at ultrasound frequencies (around MHz and above) is about 2-4 orders of magnitude higher for the LDV compared to the contact-based method. However, for contactless detection, we need to account for the pressure drop due to the impedance mismatch between air and tissue, and the propagation loss of ultrasounds through air.

According to the theory of plane pressure waves, the transmission coefficient T, is equal to the ratio of the amplitudes of the transmitted and the incident (A_t and A_i) plane waves. For a plane wave transitioning from medium 1 with specific acoustic impedance Z_1 to medium 2 with impedance Z_2 (see Appendix A), the transmission coefficient T can be described as:

$$T = \frac{A_t}{A_i} = \frac{2Z_2}{Z_1 + Z_2} \tag{3.27}$$

Considering an impedance of 1.5 MRayl for tissue and 414 Rayl for the impedance of air, the resulting pressure drop is a factor of $T = 6 \cdot 10^{-4}$, resulting in the yellow line in Fig. 3.10. Once we also take into account the propagation losses of ultrasound in atmospheric conditions according to the equations published by Bass et al. [54], resulting in the purple line in Fig.3.10, it becomes clear that it is not possible to use the OMUS for contactless detection of ultrasounds. Here, we assumed a 1 cm propagation length in air, but from the dramatic increase in loss it is clear that even much smaller air gaps can be detrimental.

While the OMUS in contact shows a much better noise spectrum compared to the LDV for measuring ultrasounds, for non-contact operation it is evident that due to the combination of impedance mismatch between tissue and air and the propagation loss of ultrasounds, the LDV shows a better noise floor. For contactless detection, the LDV is thus the better option, but we do have to consider that the noise floor in the MHz region is several orders of magnitude larger for the LDV compared to the contact-based ultrasound sensor.

Therefore, it is physically impossible to attain similar photoacoustic imaging characteristics with a contactless, LDV-based method compared to a contact-based photoacoustic imaging systen. This means that contactless photoacoustic imaging will come at the cost of either resolution (by limiting the detection bandwidth) and/or imaging depth (due to the higher noise floor).

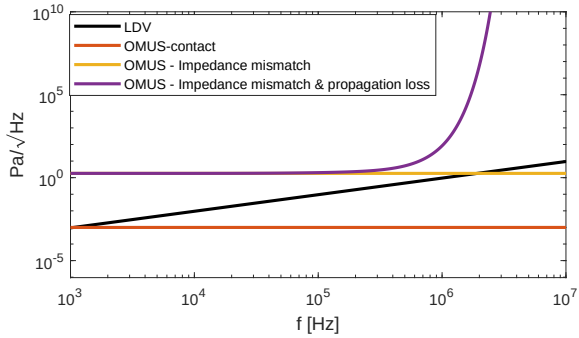

Figure 3.10: Comparison of the pressure noise spectra of an LDV with a displacement noise floor of 0.1 $pm/\sqrt{Hz}$ against the OMUS, with an estimated noise floor around 1 $mPa/\sqrt{Hz}$. Different lines consider different situations for the OMUS such as; (red) in contact with the sample, for air-coupled detection which comes the impedance loss due to the tissue-air interface (yellow) and with ultrasound propagation losses (purple). The ultrasound propagation distance in air was assumed to be 1 cm

3.4 Imperfections and demodulation

System imperfections influence the I and Q signal integrity, rendering simple arctangent demodulation inadequate for obtaining accurate results. In this section, we discuss the origins of these nonlinearities and explain the Heydemann method, used in this thesis, which numerically adjusts the demodulation method. We also discuss two other methods that can compensate for errors post-demodulation.

3.4.1 Non-linearities

A significant source of nonlinearities arises from imbalances in the detection system. This imbalance can result from various factors, such as imbalances in the optical hybrid, differences in photodiode conversion efficiencies, and variations in electronic amplification values of each photodiode signal. These differences can be described with photodiode conversion efficiency values μ_1 and μ_2, leading to the following expressions:

$$\begin{aligned} I(t) &= i_1(t) - i_2(t) = (\mu_1 - \mu_2)P_{dc} + (\mu_1 + \mu_2)|E_r E_m| cos(\theta'(t)) \\ Q(t) &= i_3(t) - i_4(t) = (\mu_3 - \mu_4)P_{dc} + (\mu_3 + \mu_4)|E_r E_m| sin(\theta'(t)) \end{aligned} \tag{3.28}$$

As seen, the imbalance results in the center of the circle shifting to $((\mu_1 -$

$\mu_2)P_{dc}, (\mu_3 - \mu_4)P_{dc})$ and distorting the circle into an ellipse along the I and Q axes.

Another type of error is phase errors, induced by imperfections in the hybrid originating from fabrication errors or temperature changes. Considering a phase error θ_r between the two input ports contributing to the I-signal, we have:

$$\begin{aligned} I(t) &= |E_r E_m|(cos(\theta'(t) + \theta_r) + cos(\theta'(t))) \\ &= 2|E_r E_m|cos(\theta_r/2)cos(\theta'(t) + \theta_r/2) \end{aligned} \tag{3.29}$$

This results in a change in the signal amplitude and a phase delay in the I signal. Taking both phase errors and imbalance errors into account, we generally write the I and Q signals as:

$$I(t) = \alpha_I \cos\theta'(t) + I_{dc} \tag{3.30}$$

$$Q(t) = \alpha_Q \sin(\theta'(t) + \theta_s) + Q_{dc} \tag{3.31}$$

Here, α_I and α_Q are the final amplitude of both signals, I_{dc} and Q_{dc} are DC factors, and θ_s is the spurious phase delay between the I and Q signal induced by phase errors.

Now, the I and Q signal form a distorted Lissajous curve, creating an ellipse with its center at (I_{dc}, Q_{dc}), a rotation angle of $\arctan(\Delta \pm \sqrt{(}\Delta^2 + \sigma^2)/\sigma)$ and semi-major and minor axis of $(\alpha_I^2 + \Delta \pm \sqrt{\Delta^2 + \sigma^2})^{1/2}$, where $\Delta = \frac{\alpha_Q^2 - \alpha_I^2}{2}$ and $\sigma = \alpha_I \alpha_Q \sin(\theta_s)$ [55].

The distortions in the Lissajous curves result in errors in the demodulated phase/displacement. These distortions can be categorized into two types: 1st-order and 2nd-order periodic nonlinearities. First-order non-linearities are due to the DC-terms in the I and Q terms (Eqs. 3.30, 3.31). The second-order non-linearities arise from the elliptical shape of the curve and are due to θ_s, α_I and α_Q.

A schematic of these errors can be seen in Figure. 3.11. Considering $\theta_m(t)$ as the measured phase and $\theta_0(t)$ as the actual phase, the phase error can be described as $\theta_0 - \theta_m(t)$. For the 1st-order non-linearity, the measured phase is described as:

$$\theta_{m,1^{st}} = \arctan(\frac{\sin\theta_0 + Q_{dc}}{\cos\theta_0 + I_{dc}}) \tag{3.32}$$

The second-order non-linearity is described as:

$$\theta_{m,2^{nd}} = \arctan(r\tan(\theta_0 - \theta_d)) + \theta_d \tag{3.33}$$

Where r is the ratio of the semi-major axis and the semi-minor axis and where θ_d is the rotation angle. Now that we have described the IQ curve distortion, in the next section, we discuss how this is compensated for our measurements.

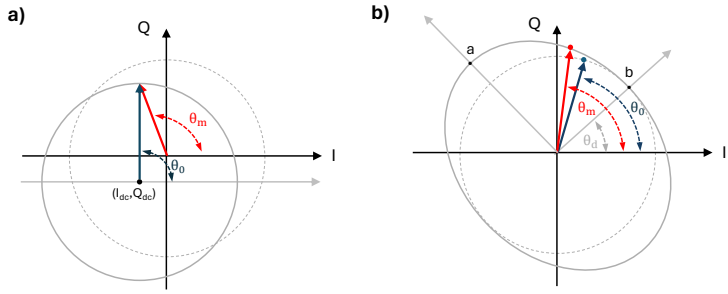

Figure 3.11: a) 1st order non-linearity due to DC errors and b) 2nd order non-linearity due to elliptical shape of the IQ curve.

3.4.2 Heydemann correction

The Heydemann correction is widely used for demodulation due to its accuracy and intuitiveness [56]. It relies on the assumption, that the IQ ellipse is stable, such that its parameters can be assumed to be constant. This method projects the measured IQ curve back to a circle and then performs arctan demodulation. This method is used in the following chapters of this work. To apply this method, an initial estimation of the full measured IQ ellipse is required. This can be done by measuring a vibration with an amplitude larger than half the wavelength or by sweeping the phase of the reference and measurement arms. Once data points are collected, an ellipse can be fitted to the measured points to yield the values for $(I_{dc}, Q_{dc}), \theta_d$, and the semi-major and -minor axis. Using this data, a simple transformation converts points on this curve back to the unit circle, allowing the arctan demodulation method to be used. It is important to note that this method requires access to the I and Q signals before demodulation and generally needs data from a large part of the IQ curve.

While other demodulation methods have been proposed that estimate compensation based on the arctan demodulated data [55], we have opted to use the Heydemann correction method in this thesis due to its proven performance and accuracy.

Since photoacoustic vibrations are typically small, in this work (as will be explained more in detail in Chapter 4), the ellipse parameters were recorded just prior to the photoacoustic measurements by first capturing and fitting data from a larger vibration.

3.5 Characterization and performance of the silicon photonics-based LDV

Noise

The theoretical noise limit, discussed in Section 3.3.2, provides a fundamental detection limit. Fig. 3.12 illustrates the noise limit detected by the on-chip LDV in the lab test. In this experiment, the LDV was directed at a flat, specularly reflective, silicone surface (similar to the phantom used for the photoacoustic measurements in Chapter 4). A 1 second recording was captured while no vibrations were actively induced on the surface. After demodulation (using the Heydemann method as described in 3.4), the phase/displacement was processed using the Welch method [57] to estimate the Noise Equivalent Displacement (NED) and Noise Equivalent Pressure (NEP) spectrum, with 2048 samples per segment, 512 overlapping, and linear detrending, resulting in Fig. 3.12a. In the MHz frequency range, the chip-based LDV presents an NED of around $0.1 - 0.2\ \mathrm{pm}/\sqrt{(\mathrm{Hz})}$. At lower frequencies, the noise floor seems higher, which can originate from the fact that the measurement detects background vibrations (which are more present at lower frequencies) or from 1/f - noise in electronics that elevate the noise floor at lower frequencies.

To measure this noise floor, the alignment between the sample and LDV was optimized to ensure optimal specular reflection. Subsequently, we increased the laser power input to the LDV, enlarging the IQ circle just below the clipping point, resulting in a chip-based optical output power of 0.5 mW for one output beam. Increasing the power beyond this point would lead to saturation in the electrical amplifiers and, consequently, clipping of the IQ circle. Using almost the full range of the electrical amplifiers minimizes the influence of electrical noise from the amplifiers or ADC noise.

The same resulting noise floor can also be expressed in terms of velocity noise and, using Eq. 3.20 in terms of pressure noise (Fig. 3.12b). Here, we assume an acoustic impedance of 1.5 MRayl, close to the acoustic impedance of water and biomedical tissue [58]. Fig. 3.12b also shows the results for measurements in the same setup, but using a commercial LDV (Polytec OFV-534, decoder VD-5000). The polytec demonstrates a velocity noise floor in the $\frac{\mu\mathrm{m}}{\mathrm{s}\sqrt{\mathrm{Hz}}}$ region (similar to the noise floor according to the data sheet: $3\frac{\mu\mathrm{m}}{\mathrm{s}\sqrt{\mathrm{Hz}}}$ at the center frequency). The on-chip LDV has a noise floor that is on par with, or even better than, the commercial LDV.

Note that multiple factors play into this difference. Outside of the different optics used within the LDV, the commercial LDV also works at a different wavelength (633 nm vs 1550 nm), a different working distance ($\pm$ 30 cm for the commercial

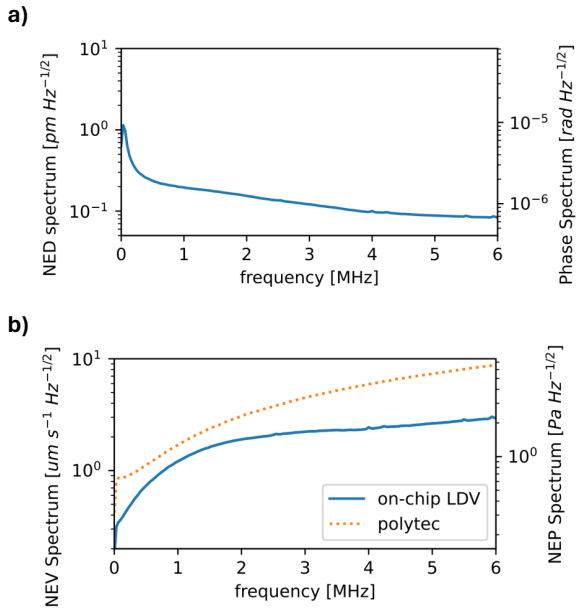

Figure 3.12: a) Noise equivalent displacement spectra for the chip-based LDV. b) Noise equivalent velocity spectra of the chip-based LDV and a commercial LDV (polytec).

LDV vs 7 cm for the chip-based LDV), and most importantly, different electronics.The on-chip LDV electronics are optimized for relatively strong reflections and developed for signals up to 3-5 MHz, compared to the 10 MHz bandwidth of the Polytec electronics. We've also carefully adjusted the optical power to match the on-chip LDV's optimal working range, which enhances its performance under these conditions. This combination of a lower bandwidth and optimized power adjustment could explain why the on-chip system presents a lower noise floor, despite the Polytec electronics being potentially better suited for measurements involving lower or variable reflections and sustaining a bandwidth of 10 MHz. Nonetheless, the results in Fig. 3.12b demonstrate the high performance of the chip-based LDVs.

The noise floor of the chip-based LDV could potentially be reduced further by increasing the LDV laser power up to the safety limit (10 mW @ 1550 nm) which would require designing the amplifier electronics accordingly.

To estimate how close this result is to the shot noise limit, we need to estimate the power of the measurement and reference beam after the hybrid.

The power of the measurement beam coupled out from the chip, was measured

to be 0.5 mW. Assuming the grating coupler performance is around 3 dB, and considering that TX and RX use separate grating couplers, we estimate that the power coupled into the measurement beam before coupling-out from the chip was around 1 mW. Assuming the splitter between the reference and measurement beam performs as designed, with a splitting ratio of 60/40, the power before the splitter can be estimated at 1.66 mW. Now, by estimation of the common loss of both the reference and measurement path and the excess loss of the measurement path we can calculate the expected shot noise.

The common loss, which encompasses all the on-chip losses that are similar for both paths, including transmission losses of the waveguides (approximately 7-8 mm), insertion losses from splitters, loss due to the limited efficiency of the photodetectors, and hybrid losses can be roughly estimated to fall between 2 dB and 4 dB.

Excess losses in the measurement path originate from 1) the grating coupler losses when coupling out from the chip, 2) losses of the optical system from focusing and collecting, 3) limited reflection and 4) the loss from coupling back into the chip via the grating coupler. Using the Fresnel equations, we estimate a loss of around 15.6 dB due to the LDV reflection from the air-Polydimethylsiloxane (PDMS) interface with reflectance R=0.027. Other losses inside the measurement path (see section 3.2.3); the TX grating coupler, the RX grating coupler, and the collection efficiency, are estimated to add a total of 5-20 dB, which results in total excess loss in the measurement arm between 20 and 35 dB .

Using these data, we can estimate the theoretical shot noise floor for different values of common loss and excess loss. We can also calculate the amplitude of the expected voltage of the signal using the electronic amplification factor ($= 340 \cdot 10^3$), used to collect the data in Fig. 3.12, represented in Fig. 3.13b. The signal voltage for the measurement in Fig.3.12 was around 3 V, and values agreeing with this value are indicated with the black line in both Fig. 3.13a and b, indicating the potential measurement situations according to our estimates.

Based on these data, we see that depending on the loss values, we expect a theoretical shot-noise limit between 0.02-0.1 $\mathrm{pm}/\sqrt{(\mathrm{Hz})}$, indicating that the chip-based LDV is within an order of magnitude of reaching the fundamental performance limit, meaning that major improvements of the detection limit should come from higher power and higher captured reflected power of the chip-based system.

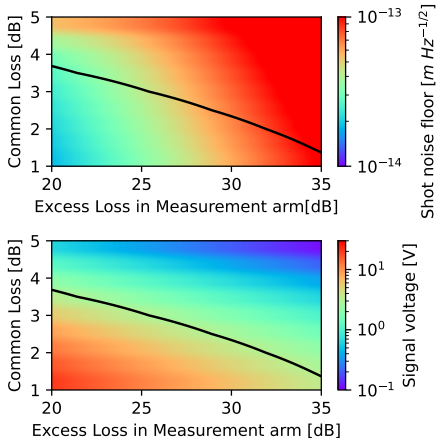

Figure 3.13: Consider an on-chip LDV beam with an output beam of 0.5 mW, assuming a splitting ratio of 60/40 for the power to the measurement and reference arm respectively. a) shows the theoretical shot noise floor for different values of the common loss (= the on-chip losses which are similar for both paths) and the excess loss in the measurement arm. b) shows the expected calculated voltage and black denotes the when the signal is equal to 3V in both figures.

Bandwidth

Although Fig. 3.12 presents data up to 10 MHz, the electronic amplification circuit was designed to have a limited bandwidth up to 3-5 MHz. To characterize the bandwidth, an experiment was designed to measure and compare the pulse response of the on-chip LDV to the commercial LDV. Fig. 3.14 shows a schematic of the experiment. An ultrasound transducer was placed against a 12 mm thick silicone sample, using contact gel to ensure good ultrasound transmission. The transducer was driven using 50 ns, 10 V pulses at a repetition rate of 1 kHz, and time traces were recorded and averaged for both the Polytec and chip-based LDV. After averaging for 100 seconds, the recorded time traces can be compared to give the sensitivity in Fig. 3.14b. Consider $P(f)$ and $C(f)$ to be the calculated Fast Fourier Transform (FFT) spectra of the time traces recorded by the Polytec and the chip-based LDV, respectively, as shown in Fig. 3.14c. Given that the commercial LDV presents an almost flat unity sensitivity for ultrasound frequencies up to 10 MHz, the sensitivity of the chip-based LDV can be estimated as $S(f) = \frac{C(f)}{P(f)}$, provided that the signals are above the noise floor, which in this case extends up to 4.5 MHz.

The resulting sensitivity (Fig. 3.14d) shows a relatively constant value (near unity) up to around 3 MHz. Hereafter the sensitivity drops, resulting in a 3 dB bandwidth

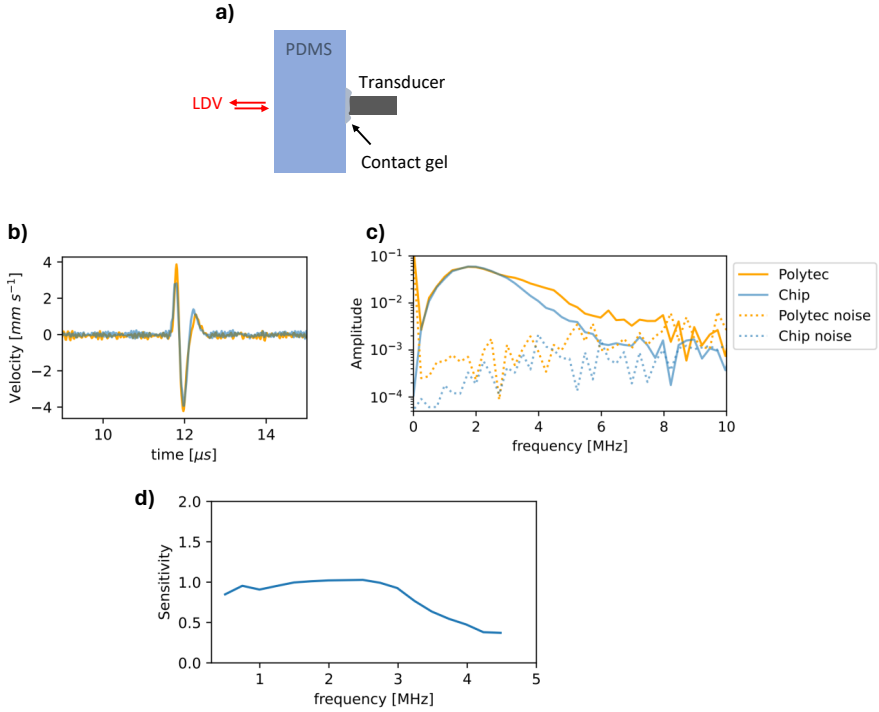

Figure 3.14: a) Schematic of setup used to compare pulse responses, whereby a pulse generated by an ultrasound transducer in contact with the silicone is detected on the opposite side by an LDV. b) The pulse time trace measured by the Polytec (orange) and on-chip LDV (blue). c) Spectra of the pulse response recordings and noise floor spectra. d) The sensitivity from the silicon photonics-based LDV, calculated by dividing the response spectrum of the chip-based LDV by the spectrum from the polytec.

of around 3.5 MHz. This bandwidth will determine resolution characteristics for photoacoustic imaging.

3.6 Theoretical study of optical amplifiers for on-chip LDV

The measurement results in the previous section indicate that we are close to the shot noise limit for the homodyne LDV. To improve upon this fundamental performance limitation, this section explores the inclusion of an optical amplifier into the LDV circuit. Specifically, we consider SOAs due to recent advancements in heterogeneous integration on the silicon-on-insulator platform.

Considering a gain G in the measurement path, we expect a factor $\sqrt{G}$ improvement of the shot noise contribution when $P_m < P_r$.

$$\theta_{n,shotnoise} = \frac{I_n}{I_s} = \frac{\sqrt{4q\mu(P_m + P_r)}}{\mu\sqrt{P_m P_r}} \propto \frac{\sqrt{(P_m + P_r)}}{\sqrt{P_m P_r}} \tag{3.34}$$

3.6.1 Semiconductor Optical Amplifiers for homodyne interferometry

Assuming a narrow linewidth laser, we can disregard the laser's phase noise. Thanks to the balanced detection method described earlier, any relative intensity noise (RIN) from the laser or amplifier can also be neglected, leaving only the different phase noise contributions to be considered. In this study, we also assume that the electronic circuit is designed to reach the shot noise limit, thus neglecting electronic noise sources. The following analysis will focus on the shot noise contribution and the SOA phase noise contribution to the demodulated phase.

Kikuchi et al. described the different physical mechanisms contributing to phase noise in semiconductor optical amplifiers [59]. Spontaneous emission causes direct phase noise due to emitted light that is out of phase (process 1). Furthermore, spontaneous emission causes optical intensity fluctuations which induce carrier density fluctuations inside the gain material (process 2). Recombination processes also cause direct fluctuation of the carrier density, adding to phase noise (process 3). Equations 3.35, 3.36, and 3.37 describe the power spectral density of these different noise sources. Processes 1 and 2 depend on the optical power in the amplifier. Therefore, the position of the optical amplifier in the homodyne LDV is important. For frequencies below $\frac{1}{2\pi\tau_e}$ (usually in the 1 GHz region), the power spectra can be assumed flat and will have the following magnitudes [59]:

$$\text{Process 1: } S_{\phi 1} = \frac{h\nu(G-1)n_{sp}}{P_{out}} \tag{3.35}$$

$$\text{Process 2: } S_{\phi 2} = \left(\frac{2\pi K\Gamma}{\lambda A}\right)^2 4(G-1)n_{sp}\tau_e^2 \frac{P_{out}}{h\nu} \tag{3.36}$$

$$\text{Process 3: } S_{\phi 3} = \left(\frac{2\pi K\Gamma}{\lambda A}\right)^2 2N_t\tau_e \tag{3.37}$$

The parameters used in these equations are explained in table 3.2. To simulate an SOA in our homodyne on-chip LDV, we will use the values from a traveling-wave GaInAsP optical amplifier from [59] as noted in table 3.2.

Parameter	Symbol	Value
Wavelength	λ	1.52 μm
Internal Gain	G	20 dB
Output Power	P_{out}	variable [mW]
Length	L	500 μm
Cross section	A	0.38 μm^2
Optical confinement factor	Λ	0.57
Spontaneous emission factor	n_{sp}	2
$\frac{\Delta\text{refractive index}}{\Delta\text{electron density}}$	K	$4.10^{-26} m^3$

Table 3.2: Parameters and Values used for simulation of an SOA. Retrieved from [59]

When considering the shot noise contribution to the demodulated phase (Eq. 3.34), it is evident that using an optical amplifier after the splitter is most beneficial when one arm has less power than the other. In LDV applications, we can imagine that the power in the measurement arm suffers the most attenuation due to the small efficiency of coupling light back into the chip after reflection from a target. We therefore can assume this is the origin of the excess loss of optical power in the measurement arm compared to the reference arm. In the following analysis, we will therefore only look at the influence of placing an amplifier in the measurement arm.

It is possible to place an SOA either before or after the antenna as depicted in Figure 3.15. Since the optical power input into the SOA influences the noise, this placement could affect performance because it is either before or after the bulk of the excess loss in the measurement arm. However, it is important to note that preferably, the power in the measurement arm cannot be amplified before the antenna since the output is already close to the safety limit. Therefore, we initially consider a situation where we have an output beam equal to 10 mW (the safety limit) and we place the amplifier after the antenna.

Amplifier in an LDV with high optical power

Consider a situation when the output beam is equal to the safety limit (= 10 mW) and the reference arm has a power of 1 mW. Fig. 3.16a shows the phase noise contributions for the SOA after the antenna depending on the excess loss (occuring before the SOA). It can be seen that with high excess loss (> 30 dB), the phase noise increases rapidly due to the out-of-phase spontaneous emission (process 1). For lower excess losses (< 30 dB), the carrier density fluctuations induced by the optical intensity fluctuations are the major contributor to the SOA phase noise.

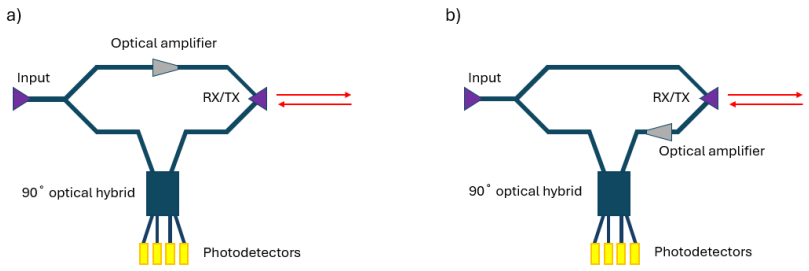

Figure 3.15: Optical amplifier in measurement arm; a) after antenna and b) before antenna

To determine if an amplifier could improve the LOD of the vibrometer, we need to compare the shot noise influence and the influence of the noise induced by the SOA on the overall LDV noise. When the SOA is in the measurement arm, the SOA phase noise directly translates into LDV noise (noise on the demodulated phase).

Fig. 3.16b plots the shot noise limit with and without the SOA and also shows the SOA phase noise. In the situation with an SOA, it is clear that the SOA-induced phase noise is much larger than the shot noise. Due to this large contribution of the SOA phase noise, there is even performance degradation for excess losses lower than 30 dB, while for higher excess losses, the situation with the LDV only demonstrates very small performance improvement. From these figures, it can be concluded that for the situation of an LDV showing an output close to the safety limit, adding an SOA in the measurement arm after the antenna does not provide a considerable performance improvement and can even degrade the performance due to the SOA-induced phase noise.

Amplifier in an LDV with low optical power

Now, let us consider a situation where the $100\ \mu$W of optical power is coupled in the reference arm of the LDV and the power of the LDV beam is also $100\ \mu$W. In this case, the SOA can be placed either before or after the antenna to amplify the output beam while staying below the safety limit.

Fig. 3.17 and Fig. 3.18 show the estimations of the phase noise contribution for the configuration with the amplifier before and after the antenna.

Similarly, as for the high power LDV, Figure 3.17a shows a significant dependence on the excess loss, with the tipping point of the dominant contributions around -10 dB. On the other hand, when the SOA is before the antenna (figure 3.18) the

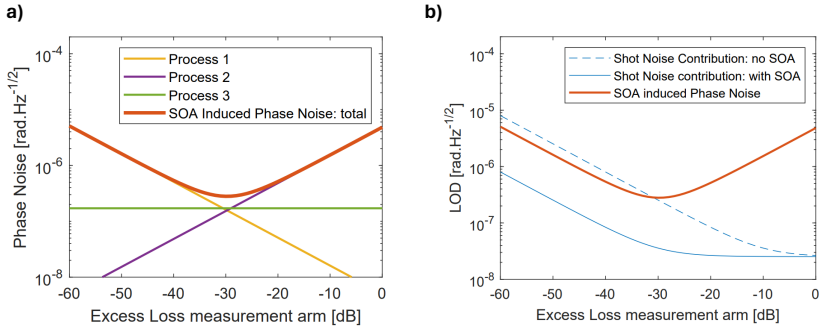

Figure 3.16: a) Plot of the SOA phase noise contributions as a function of the excess loss in the measurement arm after the antenna when the LDV output is 10 mW and the power in the reference arm is 1 mW. b)Comparison of the shot noise limit with and without SOA and the SOA phase noise

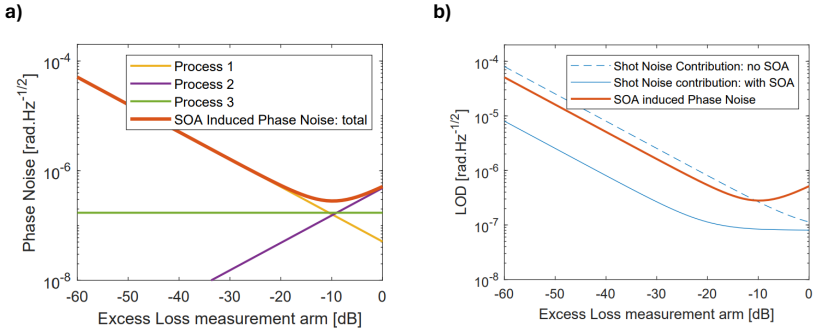

Figure 3.17: a) Plot of the SOA phase noise contributions as a function of the excess loss in the measurement arm after the antenna when the LDV output is 100 uW and the power in the reference arm is 100 uW. b)Comparison of the shot noise limit with and without SOA and the SOA phase noise

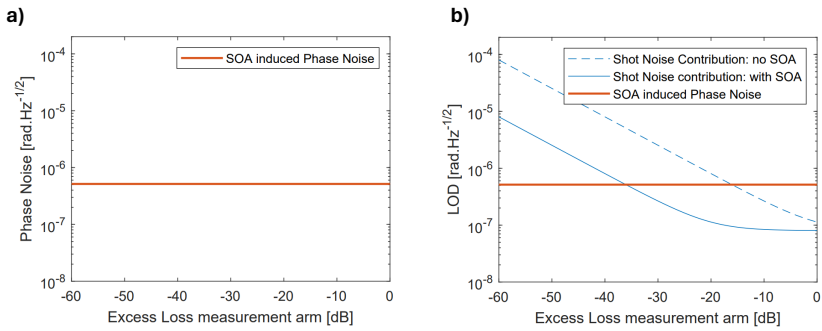

Figure 3.18: a) Plot of the SOA phase noise contributions in the measurement arm before the antenna as a function of the excess loss, when the LDV output without gain is 100 uW and the power in the reference arm is 100 uW. b)Comparison of the shot noise limit with and without SOA and the SOA phase noise

power into the SOA is larger, and the phase noise does not depend on the free space losses, thus remaining constant for different excess loss values, assuming the excess loss originates from free space losses.

For both situations, the expected shot noise and phase noise can be plotted against the shot noise limit without an SOA. The dotted blue line represents the situation without an SOA (only considering shot noise). This should be compared against the shot noise contribution with an SOA (solid blue line) and the SOA-induced phase noise (orange line). Similarly to the high power LDV, Fig. 3.17b shows that placing the amplifier after the antenna does not significantly improve the LOD because the SOA phase noise is similar to the shot noise contribution without an SOA. However, from Figure 3.18b, one can see that placing an optical amplifier before the antenna can yield an improvement when the excess loss is around -15 to -20 dB or more. This is when the shot noise contribution without an amplifier is higher than the SOA-induced phase noise, which is the case for high amounts of excess loss. When the excess loss is -35 dB or more, there is an expected improvement of around 10 dB with the amplifier. Due to the optical amplification, the shot noise contribution is reduced.

3.6.2 Comparison to Erbium Doped Fiber Amplifiers

Various studies [60, 61] show that Erbium-doped fiber amplifiers (Erbium-Doped Fiber Amplifiers (EDFAs)) generally provide better performance in terms of phase noise compared to semiconductor optical amplifiers (SOAs). Typically, the phase

noise improvement of EDFAs over SOAs is less than 10 dB [61], with the exact improvement depending on the input power. Despite these performance benefits, there are notable challenges in applying EDFAs to on-chip homodyne interferometry.

A primary challenge is that EDFAs require an optical pump source to create population inversion, which contrasts with SOAs that can be electrically pumped. This reliance on optical pumping generally makes EDFAs more costly and complex to integrate. On the other hand, SOAs benefit from simpler and cheaper production processes.

Recent advancements, however, have made strides in integrating EDFAs into photonic circuits. For example, photonic integrated circuits incorporating an Erbium-doped waveguide have been demonstrated [62], but without the optical pump source integrated. SOAs on the other hand, have been widely demonstrated to be integrated-with techniques such as transfer printing [49] offering a pathway for cost-effective and compact integration of optical amplifiers on-chip.

Thus, while progress is being made in integrating EDFAs into photonic circuits, the integration of SOAs remains more drelevant for on-chip applications due to established techniques that enable efficient and economical integration.

3.7 Multi-point on-chip LDV

Similar to ultrasound imaging, acoustic resolution photoacoustic imaging requires the detection of photoacoustic vibrations at different locations on the sample to enable photoacoustic imaging. While fiber-based LDVs, which use several discrete components, become bulky and expensive when scaling beyond a couple of beams, a silicon photonics implementation allows for a smaller footprint of the entire system [15].

Although the photoacoustic demonstrations in this work focused on using a single beam, a six-beam design has been demonstrated [15]. Scaling to more beams on the PIC is feasible, as shown in Figure 3.19, which illustrates the layout of a 16-beam LDV on a 5 x 2.5 mm chip.

The input light is split into a measurement path and a reference path, each of which is further divided into 16 different paths for the different beams. For each beam, the signals are combined in a hybrid with PDs, and similar to a single-point LDV, the I and Q signals can be read out from the PDs. Note that the proposed layout requires a significant number of electrical pads, which could become a limiting factor when scaling to more beams. In Chapter 5, we propose an alternative architecture to address this issue.

Another solution for detecting vibrations at multiple locations is to use a scanning LDV implementation, such as an optical phased array. This approach measures at a single location at a time, meaning that the scanning process would result in a longer acquisition time for photoacoustic imaging.

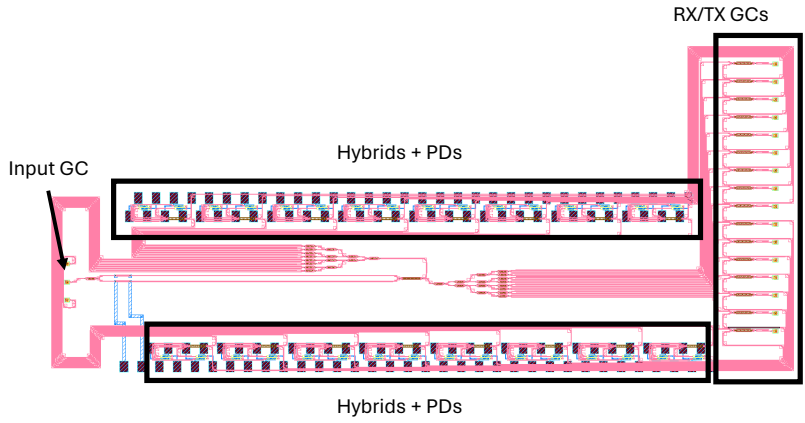

Figure 3.19: Layout of a 16-beam LDV on a 5 x 2.5 mm chip

3.8 Closing Remarks

In this chapter, we have described the implementation of a chip-based LDV and the origin of noise and non-linearities in the system. Before evaluating the performance of the LDV, Section 3.3 discusses the fundamental noise limit for an LDV due to shot noise. The current implementation shows that we are within one order of magnitude of the shot noise limit for an output power of 0.5 mW. Although this performance is near the shot noise limit, a comparison against a contact-based transducer reveals a noise floor around 3 orders of magnitude higher for an LDV in the MHz region. While LDV is better for contactless detection, these results highlight the fundamental challenges for photoacoustic detection with LDV and indicate that contactless photoacoustic imaging will come at a performance cost compared to contact-based detection. The influence on the performance for photoacoustic imaging will be discussed in the next chapter.

Since we have performance near the shot noise limit, increasing the signal amplitude by either using or collecting higher optical powers while staying within safety limits seems to be the best option to further improve performance. In the demonstrated

implementation, the output power was limited to 0.5 mW, as higher powers would lead to saturation in the electrical amplifier circuit. Therefore, the demonstrated system is constrained by saturation in the electrical amplifier circuit.

Besides increasing the laser power into the LDV or improving the collection efficiency of the reflected light, another approach would be to amplify the signal with a SOA in the measurement arm. Section 3.6 examines whether we can improve upon the shot noise limit by using SOAs in the measurement arm. The results, however, do not show considerable improvement when the SOA is placed after the antennas. Only when the safety limit of the output beam is not yet reached with the optical power does an amplifier to boost the power of the output beam present an opportunity to significantly improve upon the shot noise limit without an amplifier.

The results from this chapter demonstrate a high-performing LDV system and its ultrasound measuring capabilities. Although an increase in noise compared to contact-based detection is evident, the next chapter will demonstrate and describe how an LDV can still be effectively used for contactless photoacoustic imaging.

4

Non-contact Photoacoustics using Silicon Photonics-based Laser Doppler Vibrometry

4.1 Introduction

This chapter combines the theory and background of photoacoustic imaging discussed in chapter 2 with the silicon photonics-based detection technology introduced in chapter 3. This combination results in a pioneering demonstration of contactless photoacoustic detection and imaging using a silicon photonics-based LDV. Furthermore, to showcase the potential of a miniature system, a small and contactless excitation source was employed to generate the photoacoustic effect, contrasting to conventional photoacoustic systems that typically use expensive and bulky high-power lasers.

First, we explore the design considerations for the detection system, addressing the desired detection bandwidth and explaining how averaging can further reduce the total noise floor, enabling the detection of photoacoustic signals.

Next, we detail the implementation of the photoacoustic demonstration, covering the detection system, phantom, and excitation source.

Sections 4.4 and 4.5 present the measurement results of this lab setup, demonstrating 2D photoacoustic imaging. In Section 4.6, the 'Discussion' section, we delve into these results, examining and analyzing the signal strength and 2D imaging characteristics. We also address potential performance degradation and challenges that may arise when transitioning to in-vivo photoacoustic imaging using silicon photonics-based LDVs.

4.2 Design considerations

The previous chapter indicated that the LDV detection bandwidth significantly influences the total NEP. A smaller bandwidth results in a lower NEP, enabling photoacoustic detection at greater depths. On the other hand, reducing the bandwidth decreases the attainable image resolution (Section 2.2.3). In this section, we show the calculations made to create a decision on this balancing act of choosing an appropriate detection bandwidth.

First, we estimate the expected photoacoustic signal strengths in an ideal scenario where the excitation source exposure equals the maximum skin safety limits. According to the ANSI safety limit, the maximum permissible exposure limit is $F_0 = 15\ \mathrm{mJ/cm^2}$ at 900 nm [63]. Considering an absorber of blood at a depth d from the surface and using the photoacoustic theory described in Chapter 2, we can estimate the magnitude of the initial pressure. Assuming a $140\ \mathrm{mg/ml}$ hemoglobin concentration, which is a typical physiological value, leads to an absorption of around $\mu_a = 6\ \mathrm{cm^{-1}}$ at 900 nm [64]. We consider the surrounding tissue and skin to have an effective attenuation between $1 - 10\ \mathrm{cm^{-1}}$ to estimate the fluence at depth d.

The deposited energy per pulse at the blood absorber $h(x = d)\ [\mathrm{J/m^3}]$ is calculated as:

$$h(x = d) = \mu_a F_0 \exp(-\mu_{eff} d) \tag{4.1}$$

The effective attenuation coefficient, μ_{eff}, represents the combined effect of absorption and scattering on the attenuation of light as it propagates through the tissue. This parameter is crucial for modeling how light intensity decreases due to both energy being absorbed by the tissue and light being scattered in different directions.

Mathematically, μ_{eff} is often calculated as [65]:

$$\mu_{\text{eff}} = \sqrt{3\mu_a \left(\mu_a + \mu_s'\right)}$$

where μ_a is the absorption coefficient and μ_s' is the reduced scattering coefficient. Considering typical tissue absorption of around $0.5\ \mathrm{cm^{-1}}$ [64] and a typical reduced scattering between $5 - 60\ \mathrm{cm^{-1}}$ [66], depending on the type of tissue, typical values for effective attenuation in tissue range between $2 - 10\ \mathrm{cm^{-1}}$.

As explained in Chapter 2, for a short pulse, we can estimate the initial pressure to be:

$$p_0 = \Gamma h(x) \tag{4.2}$$

According to [67], the Grüneisen parameter for whole blood is around $\Gamma = 0.2$. With these assumptions, we can estimate the initial pressure at different depths, as seen in Fig. 4.1. This figure indicates that the initial pressure largely depends on the depth of the absorbing target and the effective attenuation of the surrounding media. Initial pressures range from the kPa-range down to the Pa-range for depths up to 1 cm.

It is important to note that the initial pressure is usually not equal to the pressure detected at the surface of the phantom since the propagation and divergence of the acoustic wave decrease the amplitude. However, for a uniform excitation and

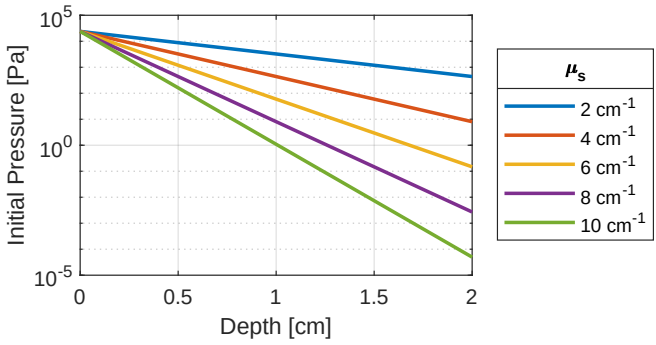

Figure 4.1: Estimated initial pressure at varying depths for different scattering coefficients of the medium

infinitely large absorption layer in the directions parallel to the surface, the pressure amplitude arriving at the surface is similar to the initial pressure due to the lack of divergence losses.

In the previous chapter, the noise spectrum was measured to be around $1 - 2\mathrm{Pa}/\sqrt{\mathrm{Hz}}$ at MHz-frequencies. For a bandwidth of a couple of MHz, the total noise equivalent pressure is, therefore, in the kPa range. As presented in Fig. 4.1, a total noise floor in the kPa range means that detection without averaging is limited to a depth of a few mm for highly scattering tissue. For media with a low scattering coefficient, the detection depth could go beyond 1 cm.

Fig. 4.1 clearly indicates that a lower noise floor (e.g. by a smaller detection bandwidth) comes with the benefit of a larger attainable detection depth. A bandwidth-limited resolution can be estimated as $0.8\lambda_c$, where λ_c is the cutoff acoustic wavelength for the detection bandwidth [1, 40]. Assuming a tissue-like medium with an acoustic impedance of approximately 1.5 MRayl, a bandwidth of 3-5 MHz corresponds to a resolution of $250 - 400\ \mu\mathrm{m}$. Although increasing the bandwidth into the high ultrasound range (10 MHz and above) can achieve superior photoacoustic imaging resolutions, the silicon photonics-based detection system was optimized for a 3-5 MHz bandwidth. This choice was driven by predictions indicating that the laser Doppler vibrometer (LDV) noise performance would remain in the lower kPa range, which still presents reasonable attainable imaging depths according to Fig. 4.1 and reasonable image resolution.

As described in Section 3.5 from the previous chapter, the measured bandwidth was around 3.5 MHz and presented an NEP of around 2 kPa.

Considering the assumption of ideal illumination and neglection of acoustic diver-

gence effects, this NEP is relatively high compared to the estimated initial pressures at depths above 5 mm. The noise floor can, however, be reduced further by averaging different acquisitions. Assuming the photoacoustic signals are repeatable, averaging multiple acquisitions can still yield an accurate representation of the actual signal. Assuming a random noise source, averaging reduces the noise by a factor of $\sqrt{(N)}$, where N is the number of acquisitions. In practice, averaging over 1000 acquisitions (measured during 1 s), resulted in noise reduction of around 32, yielding a NEP of 63 Pa after averaging.

4.3 Implementation of the photoacoustic system

This section details the lab demonstration of miniature and non-contact photoacoustic imaging using a silicon-photonics-based LDV. Fig 4.2 shows a schematic of the lab setup. We discuss each part of this system in more detail before expanding on the measurement procedure and results.

The photoacoustic system comprises three primary components, each of which is discussed in detail in subsequent sections. First, there is the detection system, which includes the LDV PIC, a lens system, the amplifier electronics, and the acquisition module.

Secondly, the phantom which is represented by a PDMS phantom with an embedded ink channel. We provide a detailed description of its development and properties.

Thirdly, the excitation source consists of a miniature pulsed laser source. Both the excitation laser and the phantom are mounted on a 1D scanning stage, facilitating 2-dimensional imaging.

4.3.1 Detection system

In Chapter 3, we discussed the theory, working principles and characterization of the silicon photonics-based detection system. Here, we present how it is implemented in the lab setup. For the detection system, we consider the elements depicted Fig. 4.4a; A lens system focuses the light from the PIC on a phantom; after reflection and optical processing, the optical signals are converted to electrical signals on the PIC and amplified on a PCB before saving them on a laptop using an ADC.

A PIC containing the layout of a six-beam LDV (similar to [15] and as presented by the schematic in Fig. 4.3a) was used.

Fig. 4.3b shows the free-space imaging system used. A confocal imaging system

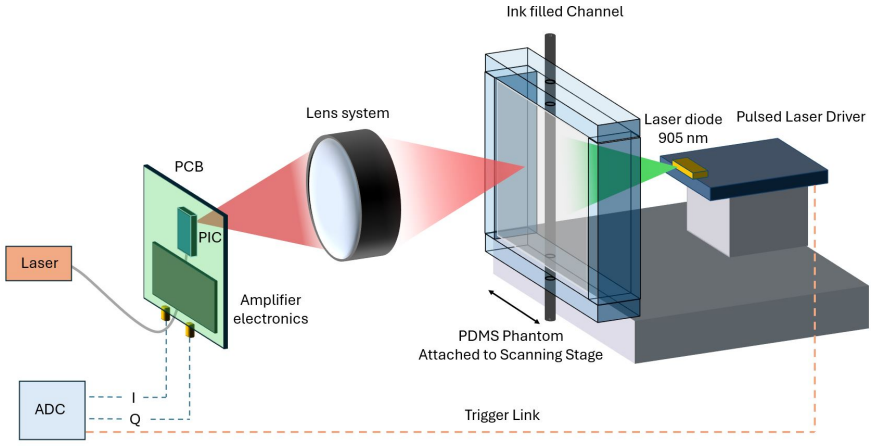

Figure 4.2: Schematic of photoacoustic system for demonstrating on-chip LDV

was used to create parallel beams with around 5 mm pitch at the target using a 6 mm diameter ball lens and a double convex lens with a focal length of 75 mm, resulting in a Magnification of $M \approx 16.7$. The pitch of 5 mm combined with the relatively large imaging distance makes it a flexible setup that allows testing each beam separately and adding optical elements between the target and double convex lens (e.g. high NA lenses, aperture, high pass filters,..). Nonetheless, without any added elements, the optics as described in 4.3b make for a very small NA due to the large magnification. The NA can be estimated by considering the NA of the grating coupler divided by the magnification. Considering the NA of a grating coupler to be similar to a single mode fiber (SMF-28, NA=0.14) the estimated NA is around 0.008. Although this does not allow to measure vibrations on surfaces with highly diffuse reflection, it comes with the benefit of a large depth of focus (± 10 mm). With such a large depth of focus, the LDV can be scanned over the surface of the phantom without the need to change the focus. In the following sections, we measure on a specularly reflective phantom to ensure good collection efficiency after careful alignment of the phantom and LDV system.

The PIC was wire-bonded to an interposer PCB, and fiber was glued to the input coupler to ensure stable light coupling into the chip, as seen in the picture in Fig 4.4b. While the PIC accommodates 6 beams, in the experiments conducted in this work, we focused on using a single LDV beam, since the wire bonds of several channels were broken and unrepairable, and photoacoustic imaging required scanning anyway.

A picture of the PIC attached to the amplifier PCB and the free-space optics can be seen in figure 4.4c.

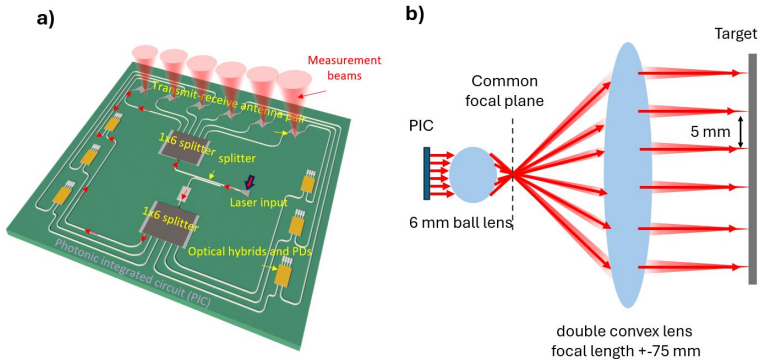

Figure 4.3: a) Schematic of the six-beam LDV layout, reproduced from [15] b) Schematic of the confocal imaging system creating parallel beams with 5 mm spacing.

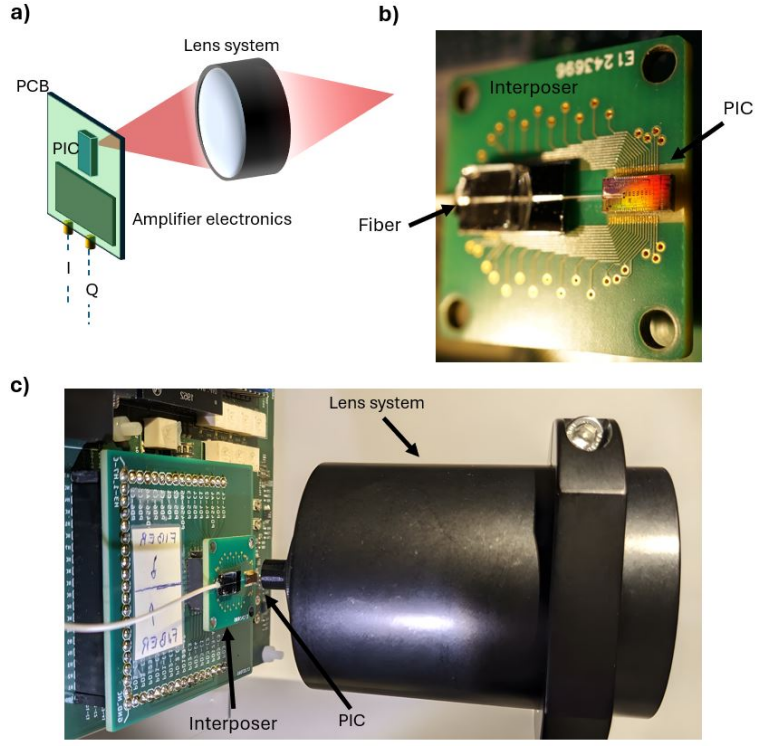

Figure 4.4: a) Schematic of the detection system b) Picture of a PIC wire-bonded to an interposer with a glued optical fiber to deliver light for the LDV. c) Picture of the PIC attached to the amplifier electronics and the free-space optics to focus light on the target.

The interposer redistributes the PD signals to an amplifier board, where the dual-stage unbalanced detection method was used as described in Chapter 3, to obtain I and Q signals to 3.5 MHz.

In the first stage, the current of each PD is converted to a voltage with a TIA and a feedback resistor of 22 $\mathrm{k}\Omega$. The second stage differentially amplified with a factor of about $51/3.3 \approx 15.5$, combining to a total conversion resistance of 340 $\mathrm{k}\Omega$ such that $V_{out} = 340\mathrm{k}\Omega(I_a - I_b)$.

After differential amplification of the PD pairs, the Gage Octopus express digitizer coverted the analog I and Q signals to the digital domain before transferring the data to a Personal Computer (PC). This 14-bit digitizer can handle up to 8 input channels at 65 MS/s. As will be explained in Section 4.4.1, triggered acquisition can be used to ensure accurate timing between photoacoustic excitation and recording.

Due to various non-idealities, such as imbalance in the detection system or phase errors, as discussed in Section 3.4, the IQ signals did not constitute a perfect circle. At higher optical LDV powers, the I and/or Q signals saturated the electrical amplification due to a large DC offset, which limited the optical power and consequently, the fundamental detection limit. In the experiments we tuned the operating temperature of the laser source, the alignment and optical input power to minimize the DC error, while maximizing the IQ radius and avoiding clipping by exceeding the limits of the amplifier circuit.

As discussed in Section 4.2, averaging is essential to detect photoacoustic signals lower than the NEP. However, effective averaging requires precise and repeatable timing synchronization between the pulse excitation and the data acquisition. To achieve this, a trigger link between the pulse excitation and the ADC was implemented, as shown in Fig. 4.2.

4.3.2 Phantom

To facilitate lab demonstrations of photoacoustic detection, we developed silicone phantoms containing ink channels to serve as absorbers. We chose silicone material because its acoustic properties resemble those of biological tissue and it is easy and safe to process. Specifically, we used PDMS (Sylgard 184), which has a speed of sound in the range of 1000 to 1050 m/s [68, 69]. Although the typical speed of sound in human tissue is generally higher, ranging from 1400 to 1700 m/s, PDMS offers a practical and easily processable alternative.

Flat phantoms were designed to take advantage of direct specular reflection from the PDMS when using the 1550 nm LDV. The reflectance of PDMS is around $R = 0.027$. This material is non-scattering and non-absorbent at the excitation

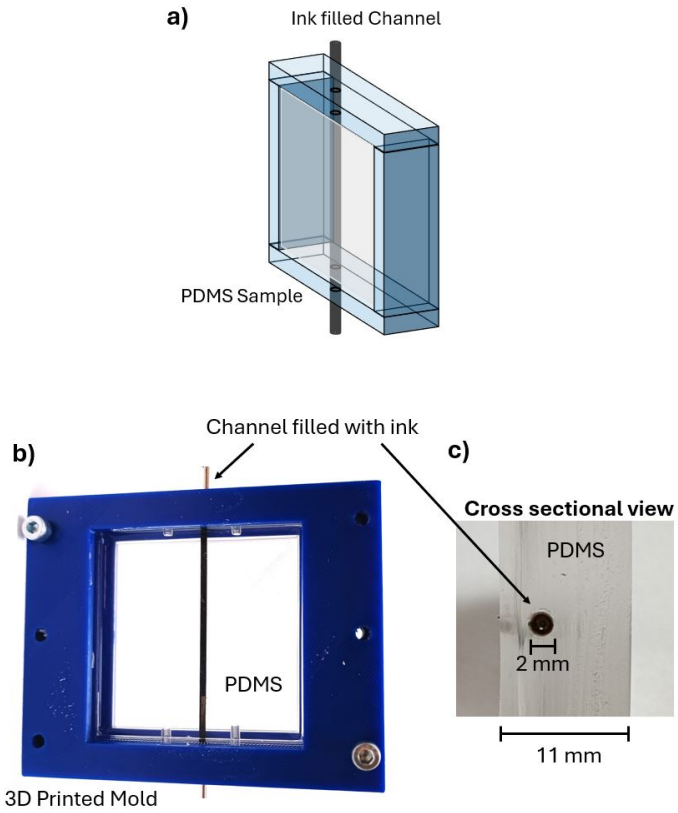

Figure 4.5: a) Schematic of the PDMS phantom with an embedded ink channel. b) 3D printed mold (blue) filled with transparent PDMS and a channel filled with ink. c) Cross-section of the PDMS phantom near the ink channel. This phantom had a cross-sectional width of around 11 mm, and the width of the channel is estimated to be around 2 mm.

wavelength, making it easy to distinguish the signal from the introduced absorber. The absorber, an ink-water solution, is introduced through a 2 mm channel within the PDMS phantom.

The process for developing the phantom is depicted in Fig. 4.6. The phantom with the channel was created by first producing a 3D-printed mold with metal rods, with a 2 mm diameter, inserted at the locations of the channels. Next, a Sylgard 184 mixture was prepared, and air bubbles were eliminated by cycling the mixture under vacuum and atmospheric pressure. Hereafter, the mixture was poured into the mold and cured overnight at 40 degrees Celsius. After curing, the rod was removed, and plastic tubing was attached to the mold to deliver ink into the channel. With these phantoms, different absorption concentrations can be tested by changing the ink or

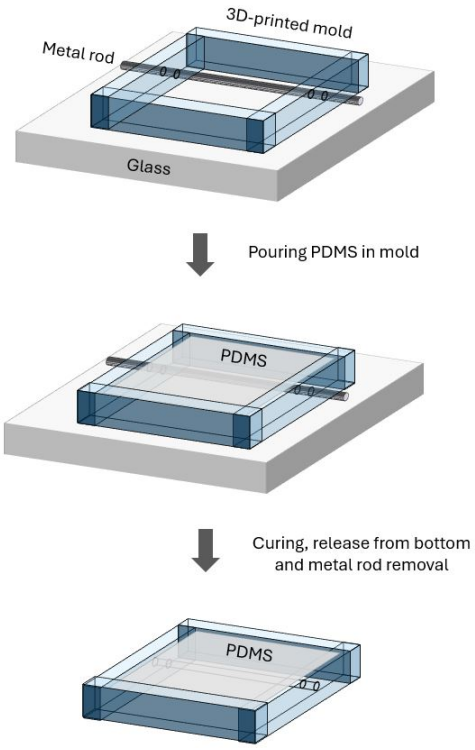

Figure 4.6: Schematic of the phantom preparation. First, a 3D printed mold was prepared with a metal rod running through the mold to create a channel in which later ink is introduced to act as the photoacoustic absorber. Hereafter, PDMS was poured into the mold, and after curing, the rod was removed, and the phantom was ready to be used for photoacoustic experiments.

ink concentrations in the channels.

The ink dye used in the experiments was black India ink (Dr. Ph. Martens Bombay Black India ink), which has a broad absorption region extending into the Near Infrared (NIR) range. The absorption spectrum for a 0.05 V% ink concentration in water is depicted in Fig. 4.7. The spectrum was measured with a spectrophotometer (LAMBDA 1050+ UV/Vis/NIR), which measured the reduction of intensity after passing through $1\ cm$ of the ink-water mixture. Assuming a small scattering coefficient compared to the absorption coefficient, the optical absorption can be estimated as depicted in Fig. 4.7.

The spectrum shows an optical absorption of around $6\ \mathrm{cm}^{-1}$ at 900 nm. It indicates that an ink concentration of around 0.05% provides an absorption around the physiological range for blood absorption. The channel facilitates changing the absorber

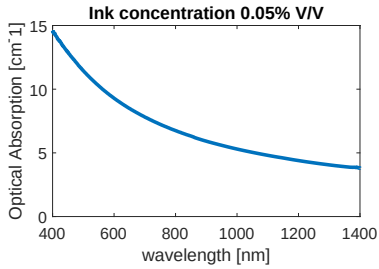

Figure 4.7: Absorption spectrum of Black India ink for 0.05% concentration in water

liquid, and by adjusting the ink concentration, different absorption strengths can be measured.

4.3.3 Excitation source

Conventional photoacoustic imaging for medical applications typically utilizes high-power pulsed lasers such as Q-switched Nd:YAG lasers [2, 5] . These lasers are generally bulky and expensive. We employ smaller sources such as laser diodes or bars to develop a more compact and cost-effective contactless system. Although these sources have lower power than high-power pulsed lasers, they offer advantages in size and cost. Additionally, adhering to safety regulations, lower energy pulses can be fired at higher repetition rates. This approach allows for acquiring a larger number of averages within the same measurement time compared to systems using high-power lasers. While the photoacoustic signal strength scales linearly with the optical fluence, averaging N times only reduces the noise floor with a factor $\sqrt{N}$, meaning that for a similar average power, a high pulsed laser is still preferred. Nonetheless, the averaging partially compensates for the loss of signal strength due to lower fluence values.

Regarding wavelength selection, the NIR window is preferred due to several factors. The difference in absorption between oxygenated and deoxygenated hemoglobin is significant in the NIR range. Additionally, unlike visible light, NIR light is not entirely absorbed by superficial tissue layers and exhibits minimal water absorption.

For most experiments discussed in 4.5 and 4.4, we employed the SPL S4L90 Osram laser diode, a commercial laser diode package consisting of 4 tightly packed emitters at 905 nm, resulting in a output beam with divergence angles (FWHM) of 10°(slow-axis) and 25°(fast-axis). The laser diode was placed at a distance of 3-7 mm from the phantom's surface without any additional optics. This laser diode was soldered onto a small interposer board connected to a commercially pulsed

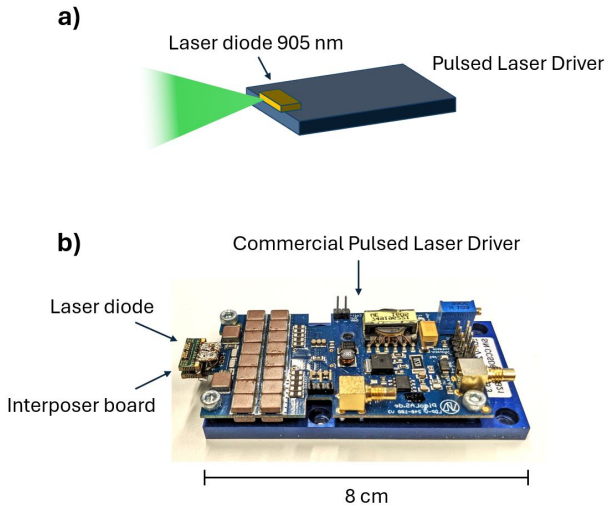

Figure 4.8: a) Schematic of the pulsed laser driver and diode. b) picture of the Osram SPL S490L laser diode mounted on the Picolas commercial pulsed laser driver.

laser driver (Picolas LDP-V240-100). With this laser driver, the laser diode was driven to its maximum in terms of peak power and peak current, according to the datasheet without any added heatsink. The laser driver allowed for pulse lengths of 100-500 ns and peak driving currents of up to 160 A, the maximal current according to the SPL datasheet. This maximum current results in 480 W of optical peak power, according to the datasheet. For most experiments, the laser diode was driven at 1 kHz with a pulse length of 400 ns, resulting in approximately 0.2 W of average power and around 200 μJ of pulse energy, which is within the ANSI skin exposure safety limits [63].

Although this commercial laser diode provides a high-power laser diode at 905 nm, a similar diode at other NIR wavelengths, which would be interesting for quantitative oxygenation, were not readily available. In the search for alternative sources, laserbars present themselves as a promising alternative. First of all, laserbars at various wavelengths are commercially available. Secondly, laserbars can generate high peak optical output power. Thirdly, laserbars naturally present a uniform illumination along the laserbar array axis, which can ease the uniform illumination preferred for photoacoustic imaging, as will be explained in Section 4.5.4. Here, the 915 nm laserbar (Jenoptik, JDL-BAB-75-35-915-TE-500) was mounted on a similar pulsed laser driver, depicted in Fig. 4.9. This 9.8 mm long laserbar consist of 37 emmiters next to each other and presents an output with a slow-axis divergence (FWHM) of 9°and a fast-axis divergence of around 25°. The laserbar was placed at a distance of a 2 mm from the phantom's surface without any collimating optics.

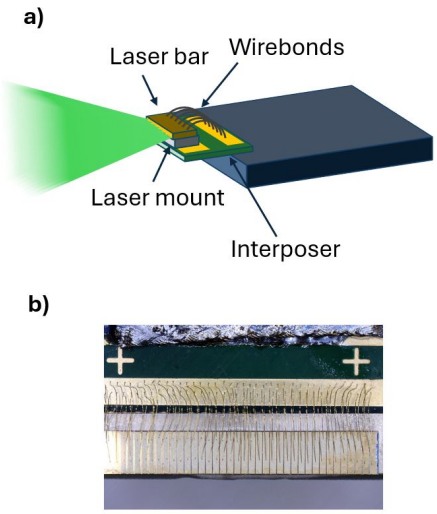

Figure 4.9: a) Schematic of the pulsed laser driver and wire-bonded laserbar on the interposer. b) Top view of the laserbar wire-bonded on the interposer.

The influence of the illumination profile is discussed in Section 4.6.1.

First, the laserbar was mounted on a submount by a commercial packager. Subsequently, this lmount was soldered on an interposer, and the top side was wire-bonded to the other electrode of the interposer. The laserbar presents a maximum peak optical power of 500 W according to the datasheet, but due to the current limitations of the laser driver (max 240 A), the realized peak power was around 250 W. The laserbar was operated with the same repetition rate (1 khz) and pulse length (400 ns) as the laser diode.

It can be noted that, even when placing the laserbar or laser diode close to the phantom, the fluence is much lower compared to the maximum allowed pulse power ($= 15\ \mathrm{mJ/cm^2}$). However, the higher repetition rate of the laser diode allows for averaging more acquisitions in the same measurement time, which slightly compensates for the lower fluence and, thus, lower photoacoustic signal strength. Major benefits compared to bulky high power lasers are however the size and cost. The commercial driver with a laser diode/bar take up a total of around 8-by-4 cm and can be developed at a relatively low cost ($< 1K$ EUR).

4.4 Single point photoacoustics

4.4.1 Method

In this section, we look at photoacoustic signals captured using the setup shown in Fig 4.2. As mentioned in Section 4.2, the photoacoustic signals are relatively small compared to the detection limit of the LDV. Therefore, it is not only essential to ensure good alignment of the phantom and LDV but also to perform averaging, as mentioned before.

Before the measurement, the LDV beam was aligned such that the laser diode was directly facing the LDV beam. Then, the phantom was placed 3 mm from the laser diode and with the ink channel aligned with the center of the laser diode. The fast-axis of the laser diode was placed transverse to the ink channel. Thereafter, the LDV focus and the phantom's pitch and yaw were carefully changed to optimize the amplitude of the captured reflected light by the LDV, by maximizing the radius of the IQ-circleduring alignment.

In order to employ averaging, accurate timing between different acquisitions needs to be ensured. Each time the laser diode fires a pulse, a trigger signal is sent to the digitizer, signaling the start of a new recording. The digitizer settings allowed for the detection of a variable number of samples for each trigger event and saving several datapoints measured before the trigger event.

It is, however, essential to consider that averaging the I and Q signals for different recordings before demodulation is not a viable option. This can be most easily understood with the following reasoning.

A photoacoustic signal generates a small vibration. This vibration causes the phase of the IQ circle to go from θ_0 to $\theta_0 + \delta\theta$ and back. Now, when a second segment is acquired later, consider a low-frequency vibration that shifts the DC phase to another point on the IQ circle, with phase θ_1. There the photoacoustic signal moves the phase of the IQ circle from θ_1 to $\theta_1 + \delta\theta$ and back. When $\theta_1 = \theta_0$, the demodulation of the average of the I and Q signals will yield accurate displacement of the photoacoustic signal. Generally however, θ_1 is not equal to θ_0. In this case, the sum of the I and Q signals of both acquisitions does not allow for accurate demodulation. To clarify this, consider the situation where $\theta_1 = \theta_0 + \pi$, then the sum of both acquisitions of small vibrations around these DC phases will result in a zero signal for both I and Q.

In order to circumvent this problem, it is essential to demodulate before averaging.

Due to system imperfections and nonlinearities, as discussed in the previous chap-

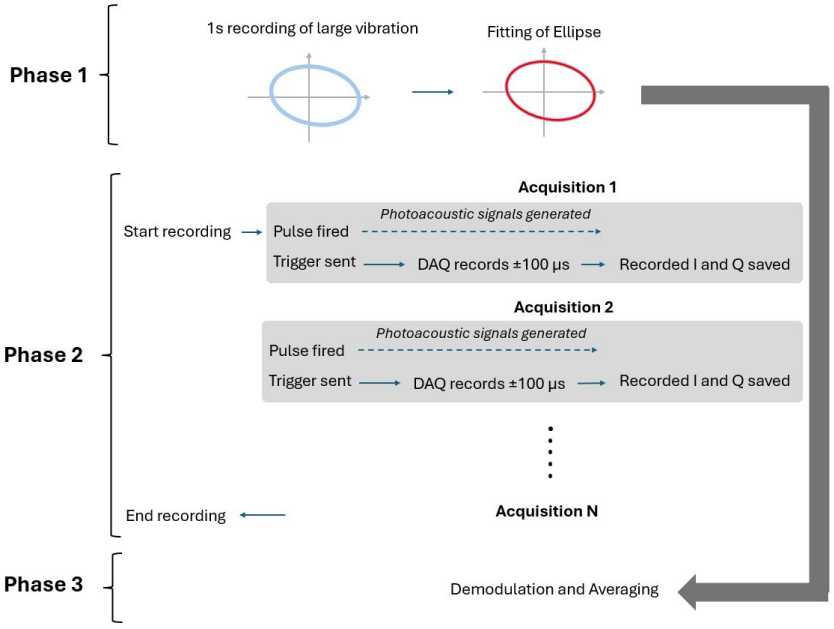

Figure 4.10: Schematic of the measurement procedure for a single point photoacoustic measurement with the on-chip LDV.

ter, we have to use an advanced demodulation method. Here, the Heydemann method was employed [56]. However, it is important to note that the Heydemann method requires raw I and Q data that spans a complete 2π phase change to accurately fit an ellipse. For each trigger event, we record only a limited number of samples—sufficient to capture the photoacoustic signals but small enough to stay within the data limitations of our system. Consequently, these brief acquisitions are inadequate for accurately fitting the ellipse.

Therefore, the measurement procedure was adapted to go as follows and is depicted in Fig. 4.10. As illustrated in Phase 1 of Fig. 4.10, we first captured a longer recording by inducing a large vibration (by tapping the optical table). This extended data set was then used to fit the ellipse for the Heydemann demodulation. After obtaining the fitted ellipse parameters, the photoacoustic measurement was started, and multiple acquisitions of the photoacoustic signal were captured, resulting in N acquisitions of the I and Q signals. In Phase 3, each acquisition was first demodulated with the Heydemann method using the ellipse parameters obtained in Phase 1, before averaging and saving the demodulated displacement. Knowing the sampling rate, the velocity of the target's surface could be estimated from the displacement data.

4.4.2 Results

With the measurement procedure, explained in the previous section, the following data was collected.

Fig. 4.11 shows the data and ellipse fit before the photoacoustic measurement, as described in Phase 1 of 4.10. This figure shows that the original IQ data constitute an ellipse with a DC offset. The red line in this figure shows the fitted ellipse. The fitted ellipse accurately describes the recorded IQ data, such that accurate demodulation is ensured later.

Photoacoustic data was recorded using the SPL laser diode and the phantom, aligned as depicted in Fig. 4.5c, with a 1% ink concentration acting as the absorber. After demodulation and averaging of the photoacoustic signal, the signals were digitally low-pass filtered with a cutoff frequency of 5 MHz. The displacement and velocity can then be plotted as shown in Fig. 4.12. Here, time $t = 0$ indicates the firing of the excitation source, and at this time, a spurious velocity signal is detected due to optical and/or electronic interference of the detection system with the excitation. After around 7.5 μs after the firing of the excitation diode, a short pulse-like signal originating from the absorber is recorded. This 7.5 μs delay matches the expected travel time for an acoustic signal originating approximately 7.5 mm from the detection point, given the speed of sound in PDMS is 1000 m/s. This correlation

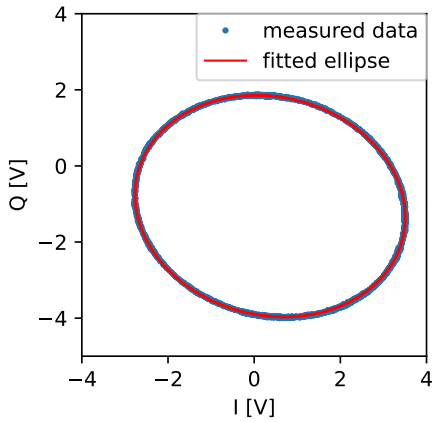

Figure 4.11: Measured IQ data for a large vibration (blue) and a fitted ellipse (red), which will we used to accurately demodulate later.

confirms that the signal originates from the absorber. This recorded displacement has an amplitude smaller than 0.5 nm and a surface velocity spike around 1 mm/s.

An even smaller secondary signal around 12.5 μs can also be seen. This signal, as will be verified later, originates from the photoacoustic signal's reflection from the phantom's excitation side.

4.5 Photoacoustic imaging

4.5.1 Single channel

In order to perform photoacoustic imaging, the signal must be detected at multiple locations. We employed 1D scanning of the LDV beam on the phantom's surface, perpendicular to the absorbing channel. The scan covered a length of 1 cm with steps of 125 µm. A photoacoustic signal was detected at each step, similar to the previous section. Now, the alignment before the measurement was done similarly as for the single point measurement explained in Section 4.4. Fig. 4.13b shows a top-view schematic of the setup. Again, the fast-axis of the laser diode was placed in the transverse plane to the ink channel, in the same plane as the LDV line scan locations. The lower divergence of the slow-axis ensures less excitation out of this plane. The ellipse fitting was done before scanning for the measurements in this section.

The step spacing of 125 µm is smaller than half the expected cutoff acoustic

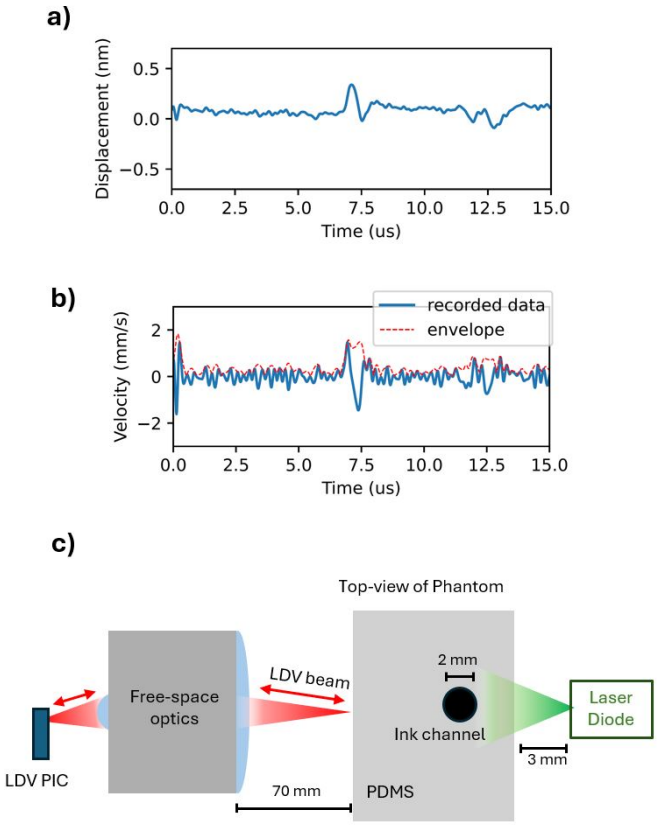

Figure 4.12: The displacement a) and velocity b) signal after averaging and filtering of photoacoustic signals recorded with the on-chip LDV and generated by the SPL laser diode in the phantom from Fig. 4.5c . c) Shematic (not to scale) of the setup to measure the photoacoustic singals. The LDV PIC and free space optics remotly detect surface vibrations of the PDMS phantom. On the right side, the excitation source directed towards the phantom in which the ink-filled tube (top-view) acts as the absorber.

wavelength determined by the detection bandwidth.

The surface velocity time traces, recorded at the different locations along the scanning axis are plotted in Fig. 4.13. It shows a clear relation between the measurement location and the time of arrival of the photoacoustic signal. The first signal arrives at approximately 7.5 μs for the central measurement locations (=5 mm) and up to 10 μs for the edge measurement locations (0 or 10 mm).

As with the single point result from Fig. 4.12, a second feature is present. This feature is more prominent at the edge measurement locations and shows a reverse polarity compared to the first signal. This polarity change can be explained by acoustic theory, specifically the reflection characteristics of a soft boundary. This further supports the idea that the second feature originates from the reflection of the surface at the excitation side of the phantom. The central measurement locations exhibit a 'doubling' effect. To understand these effects in more detail, a simple 2D acoustic simulation of the scalar wave equation was performed in COMSOL with the initial pressure distribution depicted in Fig. 4.14a. In this simulation, we assumed an acoustic impedance of the PDMS of 1.02 MRayl and an acoustic impedance of the absorber of 1.5 MRayl (same as water). After propagation for around 5 μs, Fig. 4.14b shows that the primary signal is nearly reaching the detection surface (left), while the secondary signal appears due to reflection from the backside. The reflected pressure wave shows a uniform wavefront, and no doubling effect of the reflected signal is observed. At 9 µs, however, the shape of the reflected signal's wavefront after passing by the channel, as seen in Fig. 4.14c, shows a doubling effect. The first contribution of this reflected wave is the signal passing through the channel with a higher speed of sound, while the second contribution is the diffracted signal going 'around' the channel, contributing to the distorted wavefront.

The data from figure 4.13 can be used to create a 2D photoacoustic reconstruction. We used a 2D time-reversal algorithm, as discussed in Chapter 2, to reconstruct the image, implemented with the MATLAB package k-wave [70]. The algorithm uses the measured forward-propagation field to generate back-propagation fields, after which a Hilbert transform is applied to reconstruct initial pressures at time = 0 [39]. The Hilbert transform of the signal calculates the envelope as shown in Fig. 4.12b and can be used for imaging or defining the amplitude of the signal. For the image reconstruction, we used a reported speed of sound in PDMS of 1020 m/s [68, 69]. From figure 4.15, it is clear that the reconstructed image shows a signal originating from the same location as the channel. Although reconstruction data for depths larger than the thickness of the phantom could be omitted, we show that a mirror image appears due to the reflection from the excitation side of the phantom.

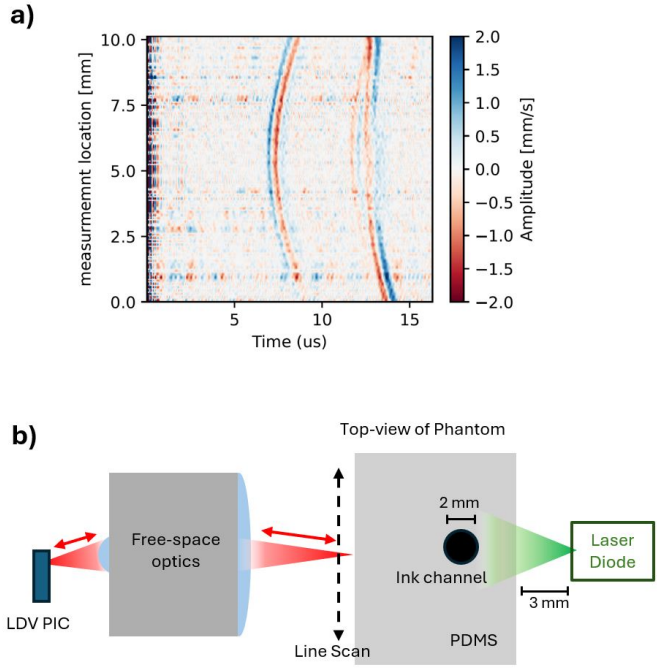

Figure 4.13: a) Velocity recorded for different measurement locations along a line on the surface, transverse to the channel direction, from which photoacoustic signals originate as indicated with the schematic of the setup in b)

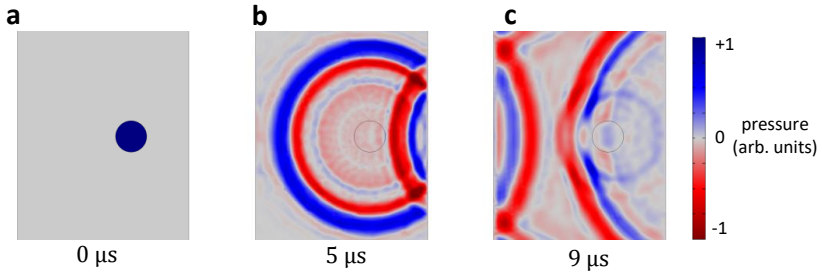

Figure 4.14: 2D COMSOL simulation of acoustic propagation in a geometry similar to Fig. 4.5 c for an initial pressure distribution with increased pressure inside the tube filled with a water-based solution surrounded by PDMS at a) $t = 0\ \mu s$, b) $t = 5\ \mu s$ and c) $t = 9\ \mu s$

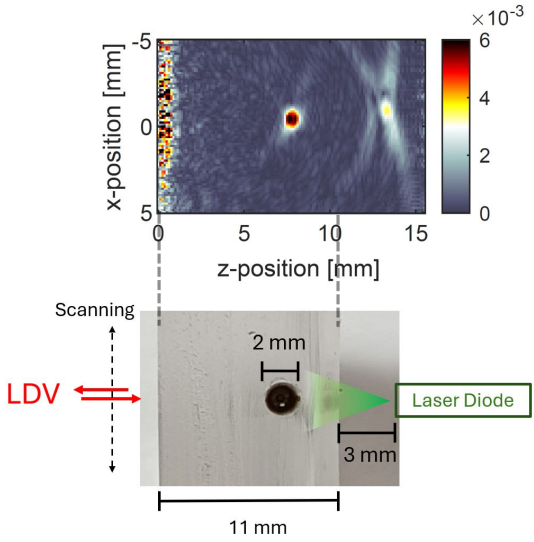

Figure 4.15: (Top) Image reconstruction of the phantom. (Bottom) Picture of the cross-sectional view of the PDMS-based phantom with the ink-filled channel.

4.5.2 Different Absorber Depths

Accurate reconstruction of the photoacoustic signal origin was further verified with multiple experiments at different depths as demonstrated in Fig. 4.16. Here, we imaged channels at three different depths of 9.6 mm, 7 mm and 5.8 mm relative to the LDV side of the phantom. The first feature's arrival time is later for larger depths from the detection side. In contrast, as expected due to the shorter traveling distance, the reflected signal arrives earlier for absorbers at larger depths. The amplitude of the signal changed between different measurements for absorbers at different depths; this could be because, for each different depth of the channel, the phantom was changed such that the alignment of the laser diode and LDV could be different. As we will see in the later discussion, the amplitude is influenced heavily by the illumination profile and acoustic propagation length, so a slight change in alignment can give different amplitudes.

4.5.3 Different Absorber Concentrations

In the experiments and images of Fig. 4.15 and Fig. 4.16, an ink concentration of 1% was used to act as the absorber. According to the absorption spectrum described in Fig. 4.7, this concentration would give rise to high absorption values up to $120\ \mathrm{cm}^{-1}$, far above typical blood absorption values at 900 nm. In order to study

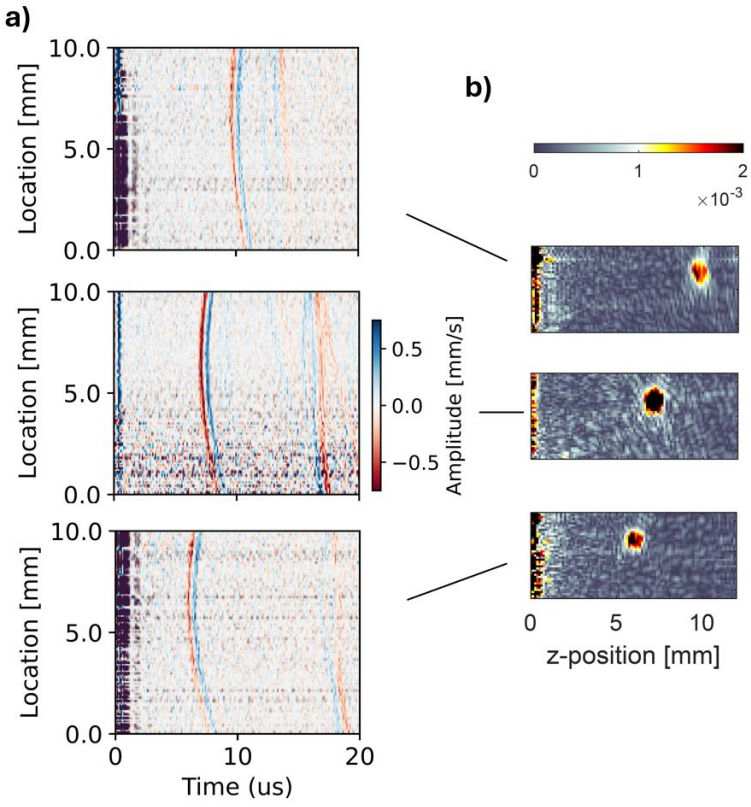

Figure 4.16: Scanning data a) and photoacoustic reconstructions b) for phantoms with absorbers at different depths of 9.6 mm, 7 mm and 5.8 mm from the detection side of the phantom.

how the photoacoustic detection of absorbers with lower ink concentration behave, the concentration of the ink-water solution was changed for different measurements on the same phantom. For this measurement, no realignment was necessary; only the ink in the channel was replaced. Fig. 4.17a shows that the amplitude increases for higher ink concentration, a small signal can be detected at 0.01% which agrees with around $1.2\ \mathrm{cm}^{-1}$. Fig. 4.17b shows photoacoustic images at different ink concentrations. For lower ink concentrations, the photoacoustic images have a lower contrast. In these figures, the contrast ratio was kept the same. Lowering the scaling could further visually improve the images at lower concentrations.

Fig. 4.17c shows the increasing Signal-to-Noise Ratio (SNR) for higher ink concentration. The SNR is defined by taking the maximum velocity of the pulse after the Hilbert transform divided by the Root Mean Square Error (RMSE) error. Unlike the PDMS phantom, in vivo samples generally exhibit optical scattering and absorption, affecting illumination, imaging strength, and depth. A more in-depth discussion on if and how we can detect absorbers for in vivo samples is discussed in the following section. Since the measured signals for absorption coefficients within the physiological range at 905 nm ($2 - 10\ \mathrm{cm}^{-1}$) [41] show only a limited strength, a higher excitation power might be necessary for in vivo demonstrations.

4.5.4 Two channels

While previous results provide a 2D photoacoustic image with one absorber, imaging of more absorbers is possible. Here, we show the imaging of a phantom with two absorbers (channels filled with 1% ink). However, more complex structures should also be feasible. Fig.4.18b shows the reconstruction and cross-section geometry of the phantom. Because the absorbers are spaced around 6 mm apart, the laser diode was placed further from the phantom to ensure illumination of both phantoms. Now, due to the divergence of the diode (as will be discussed in more detail in the Section 4.6), both channels are illuminated but with reduced fluence values, hereby limiting the signal strength, as can be seen from the reconstruction and the collected scan data. The reconstructed shapes for both channels in the image do not look spherical, which could be due to the non-uniform illumination pattern.

4.5.5 Laserbar excitation

Creating the image with the two-channel absorbers using the laser diode as the excitation source was not trivial due to difficult alignment. Trial and error was used to determine the spacing between the diode and the phantom while trying different yaw-alignments of the diode to end up with the image in Fig. 4.18.

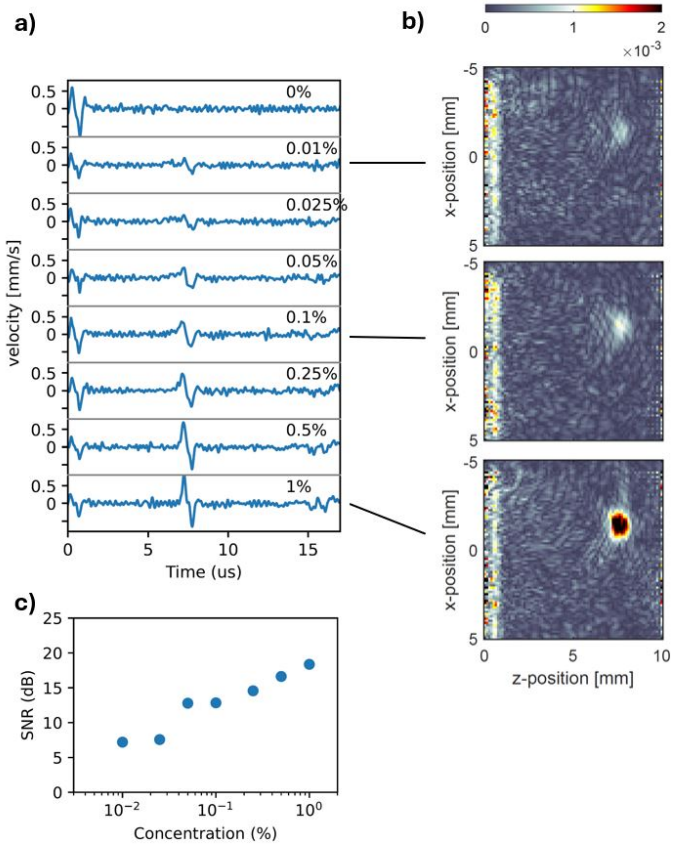

Figure 4.17: a) Signal time traces of the recorded velocity of the surface after photoacoustic excitation for different ink concentrations inside the phantom. Increasing the concentrations results in stronger signals. The 0.1 % ink solution was measured to have an absorption of 12.5 cm^{-1} *at a 905 nm wavelength. b, c, d) Show image reconstructions for different ink concentrations showing reduced contrast for lower concentrations. e) SNR for the different concentrations.*

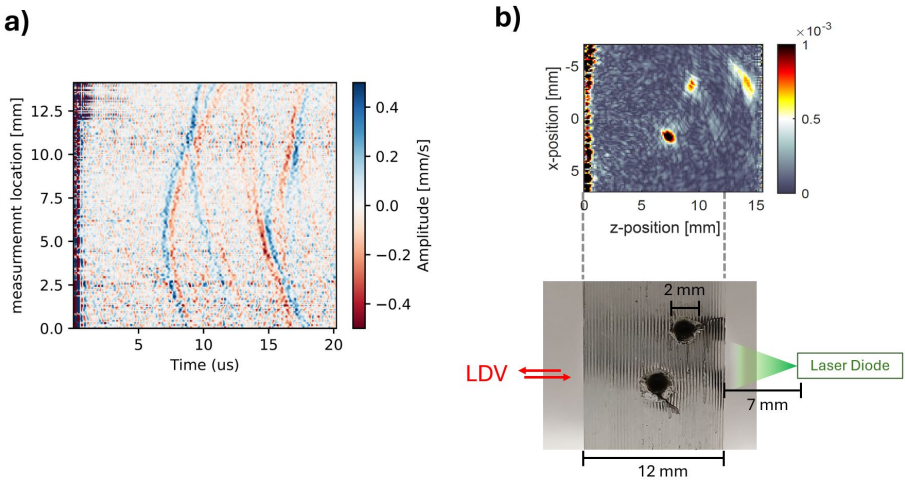

Figure 4.18: a) Scanning data and b) reconstructed image (top) of a phantom with two absorbing channels (bottom). Photoacoustic signals are generated with the SPL laser diode

For the results presented in Fig. 4.19, we have used a laserbar as the excitation source. The laserbar was positioned similarly to the laser diode, now 2 mm from the surface of the phantom. However, now, the laserbars long axis was placed along the LDV scanning direction, making for a wide illumination pattern as indicated in Fig. 4.19b. As will be discussed in more depth in the discussion section, its longitudinal illumination pattern makes the alignment of the excitation source very easy and creates a uniform illumination pattern, suitable for photoacoustic imaging.

4.6 Discussion

The previous sections demonstrated contactless 2D photoacoustic imaging capabilities for simple geometries on PDMS-based phantoms. Although these results are relevant as a first demonstration, it is unclear how to interpret them when considering in vivo experiments. In this section, we compare the laserbar and diode illumination pattern and examine the influence of the optical properties of in vivo samples.

First, we propose a method to roughly estimate the resulting pressure levels. After verifying the estimated pressure values against the PDMS-based measurements with the laser diode, we extend this method to assess the performance of the system. Additionally, we discuss the limitations of the lab demonstration and

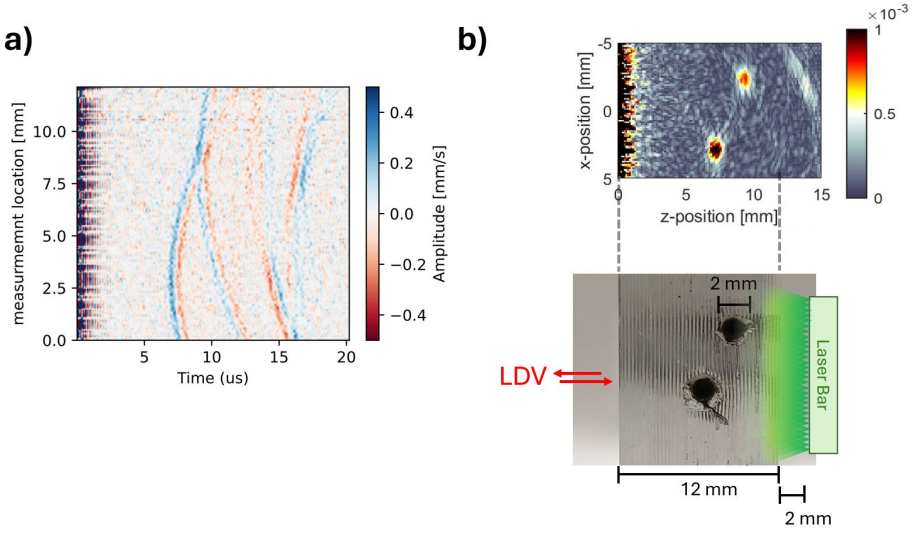

Figure 4.19: a) Scanning data and b) reconstructed image (top) of a phantom with two absorbing channels (bottom). Photoacoustic signals are generated with the laserbar

outline potential solutions, which will be elaborated on in the next chapter.

4.6.1 Illumination Patterns

The initial pressure distribution is determined by the spatial overlap of the fluence and the absorption profile. Fig. 4.20a and Fig. 4.20b show the illumination profile of the SPL laser diode package in different directions the position of the ink channel for the single channel phantom is indicated for both figures. Fig. 4.20a shows the imaging plane, transverse to the ink channel while Fig. 4.20b shows the perpendicular plane along the ink channel. Fig. 4.20c and d show the illumination profile for the laserbar in the same planes as a and b. These figures are expressed in terms of the expected fluence in $\mathrm{mJ/cm^2}$ for pulse lengths of 500 ns operating at peak optical power (approximately 500 W for both).

These illumination profiles were simulated using a Monte Carlo simulation with the MATLAB package MCMatlab [71]. This simulation method was used because it can also calculate the illumination profile in highly scattering media such as tissue. While for PDMS-based phantoms, scattering effects can be neglected, simulations for in vivo samples, as presented in the following discussion in this section, do require a simulation method that can simulate scattering effects.

Comparing Fig.4.20a and Fig. 4.20c, it is clear that the laserbar presents a more

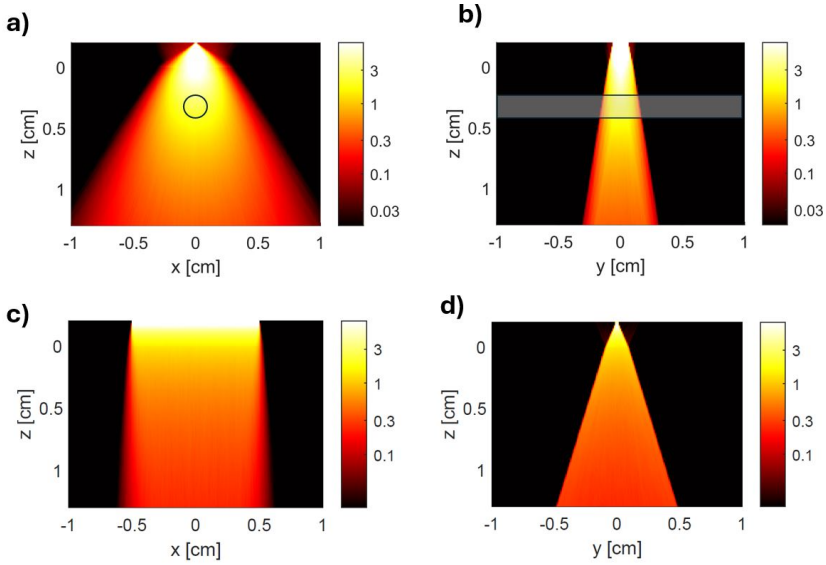

Figure 4.20: Fluence profiles in mJ/cm^2 for the SPL laser diode package in a) the zx-plane, transverse to the ink channel and b) the zy-plane. The location of the ink channel is indicated in the figure. The fluence profiles for the laserbar in the same planes are presented in c,d). Both sources are placed 2 mm from the surface of the PDMS phantom (top of the figure). Pulses with a peak optical power of 500 W and 500 ns were considered.

uniform illumination pattern in the z-x plane compared to the laser diode, which eases the alignment, especially for the dual channel images. On the other hand, the laser diode presents larger fluence values in the phantom due to its higher peak power in the current setup and the smaller size of the diode.

4.6.2 Signal Strength and Field of View

The illumination pattern can be used to estimate initial pressure values. Here, we first focus on the situation as depicted in Fig. 4.15, where the laser diode is used for photoacoustic imaging of a phantom with a single channel. The location of the absorbing channel for the phantom used in Fig. 4.15 is indicated in Fig. 4.20a and b. If we consider the fluence at the center of the absorber ($= 2.5\ \mathrm{mJ/cm^2}$) and an ink concentration of $0.1\ \mathrm{cm^{-1}} \rightarrow \mu_a = 12.5\ \mathrm{cm^{-1}}$, a rough estimation of the initial pressure can be calculated by using Eq. 4.2 and 4.1 and gives an initial pressure of around $6\ \mathrm{kPa}$.

If we want to estimate the pressure levels, that can be measured at the surface, it is important to take into account the propagation and divergence losses. These

will largely depend on the total 3D pressure distribution, resulting from the spatial overlap between the fluence profile and the absorption profile.

In the xz-plane normal to the channel, it can be seen that there is an almost uniform illumination profile of the channel cross-section. Considering the illumination in the yz-plane parallel to the channel, Fig. 4.20b shows that, due to the divergence angle of the diode, a length of 2-3 mm is illuminated by the ink channel. The total volumetric area with an increased initial pressure is therefore a tube with a 2 mm diameter and a length of around 2-3 mm. While an acoustic simulation is required for exactly knowing the influence from acoustic propagation and divergence to the pressure levels at surface, analytical expressions exist for spherical absorbers.

A rough estimation of the $2-3\ \mathrm{mm}$ long tube with a diameter of 2 mm is a spherical absorber with a 2 mm diameter. In the analysis in the remainder of this section, we consider spherical absorbers with a 2 mm diameter, for which we estimate the signal strengths and the field of view.

For a spherical initial pressure profile with radius R_s and initial pressure p_0, the pressure at a distance z from the absorber can be estimated as [72]

$$p_{peak}(z) = p_0 \frac{R_s}{2z}. \tag{4.3}$$

The LDV measured the surface opposite to the laser diode side. This surface was at a distance of around 7.5 mm away from the absorber, as indicated in Fig. 4.15. Using equation 4.3, with an initial pressure of 6 kPa and a distance of 7.5 mm, the pressure arriving at the surface can be estimated as $6\ \mathrm{kPa}/(2 \cdot 7.5) = 400\ \mathrm{Pa}$. This is equivalent to a peak velocity of around $800\ \mu\mathrm{m/s}$ in a 1 MRayl media according to $p = Z/2 \cdot v$. Although this is a rough estimation, the measured peak velocity value for 0.1% ink in Fig. 4.12 was around $400\ \mu\mathrm{m/s}$, just a factor 2 away from the estimated value.

To get an idea of the expected Field of View (FOV), we can calculate for which locations a 2 mm-diameter spherical absorber is detectable. Fig. 4.21 shows the resulting pressure at the bottom (LDV side), originating from a 2 mm-diameter absorber with its center indicated at the location on the figure. Fig. 4.21a shows the results for the laser diode excitation at 2 mm above a PDMS phantom, while Fig. 4.21b shows the results for the laserbar. The higher amplitudes observed at the surfaces in Fig. 4.21a indicate that the pressure amplitude at the surface depends on both the fluence and the distance traveled. While absorbers near the laser diode receive higher optical energy, those near the LDV surface experience reduced acoustic divergence losses.

The dotted line indicates the region where the resulting pressure is equal to the

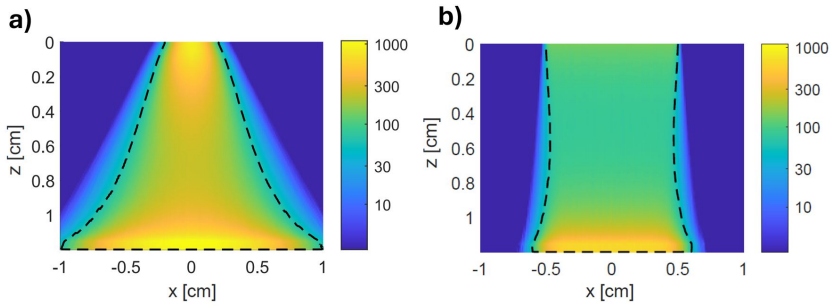

Figure 4.21: Estimated pressure amplitudes [Pa], arriving at the LDV detection surface for spherical 2 mm-diameter absorbers at different locations in the PDMS phantom with the excitation source a) being the laser diode and b) the laserbar, on the opposite side of the LDV. The dotted line indicates values equal to the NEP for the detection system, lowered through 1 s averaging.

NEP, with 1s averaging. Assuming 2 kPa as the total NEP, averaging for 1 second at a repetition rate of 1 kHz results in a final NEP of 63 Pa. Fig. 4.21 shows again differences for the laserbar and diode in terms of pressure levels, uniformity and, a broader FOV for the laserbar.

In reality, excitation and detection would most often happen on the same side, which changes the traveled distance of the pressure wave. Figs. 4.22 a,c shows estimates similar as Fig. 4.21, but now resulting from same-side excitation and detection under laser diode and laserbar illumination for PDMS-based phantoms (a,c). Fig. 4.21b and d show the results in media with typical tissue-like optical properties: $\mu_a = 0.5\ \mathrm{cm}^{-1}$ and $\mu_s' = 10\ \mathrm{cm}^{-1}$ [64, 66].

First of all, Fig. 4.21a,c shows that for PDMS-based phantoms, we expect to detect absorbers up to a depth of 1 cm using the laser diode and around 7 mm with the laserbar. In tissue-like media, (Fig. 4.21b,d,) this is reduced to around 4-5 mm for both sources.

It should be noted that these estimates will largely depend on the NEP and that, in reality, the NEP of the LDV could be compromised due to non-ideal reflection from the surface of an in-vivo sample.

Nevertheless, differences between the laser diode and laserbar can be observed. While the peak pressure at a certain depth is usually higher for the laser diode, it shows more variation of the fluence along the lateral axis (locations with the same depth). On the other hand causes the longer shape of the laserbar a shallower but broader FOV, with a more uniform fluence for absorbers at the same depth, as long as they are beneath the laserbar.

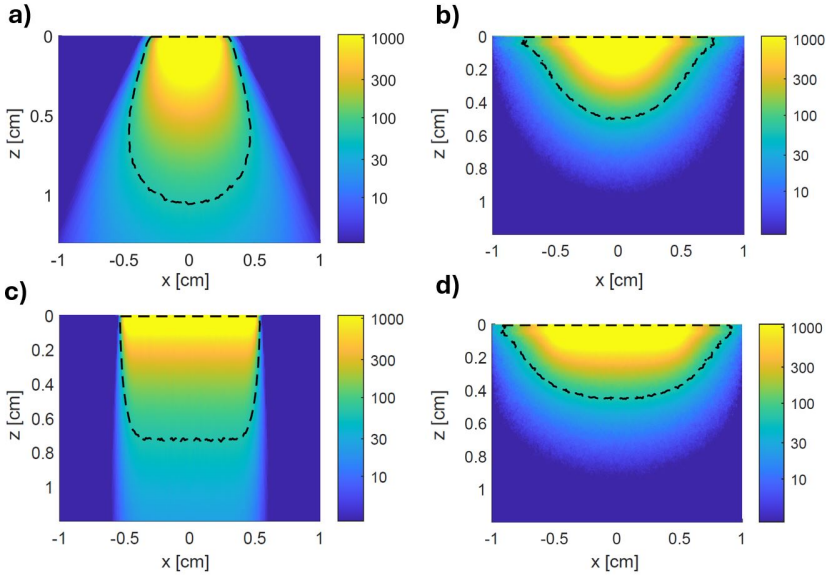

Figure 4.22: Estimated pressure amplitudes [Pa], for same-side detection and excitation, arriving at the surface for spherical 2 mm diameter absorbers at different locations. a) Laser diode and c) laser bar in PDMS phantom. b) Laser diode and d) laser bar in a tissue-like sample, with $\mu_a = 0.5\ cm^{-1}$ and a $\mu_s' = 10\ cm^{-1}$.

Note that, using an array of laserbars could improve the total fluence and the uniformity in the direction parallel to the laserbar. These estimations, along with the demonstration in Section 4.5.5, show that laserbars could be a well-suited source for building a miniature photoacoustic imaging system.

4.6.3 2D Imaging characteristics

In order to create the images, the LDV beam was scanned along a line on the surface of the sample in steps of 125 μm over a distance of around 1-1.2 cm. This results in around 80-100 locations where a photoacoustic measurement was performed. For each location, around 1 s of data was recorded, giving a theoretical measurement time of around 80 seconds. In reality, however, the entire measurement took around 8 minutes, due to an inefficient data pipeline. The transmitted recorded data was first demodulated and saved on a hard drive before starting the next recording. Parallelizing these processes and upgrading the storage and demodulation hardware should strongly decrease this time towards the theoretical measurement time. Still, the theoretical imaging time of 80 s is too long for practical situations because any sample movements during measurement will influence imaging quality. Moreover, the measurement time will skyrocket when moving towards 3D photoacoustic imaging, which requires scanning in 2D over the sample surface. Multibeam LDV could reduce this reliance on scanning and, therefore, reduce the measurement time.

To limit the measurement time in our demonstration, we were confined to 2D imaging. In conventional 2D AR-PAM systems, focused ultrasound transducers collect signals in the 2D plane underneath the contact-based transducer [73]. In contrast to focused ultrasound detectors, LDV-based detection collects signals from all directions. As such, instead of collecting signals originating from the plane underneath the array, an LDV array also collects any photoacoustic signals generated through out-of-plane excitation. Consider the situation as drawn in Fig. 4.23. The LDV is scanned over a line along the surface of the phantom. Now, the plane that is perpendicular to the phantom's surface and contains the detection line is considered as the imaging plane. Targets within the imaging plane are accurately reconstructed by a 2D reconstruction algorithm. However, due to the divergence of the excitation source out-of the imaging plane, absorbers there (e.g. at point $P_1 : x_1, y_1, z_1$), generate signals that are captured by the LDV. This results in an excited absorber at P_1 causing a shadow image in the reconstruction attributed to $P_0 : x_0, y_0, z_0$, the intersection point of the circle around the detection line through P_1. Note that for a 3D imaging situation, where the LDV is scanned along a 3D grid, this out-of-plane excitation effect is not present.

However, in the analysis that follows, we show that, due to the illumination profile

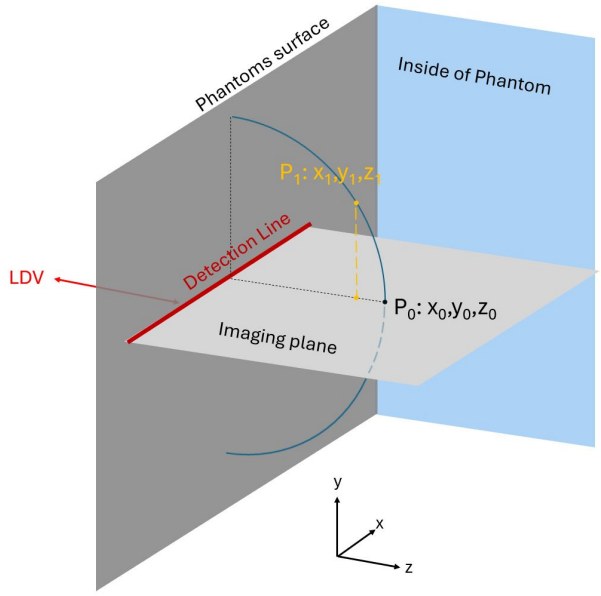

Figure 4.23: Schematic of an out-of-plane excited absorber at x_1, y_1, z_1, which will be attributed to x_0, z_0 in the imaging plane underneath the LDV detection line, creating a shadow object in the reconstructed image and a possible source of resolution degradation

and simplified geometry of the 2D demonstration in this chapter, the influence of the out-of-plane excitation on the resolution degradation remains limited.

First, consider the bandwidth-limited resolution of the 3.5 MHz LDV-based detection bandwidth. Assuming an impedance of 1.02 MRayl, the theoretically estimated resolution of a photoacoustic image is limited to $0.8\lambda_c \approx 287\ \mu\mathrm{m}$, with λ_c being the acoustic wavelength for the cutoff frequency [1, 40].

Now, consider the resolution degradation due to out-of-plane excitation for a structure that is invariant normal to the imaging plane (like the phantoms used in the measurements). Figure. 4.23 shows the situation where an LDV array/scan collects photoacoustic signals in a line on the phantom's surface. Now, an out-of-plane excited signal at $P_1 : x_1, y_1, z_1$ will create a shadow image in the reconstruction attributed to $P_0 : x_0, y_0, z_0$, the intersection point of the circle around the detection line through P_1.

Considering a y-invariant phantom geometry (similar to the demonstrations), the degradation can be estimated by calculating the difference between the attributed signal origin point in the 2D plane (x_0, z_0) in the imaging plane and the actual values x_1, z_1. In theory, all signals originating from a location on a circle running

through x_0, z_0 around the measurement axis will be attributed by the imaging algorithm to the x_0, z_0 location. However, due to the illumination profile in the non-scattering PDMS, signals only originate within the divergence angle of the SPL laser diode (for free space, a divergence angle of $10\,\mathrm{deg}$). Assume x_0, z_1, y_1 is just within the out-of-plane divergence angle α and on the circle, then the maximal deviation of the attributed x, y in the imaging plane compared to the real x_1, y_1 is around $z_0 \cdot (1 - cos(\alpha))$. A divergence angle of $10\,\mathrm{deg}$ and an imaging depth of 1 cm leads to an estimated degradation of around $150\ \mu\mathrm{m}$, which is still below the theoretical resolution limit as calculated. Suppose the structure is, however, not invariant along the normal of the imaging plane. In that case, out-of-plane excitation can project 'shadows' all along the circle on the image, thereby showing absorbers way out of the imaging plane. It is important to consider that this limited degradation does not hold when the phantom is scattering because the excitation source is scattered outside of the typical divergence angle. Then, 2D LDV scanning should be considered to omit the out-of-plane excitation degradation.

4.6.4 Challenges towards in-vivo samples

The results from the setup show the possibility of non-contact photoacoustic detection with silicon-photonics-based LDV. However, multiple challenges are expected when moving from a lab demo on a homemade phantom to an in-vivo demonstrator. Here, we will briefly mention these challenges.

As seen in chapter 3, ensuring a good collection efficiency of the LDV is very important to achieve low noise equivalent pressures. While the lab demonstration in this chapter captured specular reflection from the flat PDMS-based surface, in-vivo samples pose many challenges due to their organic structure. First of all, surfaces such as skin are uneven and highly scattering, which makes the collection of specular reflection impossible, and the collection of light relies on capturing diffuse reflected light. As mentioned in chapter 3, high NA optical systems could ensure high optical collection from diffuse reflective surfaces but it limits the depth of focus. Using these optics to measure uneven samples would require some automatic focusing capabilities.

Secondly, while in the proposed lab demonstration the excitation and detection of photoacoustic signals happen at the opposite sides of the phantom, most applications require same-side excitation and detection. In the demonstration, opposite excitation allowed for easier alignment and less complexity. Luckily, the contactless nature of LDV eases efficient excitation light delivery underneath the detection points. It might however require more free-space optical elements such as dichroic

mirrors and lenses.

Thirdly, in this lab demonstration, an LDV was scanned along a line on the surface to enable 2D imaging. As explained in the previous section, due to the nature of LDVs, out-of-plane excitation degrades the reliability of the 2D image. More out-of-plane signals would be excited for highly scattering samples, making a 1D scanning system unreliable. Adding detector element rows in the other dimension, approaching a 2D detector array configuration, could compensate for these effects, but it requires more elements. As explained in chapter 3, scaling the number of LDV beams to 100 is challenging. In the next chapter, we will propose a new architecture to enable scaling towards hundreds of beams, which could enable 3D photoacoustic imaging without the need for scanning LDV beams.

4.7 Closing remarks

This chapter introduced a lab demonstration of non-contact photoacoustic imaging using a silicon photonics-based LDV system and a miniature excitation source. Efforts necessary for this demonstration included choosing and designing for a suitable bandwidth, developing phantoms to validate imaging capabilities, and ensuring a flat and specularly reflective surface to ensure good signal quality and a compact pulsed excitation source.

The results show the potential of silicon photonics-based LDVs for contactless photoacoustic imaging, though several challenges remain in moving toward a compact, contactless, practical in-vivo imager. One of these challenges is omitting the need for scanning to reduce the imaging time. The most evident approach is to increase the number of beams. This is, however, non-trivial, and the next chapter explains the problem of scaling the number of beams and proposes an alternative architecture to solve this problem.

5

Scalable Architecture for Multibeam Silicon Photonics-based Laser Doppler Vibrometers

5.1 Introduction

Photoacoustic imaging requires the detection of the signal on multiple locations along the sample surface. Conventional contact-based ultrasound detectors often use an array of hundreds or thousands of US transducer elements for the multi-site detection [5].

For LDV-systems, multi-site detection can be realized by either scanning and/or using multibeam detection systems. Existing LDV implementations are however limited to accommodating only a couple of detection beams and generally rely on scanning. The need for scanning increases the image acquisition time and often requires a complex scanning system which is often bulky and expensive. Moreover, scaling free-space or fiber-based LDVs to multiple beams increases cost and size rapidly due to the scaling of the number of discrete components. While silicon photonics based LDVs seem to provide better scaling towards multiple beams by relieving the need for discrete components, scaling to more than a handful of beams remains challenging due to electrical connection and packaging challenges.

In section 5.2, the scaling challenges are discussed in more depth and we propose a novel, scalable architecture. This scalable architecture uses a novel component called the multibeam frequency shifter, which will be discussed in depth in the following sections. Section 5.3, describes the theory and fundamental working principles of this component, while section 5.4 and 5.5 focus on the design considerations and simulation of this component. These simulated results introduce this novel component and could allow for the implementation of the scalable architecture as discussed in 5.2.

5.2 Scaling problem and proposal of a scalable architecture

Fig. 5.1a depicts a conventional homodyne LDV architecture. It can be seen that 5 electrical connections are used to carry a ground plus 4 photocurrent signals out of the chip. It can be noted that using balanced detection, this could be reduced to 3 electrical connections. Using the conventional multibeam architecture for homodyne LDVs, as depicted in Fig. 5.1b, the number of electrical pads scales linearly with the number of beams and the total necessary connections can be estimated by multiplying the number of pads per beam times number of beams, as plotted in Fig. 5.3b. A homodyne LDV architecture with around 100 sensing beams would need around 200 to 400 electrical connections to the chip, which approaches the limits of wirebonding and could necessitate other complex packaging techniques.

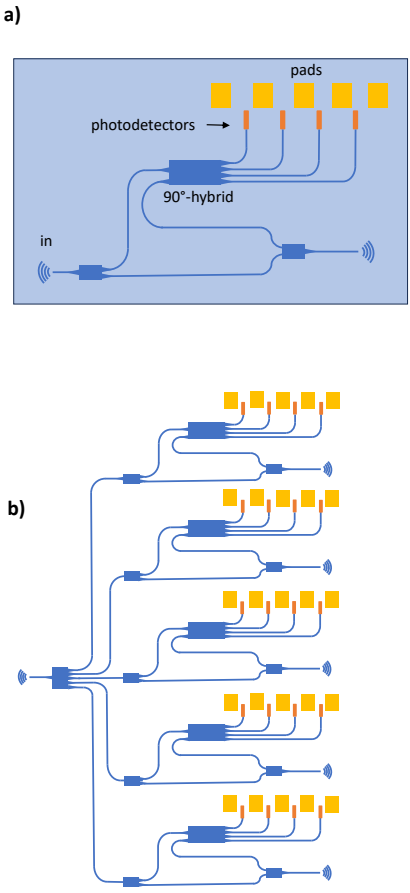

Figure 5.1: a) Single beam on-chip LDV layout. b) Conventional layout for multibeam on-chip LDVs

Given these challenges, it is clear that this scaling approach is not sustainable. Therefore, we propose an alternative architecture.

For free-space LDVs, synthetic-array heterodyne detection has been demonstrated to reduce the number of photodiodes and electrical connections required in multibeam LDV systems [74, 75]. In this technique, each sensing beam is frequency-shifted to a different carrier with an Acousto-Optic Modulator (AOM). After reflection from the probed object, these probe beams are combined with the local oscillator on a photodetector. There, the sensing signals and carrier frequency are transferred to the electrical domain, where each sensing beam can be distinguished by having a different carrier frequency. These multiplexed electrical signals can be amplified

and recorded by the same circuit. Moreover, this technique could also help in reducing crosstalk between different sensing beams thanks to the separation in the frequency domain.

Here, we propose a similar on-chip architecture and introduce a novel component with a similar function as the AOM in synthetic heterodyne detection: 'the multibeam frequency shifter'. This component takes a single frequency input and produces multiple outputs into waveguides, with each output exhibiting a different frequency shift relative to the input light, determined by the component's internal mechanism. Although the specifics of this process will be explained later in the chapter, for now, you can think of it as a black box.

Fig. 5.2a illustrates a proposed 5-beam LDV layout. The input light is first split into a reference arm and a measurement arm. The light in the measurement arm is then split into 5 arms by the multibeam frequency shifter, with each arm carrying light that has been shifted to a different optical frequency relative to the original input, as shown in the figure. These frequency-shifted outputs are routed to different output grating couplers, such that they can probe different locations on the target, enabling the system to probe multiple points simultaneously. After reflection from the target, Fig. 5.2b shows that the measured vibration information is contained around equidistant frequency-shifted optical carriers with ω_0 the original frequency and Ω, the spacing between them.

When these measurement beams are combined on PDs with a frequency shifted reference, with a frequency shift of -2.5Ω (in green), the photocurrent signals are separated in the electrical frequency domain which allows for multiplexed readout of the PDs, necessitating only a couple of signal pads for 5 beams. Note, however, that the frequency shifters require multiple pads for driving signals, but these could be shared with other units as depicted in figure 5.3a. Figure 5.3b shows that for a large number of beams, the new architecture requires up to an order of magnitude fewer electrical connections.

This new architecture requires a component capable of generating multiple frequency shifts. While free-space circuits have successfully utilized AOMs in the Raman-Nath regime [1], as multibeam frequency shifters [74–77], on-chip acousto-optic multibeam frequency shifters are still notably absent from most commercial SOI platforms. The implementation of such a feature requires the heterogeneous integration and processing of suitable acousto-optic materials [78–81], which con-

[1] The Raman-Nath regime occurs when light interacts with a sound wave in an acousto-optic material under conditions where the acoustic wavelength is relatively large compared to the interaction length, resulting in light being diffracted into multiple orders. This makes it ideal for multibeam applications. In contrast, the Bragg regime is characterized by longer interaction lengths, where light is typically diffracted into a single order. If the interaction length is extended, such that multiple diffraction events occur, the diffraction pattern can shift from the the Raman-Nath regime to the the Bragg regime.

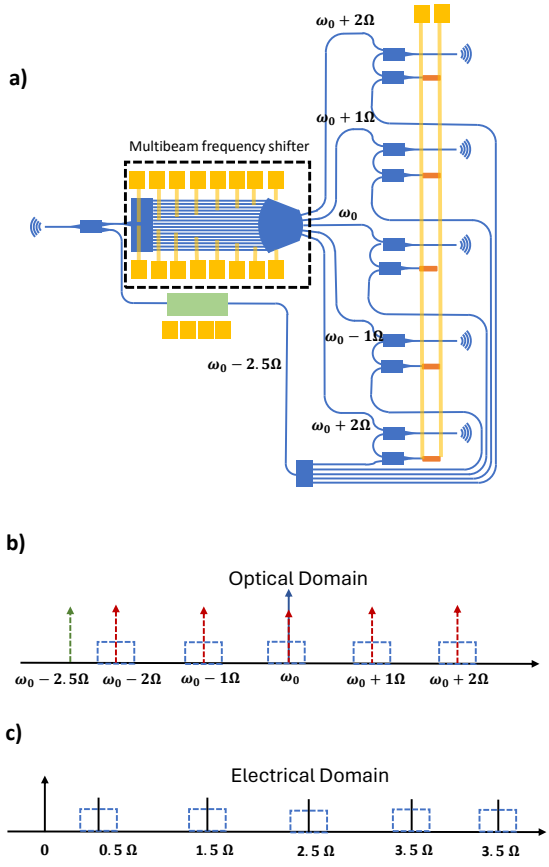

Figure 5.2: a) New architecture for a 5-beam LDV, using a multibeam frequency shifter and sharing pads for signal readout. b) A figure of the frequency content in the optical domain of both the reference and the signal beams. c) In the electrical domain, signals of the different beams are in different baseband frequency bands

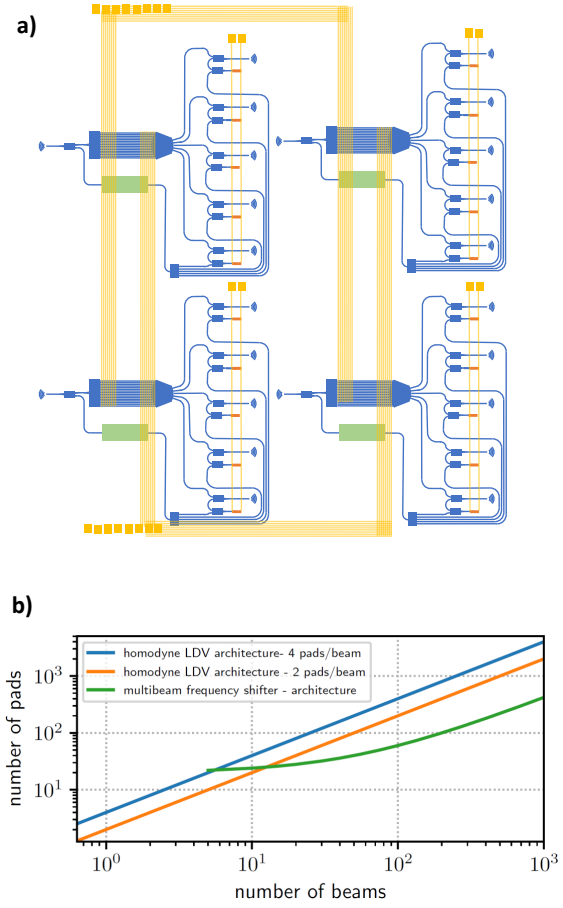

Figure 5.3: a) A schematic showing how a 16×5 *multibeam frequency shifter LDV could be used to create multibeam LDVs with more beams, while keeping the electrical pads limited due to the sharing of frequency shifter electrical pads. b) Numerical estimation of the number of pads for different numbers of beams for the different architectures.*

sequently increases complexity and cost. The remainder of this chapter proposes and describes the working principle of a novel multibeam frequency shifter, which leverages existing modulators from commercial platforms to enable

5.3 Multibeam frequency shifter - Theoretical Framework

The remainder of this chapter proposes and describes the working principle of a novel multibeam frequency shifter, which leverages existing modulators from commercial platforms for building this component.

In this first section, we begin with a theoretical description of wave-like modulation. Although somewhat abstract, these concepts will be fundamental for understanding the working principle of the component. The other subsections remove abstraction layers such that at the end of this section, it is clear that a discrete modulator array can be leveraged to create different frequency shifts in different directions (imitating an AOM).

5.3.1 Interaction of light with traveling wave-like modulation

In this section, we will discuss the interaction between optical waves and a traveling modulation wave with a short interaction length, similar to an AOM in the Raman Nath diffraction regime [76, 77]. As depicted in Fig. 5.4(a), let us consider a two-dimensional scenario where a monochromatic optical plane wave is expressed in complex notation as $U_i(x,z,t) = A_i \exp(j2\pi f_0 t - j\mathbf{k_0}\mathbf{r})$, with A_i denoting the amplitude, f_0 as the optical frequency, t as time, $\mathbf{r}$ as the position vector, $\mathbf{k_0} = k_{0x}\hat{\mathbf{x}} + k_{0z}\hat{\mathbf{z}}$ as the k-vector of the optical beam, $\hat{\mathbf{x}}$ and $\hat{\mathbf{z}}$ represent the unit vector in the x and z directions, respectively. Here the k-vector fulfills the following relation: $|\mathbf{k_0}| = 2\pi/\lambda$, where λ is the optical wavelength of light in the medium. As shown in Fig. 5.4(a), let us examine an acoustic modulation with a small interaction length L (operating in the Raman-Nath diffraction regime), traveling along the x axis ($z = 0$) and modulating the optical wave through the photo-elastic effect.

Right after the optical modulation, the optical wave can be expressed as $U_m(x,t) = U(x, z = L, t) = M(x,t)U_i(x, z = 0^-, t)$, where $M(x,t)$ is the modulation applied by the acoustic wave. When the traveling acoustic wave maintains a constant velocity v, the modulation can be expressed as a wave-like function $M(x,t) = W(x - vt)$. Considering the Fourier expansion of the modulation

function $W(x)$ in the x direction is given by

$$W(x) = \int_{-\infty}^{+\infty} W^F(k_x) \exp(-jk_x x) dk_x, \tag{5.1}$$

the modulated optical wave can be expressed as an angular decomposition of plane waves through Fourier optics.

$$\begin{aligned} U_m(x,t) &= A_i e^{j2\pi f_0 t} \exp(-j2\pi k_{0x} x) W(x - vt) \\ &= A_i \int_{-\infty}^{+\infty} W^F(k_x) \exp(j2\pi[f_0 - \frac{k_x v}{2\pi}]t) \exp(-j[k_{0x} + k_x]x) dk_x \end{aligned} \tag{5.2}$$

From this equation, it is evident that the modulated optical field is scattered in different directions due to the modulation wave. Assuming the propagation direction of a scattered component is described by $\mathbf{k}' = k'_x\hat{\mathbf{x}} + k'_z\hat{\mathbf{z}}$, the following relations should be fulfilled.

$$\begin{aligned} k'_x &= k_{0x} + k_x \\ |\mathbf{k}| &= 2\pi/\lambda \end{aligned} \tag{5.3}$$

Fig. 5.4(a), depicts the interaction between an optical monochromatic wave and a modulated traveling wave and it shows the scattering in a different direction (in color). As can be seen in Fig. 5.4(b), the relations from Eq. 5.3 hold. In the figure, k'_x is represented by k_1 and the added vector due to modulation (k_x in Eq. 5.3) is represented by k_m. In grey, the scattering into different discrete directions due to a periodic wave-like modulation, similar to an AOM is depicted, which will be explained in a following section (Section 5.3.2).

The phasor corresponding to this component is $A_i W^F(k_x) \exp(j2\pi(f_0 - \frac{k_x v}{2\pi})t)$, showing that, when the modulation wave is propagating in the x direction with a constant speed v, the angular frequency shifts in the x direction k_x and the temporal frequency shifts Δf_t of the scattered light are always correlated through the equation

$$\Delta f_t = -\frac{k_x v}{2\pi}. \tag{5.4}$$

Note that, aside from the requirement for traveling-wave-like modulation, we have not specified whether the modulation is phase or amplitude modulation of the light, as the analysis above applies to both types of modulation and their combinations.

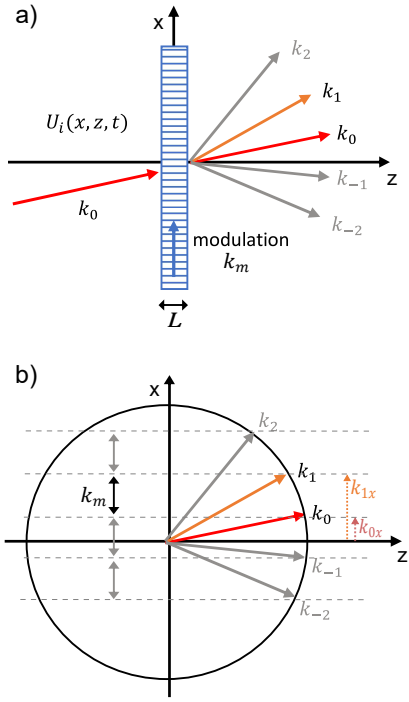

Figure 5.4: a) A 2D propagating optical wave interacting with a wave-like modulation, represented by wave vector k_m, traveling along the x-axis resulting in scattering to a different direction. In grey, the scattering into different discrete directions due to a periodic wave-like modulation, similar to an AOM b) k-vector diagram of the modulated wave vectors

5.3.2 Periodic modulation

Consider the wave-like modulation function $W(x-vt)$ to be periodic, and denote the periodic function as $W_p(x-vt)$. It is possible to define a spatial and temporal period P and T for which,

$$\begin{aligned} W_p(x-vt) &= W_p(x-vt+P) \\ &= W_p(x-v(t+T)) \quad \text{with} \quad T=P/v, \end{aligned} \tag{5.5}$$

Define $a(x)$ to be the single period of $W(x)$

$$a(x) = \begin{cases} W(x), & \text{if } 0 \leq x < P \\ 0, & \text{otherwise} \end{cases} \tag{5.6}$$

Thanks to the periodicity, the Fourier expansion of the modulation can now be written as a discrete sum

$$W_p(x-vt) = \sum_{n=-\infty}^{+\infty} a^F(\frac{2\pi n}{P}) \exp(-j\frac{2\pi n}{P}vt) \exp(-j\frac{2\pi n}{P}x), \tag{5.7}$$

where $a^F(k_x)$ denotes the Fourier components of the plane-wave decomposition of $a(x)$. With the same procedure used in the previous section, the scattered optical field can now be decomposed in discrete spatial frequencies.

$$U_m(x,t) = A_i \sum_{n=-\infty}^{+\infty} a^F(n\frac{2\pi n}{P}) \exp(j2\pi(f_0 - \frac{n}{P}v)t) \exp(-j(k_{0x} + \frac{2\pi n}{P})x), \tag{5.8}$$

As a result of the discrete expansion in plane waves, the light is scattered into discrete angles in the far field. According to the mapping relation in Eq. 5.4, different directions have different temporal frequency shifts.

These equations can describe the acoustic-optic interactions in the Raman-Nath regimes (short acoustic-optic interaction length).

5.3.3 Finite modulation region

In practice, the width of the modulation region (in the x direction) cannot be infinitely long. In order to account for the finite size of the incoming beam, the finite size of the modulation region, or the amplitude and phase differences along the modulation direction, we introduce a factor $G(x)$ in the system. The simplest

case for $G(x)$ is a rectangle function which is zero everywhere except for the finite modulation region. The modulation function can be written as

$$M(x,t) = G(x)W(x - vt). \tag{5.9}$$

Since the angular frequency spectrum of the scattered field is proportional to the Fourier transform of $M(x)$, it can be described as the convolution between the plane-wave expansion of $G(x)$ and the Fourier expansion of $W(x - vt)$. In this case, the mapping relation between the wave vectors and temporal frequency shifts (Eq. 5.4) is not strictly valid anymore. However, if $G(x)$ describes a curve that is relatively wide such that in the angular frequency domain it has a small angular bandwidth, Eq. 5.4 can still be used as a large field approximation. In the case of periodic modulations, the discrete frequency components will mix unless the width of $G(x)$ is big enough to ensure the minimal beam size of the scattered light is smaller than the angular separation of the discrete beams. When $G(x)$ breaks the large field approximation, numerical methods can be used to analyze the scattered fields.

5.3.4 Discrete Modulator array and coupling to Free Propagation Region

While considerable advancements have been made in incorporating acousto-optic materials onto the silicon photonics platform [81], these additions necessitate extra processing steps beyond most commercially available silicon photonic platforms, leading to higher costs and increased complexity. In this context, we propose a discrete modulator array coupled to a Free Propagation Region (FPR) as an alternative for achieving wave-like modulation. Fig. 5.5(a) shows a possible on-chip layout of a discrete modulator array coupled to an FPR through a grating with spacing Λ. We aim to replicate the characteristics of diffracted light under acoustic modulation by coupling wave-like modulated light of this array to an FPR. First, the properties of a 1D linear phased array grating and its coupling to an FPR are discussed. Subsequently, the theory of wave-like modulation is combined with the grating array properties to design multibeam frequency shifters based on discrete modulator arrays.

A phased array grating serves to convert phase and intensity relations between discrete elements into a specific far-field pattern after propagating through an FPR. While various forms of optical arrayed gratings exist, we focus on a 1D linear array for simplicity. Consider a 1D linear array of N elements with field profile $m(x)$ (and $m^F(k_x)$ its spatial Fourier transform), spaced with a period of Λ along the x-axis, similar to the grating depicted in Fig. 5.5(a). Considering equal amplitude

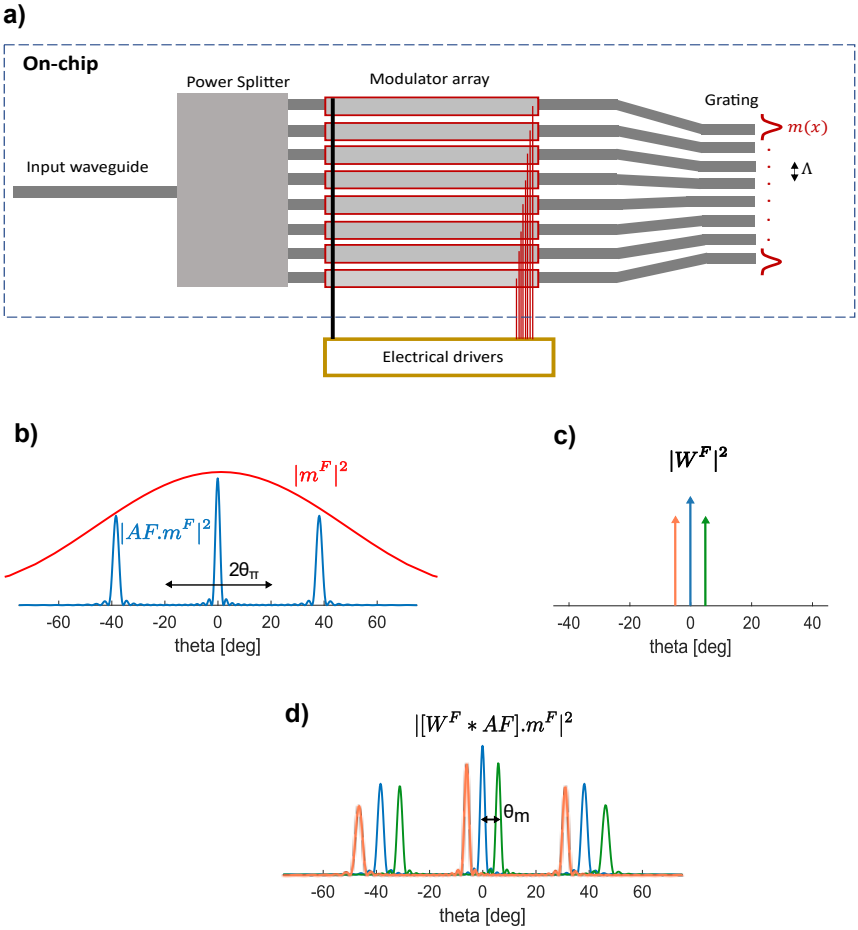

Figure 5.5: a) Schematic of a modulator array connected to a grating array with spacing Λ and element field profile $m(x)$. b) In red: the far field pattern m^F of a single element with a rectangular field profile $m(x)$ with $width = 800\ nm$. In blue; the angular intensity profile of the passive array grating of 16 elements with equal amplitude and phase. c) Output of a plane wave modulated in periodic traveling-wave-like fashion resulting in discrete output angles with each having a different frequency shift compared to the central beam. Here only the $\pm 1^{st}$ order sidebands were considered. d) Combining the traveling-wave-like modulation technique and the passive array grating output, an angular output spectrum which is the convolution of b) and c) is obtained.

elements, but a linear phase shift $\Delta\psi$ between consecutive elements, we can write for the field at the x-axis (with $'*'$ representing convolution) :

$$\begin{aligned} U_m(x,t) &= \sum_{n=0}^{N} \left[A_i \exp(j(2\pi f_0 t - n\Delta\psi))\delta(x - n\Lambda)\right] * m(x) \\ &= \left[A_i \exp(j(2\pi f_0 t - k_{0x}x)) \sum_{n=0}^{N} \delta(x - n\Lambda)\right] * m(x) \end{aligned}$$

$$\text{with} \quad k_{0x} = \Delta\psi/\Lambda \tag{5.10}$$

$$= A_i \exp(j2\pi f_0 t) \int_{-\infty}^{+\infty} AF(k_x, \Lambda) m^F(k_{0x} + k_x) \exp(-j(k_{0x} + k_x)x) dk_x \tag{5.11}$$

where AF is the array factor of a 1D linear array grating:
$AF(k_x, \Lambda) = \sum_{n=0}^{N} \exp(-jnk_x\Lambda)$.

The Fourier transform of the element field profile, multiplied by the grating array factor, results in the angular decomposition after a periodic, finite grating. Fig. 5.5(b) presents the angular intensity profile of a 16-element linear array grating (blue) derived from the modulus squared of the single-element Fourier transform (red) multiplied by the array factor. We used a wavelength $\lambda = 1550$ nm, pitch $\Lambda = 2.5$ μm , and approximated each element's field profile using an 800 nm width rectangular function. In Fig. 5.5(b) we assumed no linear phase shift to be present ($\Delta\psi = 0 \rightarrow k_{0x} = 0$) such that $2\pi k'_x = \sin(\theta)/\lambda$. The indicated $2\theta_\pi$-region in the figure represents the 0_{th} order diffraction region when scanning with the phased array grating with a consecutive phase delay $\Delta\psi$ between $-\pi$ and π. This region will be important when designing the grating structure.

N equal phase shifts $\Delta\psi$ between consecutive elements induce a shift of the array factor enabling light direction tuning via a linear phased array. The 0^{th} grating order's output angle can be estimated with $\sin(\theta) = \frac{\Delta\psi}{\Lambda}\frac{\lambda'}{2\pi}$, where λ' refers to the wavelength in the FPR and θ the angle between the z-axis and the propagation direction.

In Eq. 5.11, we assumed identical field amplitude and linear phase shift for each element and linear phase shift. Now, we include wave-like modulation factor $W(x - vt)$, which modulates each element according to the wave-like character.

$$U_m(x,t) = A_i \int_{-\infty}^{+\infty} e^{j2\pi(f_0 - k_x v)t} [W^F * AF](k_x) m^F(k_{0x}+k_x) e^{-j(k_{0x}+k_x)x} dk_x. \tag{5.12}$$

With Eq. 5.12, the expected far field of this array under periodic and traveling-wave-like modulation can be calculated numerically. Fig. 5.5(c), shows the angular field pattern of a monochromatic wave ($\lambda = 1550$ nm) along the z-axis, scattered by a periodic wave-like modulation with a fundamental frequency of 1 MHz and a velocity of 14.76 m/s along the x-axis (for simplicity we assume only scattering to ± 1 harmonic). In this example, the ± 1 harmonics are scattered to around $\theta_m =$ + 6° and -6° (see Eq. 5.4). Considering the 16-element linear array with period $\Lambda = 2.5$ μm and a wavelength of 1550 nm, this wave-like modulation can be emulated by connecting the linear array to a modulator array (as shown in Fig. 5.5(a) with a linear phase shift $\Delta\psi = \pi/3$ between the modulation of the modulators respectively.

Eq. 5.12 tells us how to combine the results from Fig. 5.5(b) and (c) to yield the resulting far-field pattern in Fig. 5.5(d), it can be seen that by using a modulator array connected to a discrete array coupled to an FPR and emulating wave-like modulation, different discrete frequency shifts can be generated and separated in the FPR, which allows designing multibeam frequency shifters. The $2\theta_\pi$-region, determined by the grating period, and θ_m determined by the modulation and delay between modulators in consecutive arms, are two important parameters to consider during the design stage for a multibeam frequency shifter.

5.4 Design of multibeam frequency shifter

In the previous section, we discussed the potential for using a combination of a modulator array and a phased array grating to generate multiple discrete frequency-shifted beams with different propagation directions. Instead of using a straight optical phased array (Fig. 5.5 (a)) that projects light into the far field, one can use a curved optical phased array to focus the light, where it can be collected through output waveguide apertures [82]. These curved optical phased arrays, or star couplers, allow for designing a multibeam frequency shifter on a compact chip. Fig. 5.6 shows a schematic where a single frequency input is distributed across a waveguide array, and, after modulation, light is coupled from input apertures into an FPR (e.g. a slab waveguide). There, the different harmonics are directed to output waveguides at the end of the FPR. By using the modulator array to mimic the properties of a Raman-Nath acousto-optic modulator, as described earlier, different single sideband frequency-shifted beams can be directed to the output of each waveguide. In the following sections, we will examine the key design considerations for creating a frequency-shifting structure using a modulator array and an FPR.

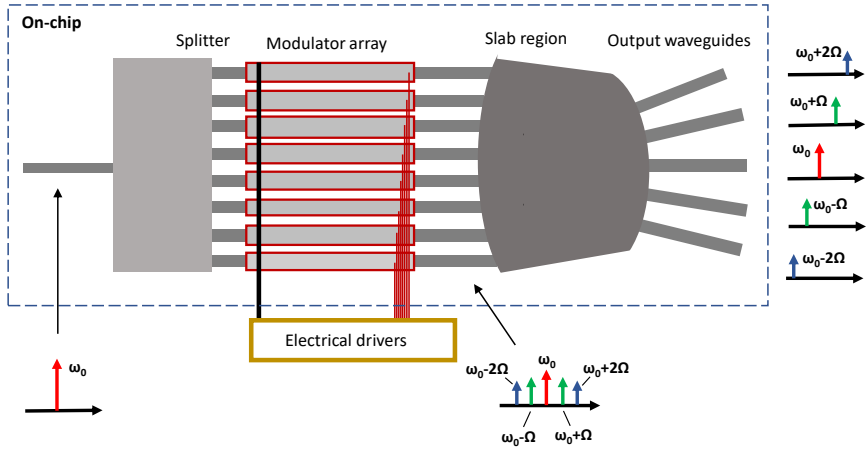

Figure 5.6: Schematic of an on-chip heterodyning component using a star coupler to separate the different beams generated through the traveling-wave-like modulation of the modulator array.

5.4.1 Optical Modulation

As described in Section 5.3, the optical modulation of the single-frequency input dictates the frequency content of the light relative to its original frequency. Periodic modulation disperses power across different carriers. This modulation can involve phase, amplitude, or a combination of both.

The characteristics and waveforms of the modulation are crucial considerations. The silicon photonics platform has seen the development of a broad range of modulation techniques and devices, including but not limited to Micro-Electro-Mechanical Systems (MEMS), thermo-optic modulators, free carrier dispersion modulators, and electro-absorption modulators [83, 84]. These devices enable amplitude and/or phase modulation with various characteristics and at different modulation frequencies.

Here, we discuss different modulation types that could be used for the multibeam frequency shifter such as: perfect phase modulation with different special modulation waveforms, a sine-driven pn-modulator, and amplitude modulation.

The left column in Fig. 5.7, shows these modulations in the time domain. The middle column shows how the harmonics behave when changing the modulation depth or voltage. The column on the right of Fig. 5.7, shows the spectrum for a specifically chosen modulation depth/voltage as indicated in the figures from the middle column. As can be seen from Fig. 5.7(a)-(c), pure sine phase modulation

gives rise to multiple sidebands, depending on the amplitude of the modulation. Fig. 5.7(c) shows the output spectrum for a pure sine phase modulation with modulation depth $r = 1.84$, which maximizes the amplitude of the -1^{st} and 1^{st} harmonic, as can be seen from 5.7(b). Fig. 5.7(d)-(f) shows results as expected from a 5-mm long pn-modulator ($L = 5$ mm), modeled using the description of the plasma dispersion effect from Soref and Bennett [85]. The output field E_m is expressed as:

$$E_m(t) = E_0(t)e^{-\frac{\Delta\alpha}{2}L} \cdot e^{i\frac{2\pi}{\lambda_0}\Delta nL}, \tag{5.13}$$

with $E_0(t)$ the output before any modulation, $\Delta\alpha$ the change in absorption coefficient and Δn , the change in refractive index at wavelength $\lambda_0 = 1.55$ μm. Now the refractive index change and absorption can be expressed according to Soref and Bennetts' relations with the hole and electron concentration changes ($\Delta N_h, \Delta N_e$):

$$\Delta n = -[8.8 \times 10^{-22}\Delta N_e + 8.5 \times 10^{-18}(\Delta N_h)^{0.8}], \tag{5.14}$$

$$\Delta\alpha = 8.5 \times 10^{-18}\Delta N_e + 6.0 \times 10^{-18}\Delta N_h. \tag{5.15}$$

In this simulation, modulation of the holes was considered and related to a voltage based on a measured $V_\pi L_\pi = 3\text{V} \cdot \text{cm}$. For a 5-mm pn-modulator then $V_\pi = 6$ V from which linear interpolation gives an estimate of $\Delta N_h/\Delta V = 7{\cdot}10^{15}$ cm^{-3}V^{-1}. The 5 mm pn-modulator has considerable insertion loss and we can see some small amplitude modulation apart from the larger phase modulation. Note that amplitude modulation is not detrimental to the working principle of the proposed design. To increase the number of sidebands in Fig. 5.7(f), one should apply higher voltages or increase the modulator length, but this increases the overall power loss.

In Fig. 5.7(m)-(o), we show results for pure amplitude modulation whereby the extinction ratio is linear with the applied voltage, (approximating the behavior of electro-absorption modulators). It is clear that amplitude modulation can also be used for sideband creation, but absorption-based modulators are fundamentally less power efficient compared to lossless phase modulators.

Other special modulations are possible and can yield interesting results. Fig. 5.7(g)-(i) and Fig. 5.7(j)-(l) show special cases for pure phase modulation. Sawtooth phase modulation with an amplitude covering a 2π phase modulation results in a single sideband output. This serrodyne technique creates one single frequency shifted beam but requires high bandwidth of the driving electronics and modulator [86, 87]. It has been proven that using dual or more sine phase modulations can equalize comb amplitudes (for a number of combs) [88, 89]. Fig. 5.7(j)-(l) show dual sine phase modulation giving rise to a comb profile with equalization of the 5 lowest order modes (-2,-1,0,1,2). Using different combinations of two or more sine phase modulations, one can equalize larger comb sizes.

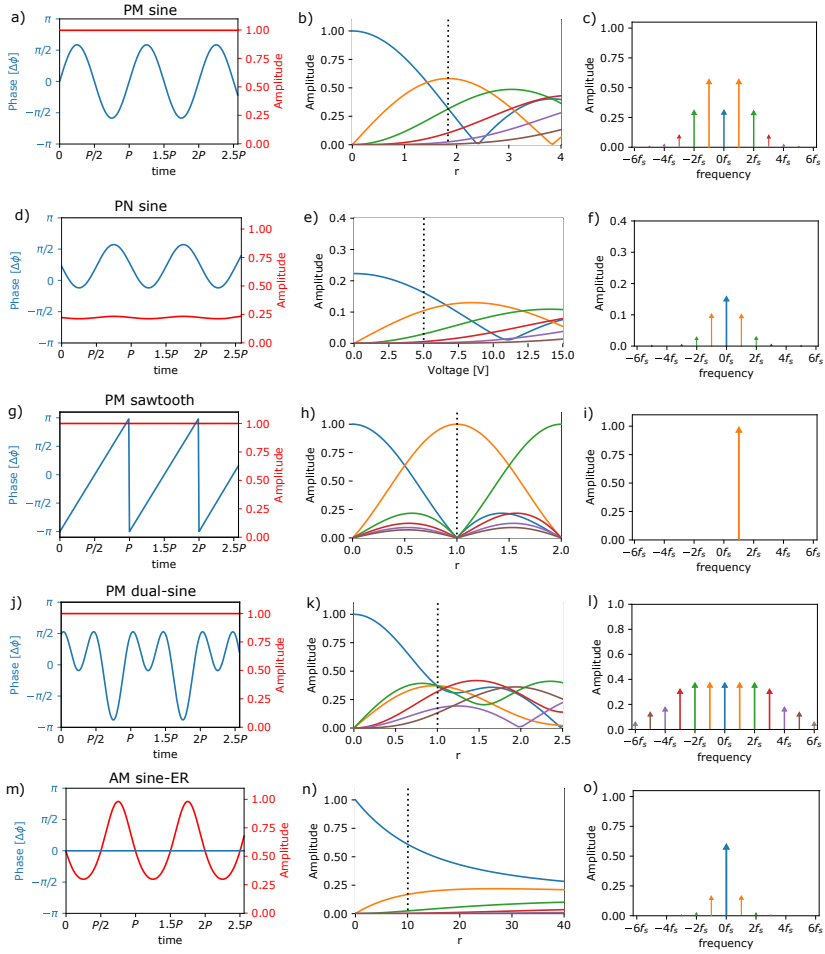

Figure 5.7: The figure in the first column shows the modulation waveform. The second column shows the influence of the change in the amplitude of that specific modulation and the third column shows the amplitude spectrum of the modulation depicted in the first column and highlighted with the dotted line in column 2. (a) to (c) considers pure sine phase modulation (PM-sine) whereby $\Delta\phi = r \cdot \sin(\omega_s t)$. (d) to (f) considers the 5 mm long pn-modulator driven by a voltage sine signal (PN-sine). (g) to (i) considers sawtooth phase modulation with amplitude of the phase modulation=$r \cdot \pi$. (PM-sawtooth) (j) to (l) shows a dual sine phase modulation with phase modulation described as $\Delta\phi = r \cdot [1.24 \sin \omega_s t + 1.53 \sin(\omega_s t + \pi/2)]$, resulting in an equalized output for the first five harmonics for r=1 (PM - dual sine). (m) to (o) depicts amplitude modulation driven by a sine signal (AM sine-ER) and where the extinction ratio is linear with the applied voltage yielding an amplitude modulation of $A = 10^{-r/20 \cdot (1+sin\omega_s t)}$

In the following section, we will consider using pure sinusoidal phase modulators with a modulation depth of 1.84 (as denoted with the dotted line in Fig. 5.7(b) for creating a 16-by-5 multibeam frequency shifter, collecting the harmonics between the -2^{nd} and $+2^{nd}$.

5.4.2 Star Coupler and phased array design

In the past decade, there has been increasing interest in optical phased arrays due to their potential for non-mechanical beam-steering in applications such as remote sensing and free-space communication [90]. Recent efforts have focused on optimizing steering range, minimizing side lobes to increase beam steering efficiency, and demonstrating 2D arrays [90, 91]. These optical phased arrays could be used to create a free-space coupled multibeam frequency shifter, provided each element can be modulated with wave-like modulation relative to each other, as described in Section 5.3. However, here, we focus on the development of a multibeam frequency shifter that does not couple into free space. Instead, we employ a star coupler to propagate and collect the frequency-shifted beams on-chip.

For a star coupler design, the input grating follows a circular arc, creating a circular phase front focusing on the center of the circle when no phase difference is present between the input waveguides. Introducing a phase difference between consecutive elements creates a shift of the focal point, which will move along a new circle with half the radius, called the Rowland circle. Now, by taking into account the number of output apertures, one can start determining the different parameters of the star coupler.

Consider, that one chooses to collect or use M output waveguides. For a star coupler design, it is important to position the output waveguides in agreement with the expected diffracted angle of the harmonics to be collected. It is however possible to tune the separation between the diffraction angles by changing the delay of modulation between consecutive modulators.

When considering modulation by applying a sine signal or any other symmetric signal, the distribution across the harmonics is symmetric. Without an angular shift applied, a symmetric output design where the harmonics between -(M-1)/2 and +(M-1)/2 are captured or used, can result in a power-efficient system. For such a system, we follow the general design guidelines for an N-by-M star coupler. The number of input apertures N is important for the efficiency of coupling to the output apertures, generally one uses at least $N > 3M$ input apertures for M output channels [82]. First, the spreading angle of the star coupler output aperture can be calculated by looking at the far-field projection. The N input apertures should be distributed within the spreading angle for efficient power coupling and results in a

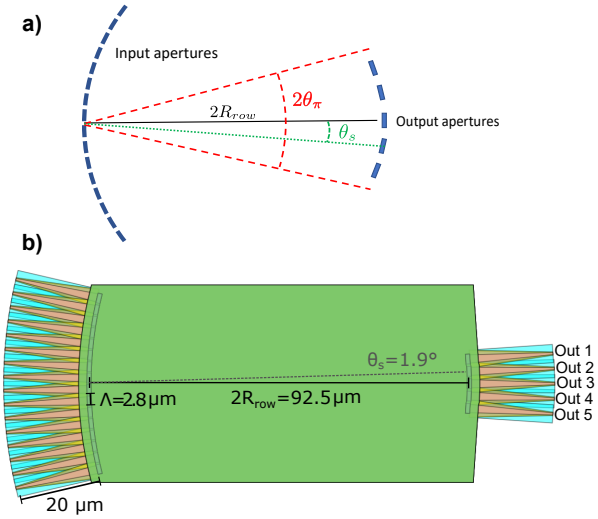

Figure 5.8: a) Schematic of the layout of the star coupler with important design parameters; the diameter of the Rowland circle, which is the distance between the in- and output apertures $2R_{row}$, the spreading angle θ_s and 0^{th} order diffraction angle $2\theta_\pi$. b) Design of the 16-by-5 starcoupler.

minimum for the radius of the Rowland circle.

The schematic in Fig. 5.8(a) shows the important parameters to consider for the star coupler design. From the period of the N input apertures, we can estimate the $2\theta_\pi$ region; it is the angle scanned by the 0^{th} order diffraction for the phased array with the phase delay $\Delta\psi$ scanned from $-\pi$ to π. The M output apertures should fit within $2\theta_\pi$ region while staying away from the edges of this region. Otherwise, the M^{th} harmonic might overlap with output waveguides.

With these considerations in mind, the minimal grating radii of the star coupler can be calculated. To arrange M output waveguides, an initial approach would be to choose the angular separation to be equal and approximately $\theta_s = 2\theta_\pi/(M+1)$. This choice ensures the collection of different harmonics while preventing the $\pm((M+1)/2)$ harmonics from overlapping with any output. However, higher harmonics might overlap with the outputs. If this overlapping becomes an issue, for instance, when using modulation with power in these higher harmonics, it can be mitigated by decreasing the angular separation. This will be further elaborated in Section 5.5.

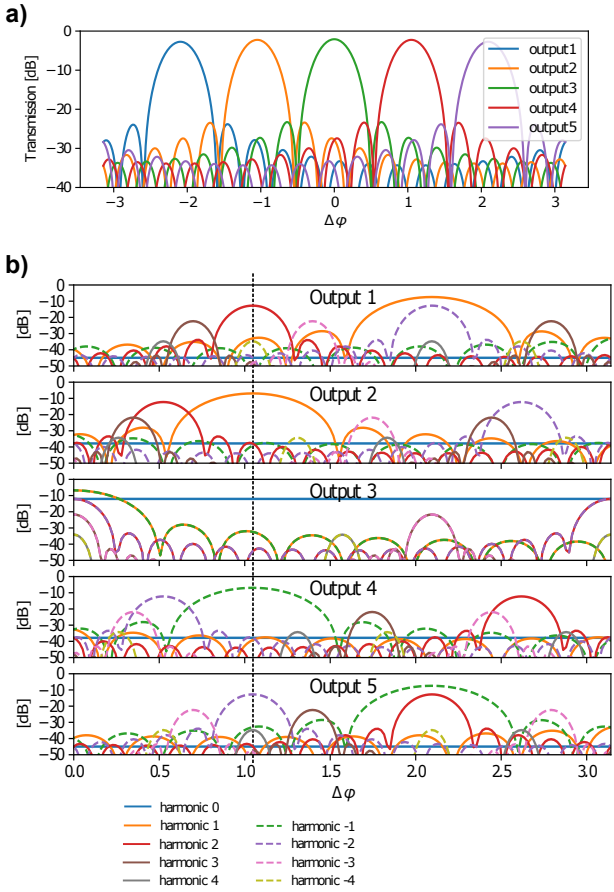

Figure 5.9: a) The transmission to different outputs of the 16-by-5 star coupler, with equally distributed input in the function of the phase difference between consecutive inputs. b) Resulting output power of the different harmonics into different ports when using pure sine phase modulation with depth 1.84 for different delays between the consecutive modulators. The dotted line at $\Delta\phi = \pi/3$ indicates the phase delay for which the different harmonics are aligned with the output directions.

5.5 Simulation

After determining different parameters, the design and performance can be estimated through simulation. Here, we first calculate the S-matrix of the star coupler using the IPKISS AWG designer [92]. Apertures are simulated using CAMFR [93], doing 1D mode solving and 2D eigenmode expansion propagation. The propagation through the FPR is calculated through the Rayleigh-Sommerfeld diffraction expressions. Modal overlaps are used for calculating power coupling into the waveguides. Here, a 220 nm thick silicon platform is considered, as is typical for commercially available silicon photonic platforms [17]. Following the guidelines described in this section, we designed a 16-by-5 star coupler with an input grating period of 2.8 μm. The design features a 20 μm linear taper structure from a single mode wire waveguide to the shallow-etched rib-wire apertures with a width of 2 μm and a Rowland circle radius equal to 46.25 μm (Fig. 5.8b. We set $\theta_s = 2\theta_\pi/6 = 1.9°$, as depicted in the design layout in Fig. 5.8b. Fig. 5.9a shows the transmission to the different ports, depending on the phase difference between the various arms. This is based on the scattering matrix while assuming equal power into every input arm and no modulation.

As illustrated in Fig. 5.8a, the outputs from the star coupler exhibit about -25 dB crosstalk to the neighboring outputs due to sidelobes. This crosstalk, along with the insertion loss from the star coupler, could be improved by increasing the aperture angle as viewed from the outputs [82], but this would necessitate the addition of more modulators to the star coupler.

Considering a perfect sine phase modulator with modulation depth $r = 1.84$ (as defined in Fig. 5.7), the amplitudes of the harmonics behave as depicted in Fig. 5.7a-c. Assuming this modulation results in Fig. 5.9b, where it can be seen that the majority of the power will be contained in the 1^{st} and -1^{st} harmonic, while there will still be a substantial amount of power in the other captured harmonics.

In Fig. 5.9a, the transmission of the star coupler is plotted, when the inputs have the same amplitude for different detunings of the phased array (without modulation). We can see optimal transmission in the different output ports at multiples of $\pi/3$. This is as expected since we chose

$$\theta_s = \frac{2\theta_\pi}{M+1} \xrightarrow{M=5} \frac{\theta_\pi}{3}. \tag{5.16}$$

Fig. 5.8b shows the calculated output power of different harmonics for the multi-beam frequency shifter for sine phase modulation, with a modulation depth of around 1.84 (as was shown in Fig. 5.7(a-c)). The x-axis denotes the delay between consecutive modulations. It can be seen that for a delay of around $\pi/3$, we collect

the 2^{nd} harmonic in the upper waveguide with over 20 dB suppression of other harmonics. In the second output waveguide, we collect the 1^{st} harmonic with around 30 dB suppression and the 0^{th} harmonic in the central output waveguide with 20 dB suppression of other sidebands. The lower two waveguides collect the -1^{st} and -2^{nd} harmonic. The 2D eigenmode expansion propagation results were confirmed through a 2D FDTD simulation of the star coupler, as illustrated in Fig. 5.10. In this simulation, a scattering matrix of the star coupler was created by doing 2D FDTD simulations, where each time a different output aperture is excited with the 2D TE fundamental mode and the TE fundamental modes at the in and output apertures are monitored. Now, using the reciprocity of Maxwell's equations for time-invariant linear reciprocal media, a scattering matrix from the in- to the output TE fundamental modes of the star coupler can be created. With the scattering matrix of the star coupler and knowing the modulated input in each arm, the output for each discrete harmonic can be calculated. The delay between the modulators was assumed to be the optimal value at 1550 nm (as indicated in Fig. 5.8b). The results, in Fig. 5.10b, indicate the performance of the frequency shifter over a broad wavelength range and similar results as the propagation simulation.

5.5.1 Output angle

As mentioned before, setting $\theta_s = 2\theta_\pi/(M+1)$ ensures the collection of the M lowest harmonics while preventing the $\pm((M+1)/2)$ harmonics from overlapping with any output. However, higher harmonics might overlap as well with the outputs. For a 16-by-5 star coupler with results from Fig. 5.9b this effect is barely noticeable but for $\phi = \pi/3$ the output that efficiently collects the 2^{nd} harmonic, will also collect the -4^{th}, while the direction of the output collecting the 1^{st} harmonic coincides with the direction of the -5^{th} harmonic,... In the example discussed previously (Fig. 5.9), this overlap does not significantly decrease the suppression rate because the modulation used doesn't contain substantial power in these overlapping harmonics as can be seen from Fig. 5.5.

However, if we aim to use different modulations that contain considerable power in these higher harmonics, it could reduce the suppression ratio. Considering dual sine phase modulation as discussed in Fig. 5.7(j-l), the resulting collected output can be plotted as seen in Fig. 5.11. In this figure, we only plotted outputs 1,2 and 3 since, a symmetric comb profile and a symmetric star coupler design, outputs 4 and 5 can be derived through symmetry from outputs 2 and 3 by reversing the sign of the harmonics as can also be seen in the example from 5.9 b. From Fig. 5.11, it is evident that when $\theta_s = 2\theta_\pi/(M+1) = 2\theta_\pi/6$, higher harmonics are indeed overlapping when the collected harmonics are directed to the outputs. However, by choosing a slightly adjusted angular separation $\theta_s = 2\theta_\pi/(M+3/2) = 2\theta_\pi/(6+1/2)$,

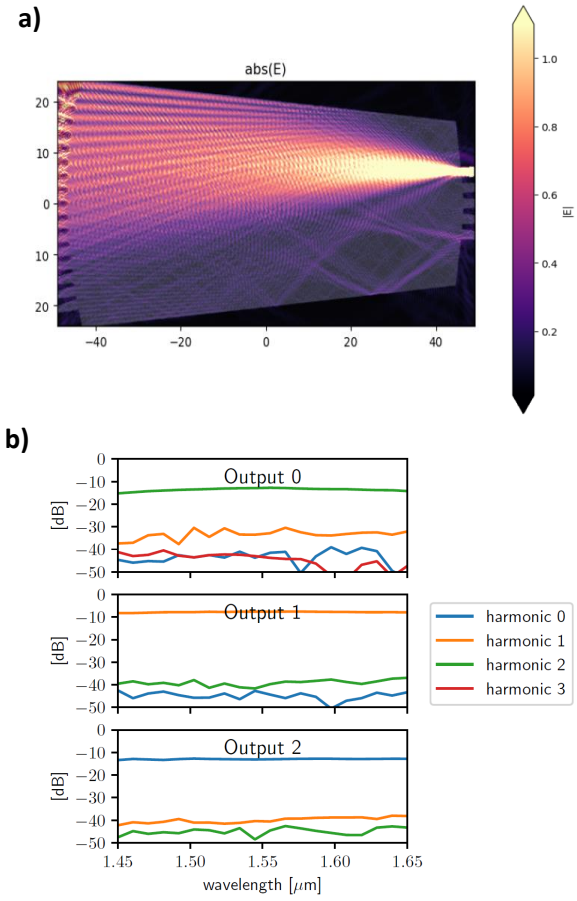

Figure 5.10: a)A 2D FDTD simulation of the excited TE mode in the top output waveguide is performed. By repeating this for all the output waveguides and monitoring the fundamental TE mode at the input, a scattering matrix can be constructed to characterize the relationships between the desired input and output ports. b) 2D FDTD results of output power of the different harmonics into different ports when using pure sine phase modulation with depth 1.84 for the geometry as described and with optimized phase delay of the modulation for 1550 nm

the higher harmonics are directed in between the various output angles. Fig. 5.11, therefore shows that this slight change of the output angle is a mitigation strategy for overlapping harmonics.

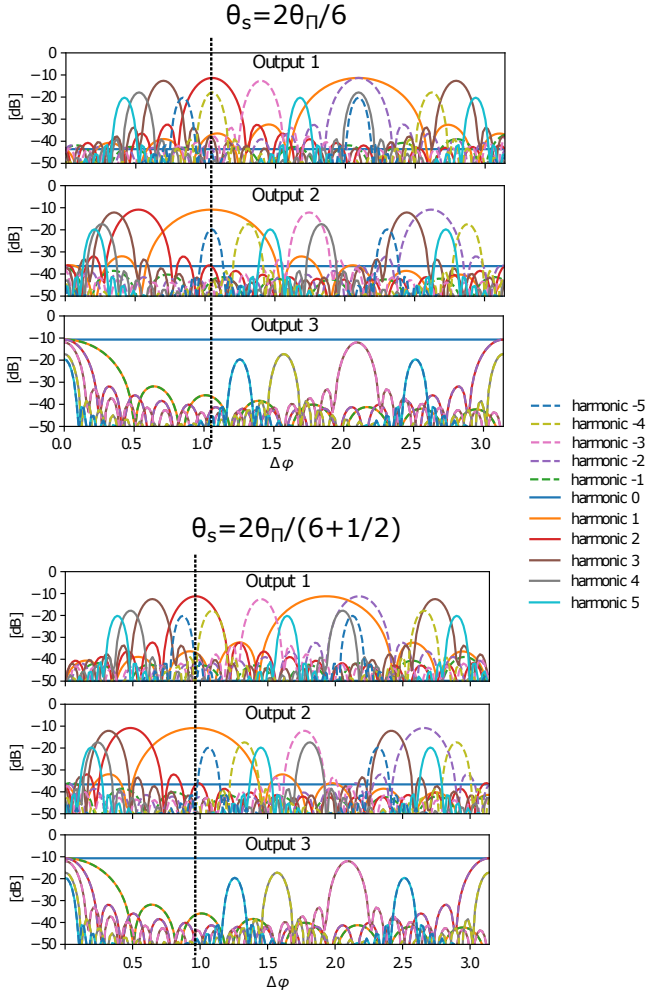

Figure 5.11: The harmonic power collected by various outputs from the 16-by-5 star coupler for different output angles, under the assumption of a dual-sine phase modulation input, shows distinct characteristics. When $\theta_s = 2\theta_\pi/6$, the higher harmonics overlap as they are directed toward the outputs. On the other hand, when $\theta_s = 2\theta_\pi/(6+1/2)$, the higher harmonics are steered in between the outputs. This observation illustrates that by choosing suitable output angles, it is possible to mitigate the overlap of higher harmonics with the outputs, thus improving the suppression ratio.

5.5.2 Discussion

Since, to the best of our knowledge, no similar devices that generate different frequency shifts in distinct arms have been proposed, we are limited to comparison against single-sideband frequency shifters. For this, different techniques have been reported, such as the serrodyne technique or IQ-based frequency shifters. The serrodyne technique uses sawtooth-shaped phase modulation to generate a single sideband output, but it suffers from modulator nonlinearities and limited bandwidth [86, 87]. IQ modulators, which use two Mach Zehnder modulators driven by cosine and sine signals with a $\pi/2$ phase difference, can also produce a single sideband output [94–96]. These IQ frequency shifters are less sensitive to modulator non-linearities and more suitable for generating high-frequency shifts. IQ-based frequency shifters remove sidebands through destructive interference from arms with multiple modulators [68, 97, 98]. Assuming lossless phase modulation in each arm, they have an upper-limit device loss of -4.7 dB for collecting the 1^{st} harmonic while having non-negligible higher harmonics. When optimally modulating for the first harmonic, the IQ-based frequency shifters exhibit a suppression ratio limited to approximately 15 dB due to the presence of -3^{rd} harmonics [94–96]. Improving the suppression ratio relative to this harmonic comes at a cost of power efficiency. Additionally, the insertion loss of individual modulators significantly impacts power efficiency. Recent demonstrations of IQ-based modulators show therefore largely varying suppression ratios of 10 to 25 dB and varying insertion losses [97, 98] (e.g., a lithium-niobate-based IQ frequency shifter shows an insertion loss of around -17.6 dB and a suppression ratio of 22 dB [97]).

To compare the theoretical performance of the designed frequency shifter with the IQ-based frequency shifter, we therefore assume both employ identical lossless modulations. For this theoretical comparison, we also neglect propagation losses (usually below 2 dB/cm for 220 nm thick SOI [99]) and losses due to splitters for both types of frequency shifter (0.05–0.2 dB per 1×2 - splitter [99]). Assuming the same modulation, we can see that the 16-by-5 multibeam frequency shifter requires 6 dB more RF power due to the multitude of modulators. When we look at the optical power budget, results from Fig. 5.8 show the collected power of the first harmonic of the 16-by-5 frequency shifter is -6.9 dB, which is less than the IQ-based frequency shifter (-4.7 dB). However, in the proposed design, we collect the light of other harmonics, resulting in a simulated optical loss of around -2.4 dB. This simulated value is primarily due to star coupler insertion losses, while the loss from uncollected higher harmonics is near zero because of the comb profile, which concentrates the power in the lower harmonics. In addition, we can see from Fig. 5.8(d) that for the 16-by-5 example of the multibeam frequency shifter, simulations indicate around 30 dB suppression for the 1^{st} harmonic and 20 dB for

the 0^{th} - and 2^{nd} harmonic. It's worth noting that the theoretical performance can be enhanced with more optimally designed star couplers. Previous demonstrations have shown that star couplers with superior suppression ratios and reduced insertion losses can be fabricated through optimization of mode matching and suppression of scattering in the star coupler [100].

5.6 Closing Remarks

This chapter introduces a new architecture for multibeam on-chip LDV. By incorporating a multibeam frequency shifter, various sensing beams can be multiplexed in the electronic domain. Although the new architecture appears promising and simulations suggest satisfactory performance of the multibeam frequency shifter, no experimental data has been presented due to time constraints for developing the advanced control and drive electronics. Operating the multibeam frequency shifter requires control of an array of modulators. These modulators must be addressable individually to ensure tunable delays, and the fundamental modulation frequency needs to exceed the frequency bandwidth of the vibrations to be detected. Consequently, the multibeam frequency shifter requires numerous driver channels operating at MHz speeds. Additionally, while the electrical signals are multiplexed and can be amplified simultaneously, the electronic circuit must eventually demultiplex and read out the signals. Despite these requirements, they appear manageable with sufficient resources. This leads us to believe that the architecture proposed in this chapter could be a viable solution for chip-based LDV systems with hundreds of sensing beams.

6

Conclusion and Outlook

Photoacoustic imaging has emerged as a significant research area over the past few decades, recently gaining traction with the introduction of commercial systems. This work focused on using silicon-photonics based LDVs in for enabling contactless, miniature photoacoustic imaging. Current photoacoustic imaging setups often require high-power lasers and contact-based ultrasound detectors, resulting in bulky and expensive configurations that necessitate physical contact with the sample through a coupling medium. A contactless, miniature photoacoustic system could revolutionize the field by expanding its applications and facilitating adoption in the medical sector. Consequently, the primary objective of this work is to advance photoacoustic imaging by developing systems that use silicon photonics-based LDVs for contactless detection. The specific goals of this study included:

- Develop and assess silicon photonics-based LDV as a tool for ultrasound detection.
- Demonstrate the feasibility of non-contact photoacoustic imaging using silicon photonics-based LDVs and a miniature excitation source.

- Explore challenges and solutions for the future of photoacoustic imaging systems using silicon-photonics based LDVs (eg. scaling the number of beams).

In the following sections, we present the key findings and conclude with a future outlook on the development of this technology.

6.1 Ultrasound Detection with Silicon Photonics-Based LDV

The homodyne silicon photonics LDV technology, as demonstrated in previous work [15], was adapted to measure ultrasound frequencies. The detection limit was measured and found to be close to the shot noise limit at ultrasound frequencies. However, as the frequency increases, the detection limit becomes worse due to the reduced amplitude of surface vibrations. The system was optimized for the lower ultrasound range, targeting a bandwidth of around 4 MHz.

The silicon-photonics-based LDV exhibited lower noise levels compared to commercial LDVs for measurements on a flat phantom, maintaining a useful bandwidth of up to 3.5 MHz. While noise levels for LDVs are still 2-4 orders of magnitude higher than state-of-the-art contact-based ultrasound detectors, air-coupled detection with conventional detectors is not an option due to the air-tissue impedance mismatch and the high propagation losses of ultrasounds in air. This makes LDV one of the preffered options for non-contact LDV

In an attempt to improve the detection limit of silicon photonics-based LDVs, the influence of the incorporation of a semiconductor optical amplifier in the LDV circuit was studied. Theoretical estimates showed however that the incorporation of an SOA generally did not significantly enhance the fundamental detection limit, except when the output beam is not yet near the safety-limit and the amplifier is used to boost the power of the output beam.

Overall, the on-chip LDV demonstrated high performance and presented a viable solution for non-contact ultrasound detection.

6.2 Photoacoustic Imaging with Silicon Photonics-Based LDV

A first-of-its-kind lab-based system was developed that demonstrates non-contact photoacoustic imaging with a silicon photonics-based LDV and a miniature excitation source. By scanning the silicon photonics-based LDV along a line over the surface of a photoacousticly excited phantom, a 2D image could be reconstructed. This setup has shown basic contactless imaging capabilities on a lab-based phantom with silicon photonics-based LDVs. However, the adaptation of this technology for in-vivo imaging presents several challenges, primarily due to the non-flat and highly diffusive surface of biological tissues.

One potential solution to these challenges is the use of high numerical aperture (NA) optics, which could efficiently collect light reflected from a diffuse surface. However, high NA systems have a limited depth of field and therefore could require automatic focusing techniques to maintain optimal focus on the target tissues.

6.3 Scaling the Number of Beams

Reducing the need for mechanical scanning is critical for decreasing imaging time. While the silicon photonics platform currently enables scaling up to a few tens of beams, achieving a scale of hundreds of beams necessitates new techniques or architectural innovations. In this work we present a new architecture, featuring a multibeam frequency shifter, which allows the multiplexing of LDV beams in the electrical domain. This method significantly reduces the number of required electrical connections, simplifying the system design.

Although simulations and preliminary designs indicate that this architecture has potential, experimental verification is still required. Future work should concentrate on overcoming the challenges associated with driving a large array of modulators and efficiently demultiplexing the resulting signals. Addressing these challenges will be crucial for enabling the practical implementation of large-scale, multibeam LDV systems, which could further revolutionize the field by significantly increasing imaging speed and resolution.

6.4 Outlook

In the short term, demonstrating in-vivo capabilities is essential. This includes developing an in-vivo demonstrator with high NA optics and automatic focusing techniques, preferably in a multibeam implementation. As highlighted in Chapter 4, illumination plays a critical role in determining the field of view and signal strength. Therefore, optimizing the illumination pattern is crucial and may involve the use of multiple laserbars or diodes. Given that most applications require same-side excitation and detection, advanced optical systems will be necessary to enhance both illumination and detection efficiency.

For practical applications, it is also crucial to reduce imaging time and minimize the need for scanning. Scaling up the number of beams is a key strategy to achieve this. Two approaches can be considered:

- Advanced Packaging Methods: With 2.5D or 3D integration techniques, the photonic integrated circuit (PIC) can be surface-mounted on an interposer or electrical IC, thereby allowing more connections and, consequently, more beams. This approach could support a few tens of LDV beams. However, for scaling to higher beam counts, another approach might be necessary.
- Novel Architecture: As discussed in Chapter 5, a newly proposed architecture might be necessary for scaling beyond tens of beams. However, The proposed architecture drastically differs from the conventional multibeam architecture, and efforts are required to verify performance experimentally.

While this work has identified several potential applications where contactless photoacoustic imaging could be highly valuable, further research is needed to demonstrate diagnostic capabilities. It is crucial to pinpoint impactful biomedical applications where the benefits of contactless imaging outweigh the drawbacks of potentially lower resolution compared to contact-based systems. Ultimately, finding commercially viable pathways is essential to enable the widespread adoption of these techniques.

This research establishes a foundation for future advancements in photoacoustic imaging, encouraging further exploration and development of silicon photonics-based LDVs as a transformative tool in medical diagnostics and beyond.

A

Appendix: Plane Wave Equations

Consider a plane wave incident perpendicular to a boundary between two media with acoustic impedances Z_1 and Z_2, respectively. Let the amplitudes of the incident, reflected, and transmitted waves be denoted by A_i, A_r, and A_t, respectively. The pressure fields for these waves are given by:

$$p_i(x,t) = A_i e^{j(\omega t - k_1 x)}, \tag{A.1}$$
$$p_r(x,t) = A_r e^{j(\omega t + k_1 x)}, \tag{A.2}$$
$$p_t(x,t) = A_t e^{j(\omega t - k_2 x)}, \tag{A.3}$$

where ω is the angular frequency, and $k_1 = \frac{\omega}{c_1}$ and $k_2 = \frac{\omega}{c_2}$ are the wave numbers in the two media.

At the boundary (taken as $x = 0$), the following boundary conditions must be satisfied:

1. **Continuity of pressure:** The pressure must be continuous across the boundary:
$$p_i(0,t) + p_r(0,t) = p_t(0,t). \tag{A.4}$$

2. **Continuity of particle velocity:** The normal component of the particle

velocity $v = \frac{p}{Z}$ must be continuous:

$$\frac{p_i(0,t) - p_r(0,t)}{Z_1} = \frac{p_t(0,t)}{Z_2}. \tag{A.5}$$

Substituting the expressions for the pressures into the boundary conditions, we get:

$$A_i + A_r = A_t, \tag{A.6}$$

$$\frac{A_i - A_r}{Z_1} = \frac{A_t}{Z_2}. \tag{A.7}$$

Solving these equations for the reflection coefficient $R = \frac{A_r}{A_i}$ and the transmission coefficient $T = \frac{A_t}{A_i}$, we find:

$$R = \frac{Z_2 - Z_1}{Z_2 + Z_1}, \tag{A.8}$$

$$T = \frac{2Z_2}{Z_2 + Z_1}. \tag{A.9}$$

These coefficients describe how the amplitude of the plane wave is divided between the reflected and transmitted waves when encountering the boundary between two media with differing acoustic impedances.

When the acoustic impedance of the first medium (Z_1) is much greater than that of the second medium (Z_2), such as when sound travels from water to air, the reflection coefficient R and transmission coefficient T simplify significantly.

The reflection and transmission coefficients are given by:

$$R = \frac{Z_2 - Z_1}{Z_2 + Z_1}, \tag{A.10}$$

$$T = \frac{2Z_2}{Z_2 + Z_1}. \tag{A.11}$$

The particle velocity at the boundary v_{boundary} is related to the transmitted pressure p_t by:

$$v_{\text{boundary}} = \frac{p_t}{Z_2}. \tag{A.12}$$

Using the transmission coefficient $T = \frac{A_t}{A_i} = \frac{2Z_2}{Z_2+Z_1}$, the transmitted pressure can be expressed in terms of the incident pressure $p_t = T \cdot p_i$ Substituting this into the expression for velocity and using the transmission coefficient we get:

$$v_{\text{boundary}} = \frac{T \cdot p_i}{Z_2} = \frac{2Z_2}{(Z_2 + Z_1)Z_2} p_i = \frac{2p_i}{Z_2 + Z_1}. \tag{A.13}$$

When $Z_1 \gg Z_2$, which is the case when working with a water—air- or tissue—air-interface, the relation between the amplitude of the pressure and the boundary velocity can be approximated as:

$$p_i \approx \frac{Z_1}{2} v_{\text{boundary}}. \tag{A.14}$$

References

[1] Paul Beard. *Biomedical photoacoustic imaging*. Interface Focus, 1:602–631, 2011.

[2] Lihong V. Wang and Junjie Yao. *A practical guide to photoacoustic tomography in the life sciences*. Nature Methods, 13:627–638, 2016.

[3] Mucong Li, Yuqi Tang, and Junjie Yao. *Photoacoustic tomography of blood oxygenation: A mini review*. Photoacoustics, 10:65–73, 6 2018.

[4] Daiwei Li, Lucas Humayun, Emelina Vienneau, Tri Vu, and Junjie Yao. *Seeing through the Skin: Photoacoustic Tomography of Skin Vasculature and Beyond*. JID Innovations, 1:100039, 9 2021.

[5] Eun Yeong Park, Haeni Lee, Seongyi Han, Chulhong Kim, and Jeesu Kim. *Photoacoustic imaging systems based on clinical ultrasound platform*. Experimental Biology and Medicine, 247:551–560, 4 2022.

[6] Thomas Sartoretti, Elisabeth Sartoretti, Candid Bucher, Aleksis Doert, Christoph Binkert, Klaus Hergan, Matthias Meissnitzer, Johannes Froehlich, Orpheus Kolokythas, Simon Matoori, Christina Orasch, Sebastian Kos, Sabine Sartoretti-Schefer, and Andreas Gutzeit. *Bacterial contamination of ultrasound probes in different radiological institutions before and after specific hygiene training: do we have a general hygienical problem?* European Radiology, 27:4181–4187, 2017.

[7] Jens Horstmann, Hendrik Spahr, Christian Buj, Michael Münter, and Ralf Brinkmann. *Full-field speckle interferometry for non-contact photoacoustic tomography*. Physics in Medicine and Biology, 60:4045–4058, 5 2015.

[8] Armin Hochreiner, Johannes Bauer-Marschallinger, Peter Burgholzer, Bernhard Jakoby, and Thomas Berer. *Non-contact photoacoustic imaging using a fiber based interferometer with optical amplification*. Biomedical Optics Express, 4:2322, 11 2013.

[9] Parsin Hajireza, Wei Shi, Kevan Bell, Robert J. Paproski, and Roger J. Zemp. *Non-interferometric photoacoustic remote sensing microscopy*. Light: Science and Applications, 6, 6 2017.

[10] Huanhao Li, Fei Cao, Yingying zhou, Zhipeng yu, and Puxiang Lai. *Interferometry-free noncontact photoacoustic detection method based on speckle correlation change*. Optics Letters, 44:5481, 11 2019.

[11] Jonghyun Eom, Seong Jun Park, and Byeong Ha Lee. *Noncontact photoacoustic tomography of in vivo chicken chorioallantoic membrane based on all-fiber heterodyne interferometry*. Journal of Biomedical Optics, 20:106007, 10 2015.

[12] Yi Wang, Yingxin Hu, Binyang Peng, Hongxian Zhou, Yuqian Zhao, and Zhenhe Ma. *Complete-noncontact photoacoustic microscopy by detection of initial pressures using a 3×3 coupler-based fiber-optic interferometer*. Biomedical Optics Express, 11:505, 1 2020.

[13] Elisabeth Leiss-Holzinger, Johannes Bauer-Marschallinger, Armin Hochreiner, Philipp Hollinger, and Thomas Berer. *Dual modality noncontact photoacoustic and spectral domain OCT imaging*. Ultrasonic Imaging, 38:19–31, 1 2016.

[14] Yanlu Li, Louise Marais, Hakim Khettab, Zhiheng Quan, Soren Aasmul, Rob Leinders, Ralf Schüler, Padraic E. Morrissey, Stephen Greenwald, Patrick Segers, Michael Vanslembrouck, Rosa M. Bruno, Pierre Boutouyrie, Peter O'Brien, Mirko de Melis, and Roel Baets. *Silicon photonics-based laser Doppler vibrometer array for carotid-femoral pulse wave velocity (PWV) measurement*. Biomedical Optics Express, 11:3913, 7 2020.

[15] Yanlu Li, Jinghao Zhu, Matthieu Duperron, Peter O'Brien, Ralf Schüler, Soren Aasmul, Mirko de Melis, Mathias Kersemans, and Roel Baets. *Six-beam homodyne laser Doppler vibrometry based on silicon photonics technology*. Optics Express, 26:3638–3645, 6 2018.

[16] Bahram Jalali and Sasan Fathpour. *Silicon photonics*. Journal of Lightwave Technology, 24:4600–4615, 2006.

[17] Abdul Rahim, Jeroen Goyvaerts, Bertrand Szelag, Jean Marc Fedeli, Philippe Absil, Timo Aalto, Mikko Harjanne, Callum Littlejohns, Graham Reed, Georg Winzer, Stefan Lischke, Lars Zimmermann, Dieter Knoll, Douwe Geuzebroek, Arne Leinse, Michael Geiselmann, Michael Zervas, Hilde Jans, Andim Stassen, Carlos Dominguez, Pascual Munoz, David Domenech, Anna Lena Giesecke, Max C Lemme, and Roel Baets. *Open-access silicon*

photonics platforms in Europe. IEEE Journal of Selected Topics in Quantum Electronics, 25:1–18, 6 2019.

[18] Xiaosheng Zhang, Kyungmok Kwon, Johannes Henriksson, Jianheng Luo, and Ming C. Wu. *A large-scale microelectromechanical-systems-based silicon photonics LiDAR*. Nature, 603:253–258, 3 2022.

[19] Christopher V Poulton, Ami Yaacobi, David B Cole, Matthew J Byrd, Manan Raval, Diedrik Vermeulen, and Michael R Watts. *Coherent solid-state LIDAR with silicon photonic optical phased arrays*. Opt. Lett., 42:4091–4094, 10 2017.

[20] Bhavin J. Shastri, Alexander N. Tait, T. Ferreira de Lima, Wolfram H.P. Pernice, Harish Bhaskaran, C. D. Wright, and Paul R. Prucnal. *Photonics for artificial intelligence and neuromorphic computing*. Nature Photonics, 15:102–114, 2 2021.

[21] Muzammil Iqbal, Martin A Gleeson, Bradley Spaugh, Frank Tybor, William G Gunn, Michael Hochberg, Tom Baehr-Jones, Ryan C Bailey, and L Cary Gunn. *Label-Free Biosensor Arrays Based on Silicon Ring Resonators and High-Speed Optical Scanning Instrumentation*. IEEE Journal of Selected Topics in Quantum Electronics, 16:654–661, 2010.

[22] Sudip Shekhar, Wim Bogaerts, Lukas Chrostowski, John E Bowers, Michael Hochberg, Richard Soref, and Bhavin J Shastri. *Roadmapping the next generation of silicon photonics*. Nature Communications, 15:751, 2024.

[23] Qi Pian, Chao Wang, Xueli Chen, Jimin Liang, Lingling Zhao, Ge Wang, and Xavier Intes. *Multimodal Biomedical Optical Imaging Review: Towards Comprehensive Investigation of Biological Tissues*. Current Molecular Imaging, 3:72–87, 11 2014.

[24] Mehreen Adhi and Jay S. Duker. *Optical coherence tomography-current and future applications*. Current Opinion in Ophthalmology, 24:213–221, 5 2013.

[25] B Wan, C Ganier, X Du-Harpur, N Harun, F M Watt, R Patalay, and M D Lynch. *Applications and future directions for optical coherence tomography in dermatology*. British Journal of Dermatology, 184:1014–1022, 2021.

[26] Srirang Manohar and Daniel Razansky. *Photoacoustics: a historical review*. Advances in Optics and Photonics, 8:586, 12 2016.

[27] Alexander Graham Bell. *On the production and reproduction of sound by light*. American Journal of Science, 20:305–324, 10 1880.

[28] Mark Vengerov. *An Optical-Acoustic Method of Gas Analysis*. Nature, 158:28–29, 1946.

[29] M Delany. *The optic-acoustic effect in gases*. Science Progress, 47:459–467, 1959.

[30] Tyndall John. *Action of an intermittent beam of radiant heat upon gaseous matter*. Proceedings of the Royal Society of London, 31:307–317, 1881.

[31] J E Michaels. *Thermal impact—the mechanical response of solids to extreme electromagnetic radiation*. Planetary and Space Science, 7:427–433, 1961.

[32] R M White. *An Elastic Wave Method for the Measurement of Pulse-Power Density*. IRE Transactions on Instrumentation, I-11:294–298, 1962.

[33] Richard M White. *Generation of Elastic Waves by Transient Surface Heating*. Journal of Applied Physics, 34:3559–3567, 1963.

[34] Judith Weber, Paul C. Beard, and Sarah E. Bohndiek. *Contrast agents for molecular photoacoustic imaging*. Nature Methods, 13:639–650, 7 2016.

[35] Christopher P. Favazza, Lihong V. Wang, Omar W. Jassim, and Lynn A. Cornelius. *In vivo photoacoustic microscopy of human cutaneous microvasculature and a nevus*. Journal of Biomedical Optics, 16:1, 1 2011.

[36] Wenzhong Liu, Kathryn M Schultz, Kevin Zhang, Amy Sasman, Fengli Gao, Tsutomu Kume, and Hao F Zhang. *In vivo corneal neovascularization imaging by optical-resolution photoacoustic microscopy*. Photoacoustics, 2:81–86, 2014.

[37] Taiichiro Ida, Hideaki Iwazaki, Yasushi Kawaguchi, Satoko Kawauchi, Tsuyako Ohkura, Keiichi Iwaya, Hitoshi Tsuda, Daizoh Saitoh, Shunichi Sato, and Toshiaki Iwai. *Burn depth assessments by photoacoustic imaging and laser Doppler imaging*. Wound Repair and Regeneration, 24:349–355, 2016.

[38] Lihong Wang and Brian Thompson. *Photoacoustic Imaging and Spectroscopy*. CRC Press, 1st edition, 2009.

[39] Yuan Xu and Lihong V. Wang. *Time Reversal and Its Application to Tomography with Diffracting Sources*. Physical Review Letters, 92:4, 2004.

[40] Minghua Xu and Lihong V. Wang. *Analytic explanation of spatial resolution related to bandwidth and detector aperture size in thermoacoustic or photoacoustic reconstruction*. Physical Review E - Statistical Physics, Plasmas, Fluids, and Related Interdisciplinary Topics, 67:15, 2003.

[41] Junjie Yao and Lihong V. Wang. *Photoacoustic microscopy*. Laser and Photonics Reviews, 7:758–778, 9 2013.

[42] Zohreh Hosseinaee, Nicholas Pellegrino, Nima Abbasi, Tara Amiri, James A.Tummon Simmons, Paul Fieguth, and Parsin Haji Reza. *In-vivo functional and structural retinal imaging using multiwavelength photoacoustic remote sensing microscopy*. Scientific Reports, 12, 12 2022.

[43] Yanlu Li, Emiel Dieussaert, and Roel Baets. *Miniaturization of Laser Doppler Vibrometers—A Review*. Sensors, 22, 7 2022.

[44] David A. B. Miller. *Perfect optics with imperfect components*. Optica, 2:747, 8 2015.

[45] R Halir, G Roelkens, A Ortega-Moñux, and J G Wangüemert-Pérez. *High-performance 90° hybrid based on a silicon-on-insulator multimode interference coupler*. Optics Letters, 36:178–180, 2011.

[46] E C M Pennings, R van Roijen, M J N van Stralen, P J de Waard, R.G.M.P. Koumans, and B H Verbeck. *Reflection properties of multimode interference devices*. IEEE Photonics Technology Letters, 6:715–718, 6 1994.

[47] S. Y. Siew, B. Li, F. Gao, H. Y. Zheng, W. Zhang, P. Guo, S. W. Xie, A. Song, B. Dong, L. W. Luo, C. Li, X. Luo, and G. Q. Lo. *Review of Silicon Photonics Technology and Platform Development*. Journal of Lightwave Technology, 39:4374–4389, 7 2021.

[48] Catherine Cooksey, Benjamin Tsai, and David Allen. *Spectral reflectance variability of skin and attributing factors*. page 94611. SPIE, 6 2015.

[49] Gunther Roelkens, Jing Zhang, Laurens Bogaert, Maximilien Billet, Dongbo Wang, Biwei Pan, Clemens J. Kruckel, Emadreza Soltanian, Dennis Maes, Tom Vanackere, Tom Vandekerckhove, Stijn Cuyvers, Jasper De Witte, Isaac Luntadila Lufungula, Xin Guo, He Li, Senbiao Qin, Grigorij Muliuk, Sarah Uvin, Bahawal Haq, Camiel Op De Beeck, Jeroen Goyvaerts, Guy Lepage, Peter Verheyen, Joris Van Campenhout, Geert Morthier, Bart Kuyken, Dries Van Thourhout, and Roel Baets. *Micro-Transfer Printing for Heterogeneous Si Photonic Integrated Circuits*. IEEE Journal of Selected Topics in Quantum Electronics, 29, 5 2023.

[50] Jinjun Xia and Gang Yao. *Angular distribution of diffuse reflectance in biological tissue*. Applied Optics, 46:6552–6560, 2007.

[51] Jerald G. Graeme. *Photodiode amplifiers : op amp solutions*. McGraw Hill, 1996.

[52] A. and P. Yariv Yeh. *Photonics: Optical Electronics in Modern Communications*. Oxford University Press, 2007.

[53] Wouter J. Westerveld, Md Mahmud-Ul-Hasan, Rami Shnaiderman, Vasilis Ntziachristos, Xavier Rottenberg, Simone Severi, and Veronique Rochus. *Sensitive, small, broadband and scalable optomechanical ultrasound sensor in silicon photonics*. Nature Photonics, 15:341–345, 5 2021.

[54] H E Bass, L C Sutherland, A J Zuckerwar, D T Blackstock, and D M Hester. *Atmospheric absorption of sound: Further developments*. The Journal of the Acoustical Society of America, 97:680–683, 1 1995.

[55] Yanlu Li and Emiel Dieussaert. *A Compensation Method for Nonlinearity Errors in Optical Interferometry*. Sensors, 23:7942, 9 2023.

[56] Peter L M Heydemann. *Determination and correction of quadrature fringe measurement errors in interferometers*. Applied Optics, 20:3382–3384, 1981.

[57] P. Welch. *The use of fast Fourier transform for the estimation of power spectra: A method based on time averaging over short, modified periodograms*. IEEE Transactions on Audio and Electroacoustics, 15:70–73, 1967.

[58] Stephen Hughes. *Medical ultrasound imaging*. Physics Education, 36:468, 8 2001.

[59] Kazuro Kikuchi, Chung-En Zah, and Toen-Pei Lee. *Measurement and Analysis of Phase Noise Generated from Semiconductor Optical Amplifiers*. Journal of quantum electronics, 27:416–422, 1991.

[60] Alexander William Setiawan Putra, Minoru Yamada, Hiroyuki Tsuda, and Sumiaty Ambran. *Theoretical Analysis of Noise in Erbium Doped Fiber Amplifier*. IEEE Journal of Quantum Electronics, 53, 2017.

[61] Alexander William Setiawan Putra, Minoru Yamada, Sumiaty Ambran, and Takeo Maruyama. *Theoretical Comparison of Noise Characteristics in Semiconductor and Fiber Optical Amplifiers*. IEEE Photonics Technology Letters, 30:756–759, 2018.

[62] Yang Liu, Zheru Qiu, Xinru Ji, Anton Lukashchuk, Jijun He, Johann Riemensberger, Martin Hafermann, Rui Ning Wang, Junqiu Liu, Carsten Ronning, and Tobias J Kippenberg. *A photonic integrated circuit-based erbium-doped amplifier*. Science, 376:1309–1313, 2022.

[63] ANSI Z136.9-2013. *American National Standard for Safe Use of Lasers*. Laser Institute of America, 2014.

[64] Nienke Bosschaart, Gerda J. Edelman, Maurice C.G. Aalders, Ton G. Van Leeuwen, and Dirk J. Faber. *A literature review and novel theoretical approach on the optical properties of whole blood*. Lasers in Medical Science, 29:453–479, 2014.

[65] Lindokuhle Ntombela, Naven Chetty, and Bamise Adeleye. *Effective attenuation coefficient and penetration depth of 630 nm laser light in polyvinyl alcohol slime glue phantoms simulating the human brain tumour*. Proceedings of the Estonian Academy of Sciences, 71:221–226, 2022.

[66] Guosong Hong, Alexander L. Antaris, and Hongjie Dai. *Near-infrared fluorophores for biomedical imaging*. Nature Biomedical Engineering, 1, 1 2017.

[67] Da-Kang Yao, Chi Zhang, Konstantin Maslov, and Lihong V Wang. *Photoacoustic measurement of the Grüneisen parameter of tissue*. Journal of Biomedical Optics, 19:017007, 2014.

[68] Guangyao Xu, Zhengyang Ni, Xizhou Chen, Juan Tu, Xiasheng Guo, Henrik Bruus, and Dong Zhang. *Acoustic Characterization of Polydimethylsiloxane for Microscale Acoustofluidics*. Physical Review Applied, 13:054069, 5 2020.

[69] V. Genovés, L. Maini, C. Roman, C. Hierold, and N. Cesarovic. *Variation in the viscoelastic properties of polydimethylsiloxane (PDMS) with the temperature at ultrasonic frequencies*. Polymer Testing, 124:108067, 7 2023.

[70] Bradley E. Treeby and B. T. Cox. *k-Wave: MATLAB toolbox for the simulation and reconstruction of photoacoustic wave fields*. Journal of Biomedical Optics, 15:021314, 2010.

[71] Dominik Marti, Rikke N. Aasbjerg, Peter E. Andersen, and Anders K. Hansen. *MCmatlab: an open-source, user-friendly, MATLAB-integrated three-dimensional Monte Carlo light transport solver with heat diffusion and tissue damage*. Journal of Biomedical Optics, 23:1, 12 2018.

[72] L. Mignanelli and C. Rembe. *Feasibility study of the employment of laser Doppler Vibrometry for photoacoustic imaging*. volume 1149. Institute of Physics Publishing, 12 2018.

[73] Kornel P Kö and Paul C Beard. *Two-dimensional photoacoustic imaging by use of Fourier-transform image reconstruction and a detector with an anisotropic response*. Applied Optics, 42:1899–1908, 2003.

[74] Charlie E M Strauss. *Synthetic-array heterodyne detection: a single-element detector acts as an array*. Optics Letters, 19:1609–1611, 6 1994.

[75] Y Fu, M Guo, and P B Phua. *Spatially encoded multibeam laser Doppler vibrometry using a single photodetector*. Optics Letters, 35:1356–1358, 2010.

[76] Adrianus Kowel. *Acousto-Optics-A Review of Fundamentals*. Poceedings of the IEEE, 69:48–53, 1981.

[77] Adrianus Korpel and Ting-Chung Poon. *Explicit formalism for acousto-optic multiple plane-wave scattering*. Journal of Optical Society of America, 70:817–820, 6 1979.

[78] Lutong Cai, Ashraf Mahmoud, Msi Khan, Mohamed Mahmoud, Tamal Mukherjee, James Bain, and Gianluca Piazza. *Acousto-optical modulation of thin film lithium niobate waveguide devices*. Photonics Research, 7:1003, 6 2019.

[79] Lei Wan, Zhiqiang Yang, Wenfeng Zhou, Meixun Wen, Tianhua Feng, Siqing Zeng, Dong Liu, Huan Li, Jingshun Pan, Ning Zhu, Weiping Liu, and Zhaohui Li. *Highly efficient acousto-optic modulation using nonsuspended thin-film lithium niobate-chalcogenide hybrid waveguides*. Light: Science and Applications, 11:2047–7538, 6 2022.

[80] M M De Lima, M Beck, R Hey, and P V Santos. *Compact Mach-Zehnder acousto-optic modulator*. Applied Physics Letters, 89:121104, 2006.

[81] Eric A Kittlaus, William M Jones, Peter T Rakich, Nils T Otterstrom, Richard E Muller, and Mina Rais-Zadeh. *Electrically driven acousto-optics and broadband non-reciprocity in silicon photonics*. Nature Photonics, 15:43–52, 6 2021.

[82] Meint K Smit and Cor Van Dam. *PHASAR-Based WDM-Devices: Principles, Design and Applications*. IEEE Journal of selected topics in Quantum Electronics, 2:236–250, 1996.

[83] Abdul Rahim, Artur Hermans, Benjamin Wohlfeil, Despoina Petousi, Bart Kuyken, Dries Van Thourhout, and Roel Baets. *Taking silicon photonics modulators to a higher performance level: State-of-the-art and a review of new technologies*. Advanced Photonics, 3:24003, 6 2021.

[84] Georgios Sinatkas, Thomas Christopoulos, Odysseas Tsilipakos, and Emmanouil E Kriezis. *Electro-optic modulation in integrated photonics*. Journal of Applied Physics, 130:10901, 6 2021.

[85] Richard A Soref and Brian R Bennett. *Electrooptical Effects in Silicon*. IEEE Journal of Quantum Electronics, 23:123–129, 1987.

[86] Leonard M Johnson and Charles H Cox. *Serrodyne Optical Frequency Translation with High Sideband Suppression*. Journal of Lightwave Technology, 6:109–112, 1988.

[87] D M S Johnson, J M Hogan, S w. Chiow, and M A Kasevich. *Broadband Optical Serrodyne Frequency Shifting*. Optics Letters, 35:745–747, 6 2010.

[88] Qingjiang Chang, Junming Gao, and Yikai Su. *Generation of optical comb frequency signal with high spectral flatness using two cascaded optical modulators*. Asia Optical Fiber Communication and Optoelectronic Exposition and Conference, pages 1–3, 2008.

[89] S Ozharar, F Quinlan, I Ozdur, S Gee, and P J Delfyett. *Ultraflat optical comb generation by phase-only modulation of continuous-wave light*. IEEE Photonics Technology Letters, 20:36–38, 6 2008.

[90] Jingwen He, Tao Dong, and Yue Xu. *Review of photonic integrated optical phased arrays for space optical communication*. IEEE Access, 8:188284–188298, 2020.

[91] Weihan Xu, Linjie Zhou, Liangjun Lu, and Jianping Chen. *Aliasing-free optical phased array beam-steering with a plateau envelope*. Optics Express, 27:3354, 6 2019.

[92] Wim Bogaerts, Martin Fiers, Massimo Sivilotti, and Pieter Dumon. *The IPKISS photonic design framework*. Optical Fiber Communication Conference, page W1E.1, 2016.

[93] Peter Bienstman and Roel Baets. *Optical modelling of photonic crystals and VCSELs using eigenmode expansion and perfectly matched layers*. Optical and Quantum Electronics, 33:327–341, 6 2001.

[94] S Shimotsu, S Oikawa, T Saitou, N Mitsugi, K Kubodera, T Kawanishi, and M Izutsu. *Single Side-Band Modulation Performance of a LiNbO3 Integrated Modulator Consisting of Four-Phase Modulator Waveguides*. IEEE Photonics Technology Letters, 13:364–366, 2001.

[95] Adrian A Dorrington and Rainer Kuennemeyer. *Single sideband techniques for laser Doppler velocimeter frequency offset*. Optical Engineering, 42:3239–3256, 6 2003.

[96] Tadasi Sueta and Shinsuke Shikama. *Integrated Optical SSB Modulator/Frequency Shifter*. IEEE Journal of Quantum Electronics, 17:2225–2227, 1981.

[97] Hsin-Pin Lo and Hiroki Takesue. *Precise tuning of single-photon frequency using an optical single sideband modulator*. Optica, 4:919, 6 2017.

[98] Panpan Shi, Liangjun Lu, Chuxin Liu, Gangqiang Zhou, Weihan Xu, Jianping Chen, and Linjie Zhou. *Optical FMCW Signal Generation Using a Silicon Dual-Parallel Mach-Zehnder Modulator*. IEEE Photonics Technology Letters, 33:301–304, 6 2021.

[99] Wim Bogaerts, Daniel Pérez, José Capmany, David A B Miller, Joyce Poon, Dirk Englund, Francesco Morichetti, and Andrea Melloni. *Programmable photonic circuits*. Nature, 586:207–216, 6 2020.

[100] Jaegyu Park, Gyungock Kim, Hyundai Park, Jiho Joo, Sanggi Kim, and Myung-Joon Kwack. *Performance improvement in silicon arrayed waveguide grating by suppression of scattering near the boundary of a star coupler*. Applied Optics, 54:5597, 6 2015.